THE PHASE BEHAVIOR OF A MODEL PLASMA MEMBRANE

A Dissertation

Presented to the Faculty of the Graduate School

of Cornell University

In Partial Fulfillment of the Requirements for the Degree of

Doctor of Philosophy

by

Andrew K Smith

May 2010

THE PHASE BEHAVIOR OF A MODEL PLASMA MEMBRANE

Andrew K Smith, Ph. D.

Cornell University 2010

The governing paradigm in biology states that understanding the structure of biological macromolecules and macromolecular assemblies will lead to an understanding of their cellular functions. While much progress has been made in understanding proteins/nucleic acids and their assemblies, the progress in understanding lipids/proteins and their assemblies, or biological membranes, has lagged behind. The main reason lies with the different interactions between the molecules. Proteins/nucleic acids tend to interact with high specificity at certain binding sites, but the interactions between lipids and proteins, especially between lipids themselves, tend not to be specific but show a high level of cooperativity among many molecules. Regarding just the lipids, this cooperativity manifests itself as phase behavior, both chemically, as coexisting phases, and mechanically, as phase domain morphology and dynamics. The chemical and mechanical phase behavior of lipid/protein mixtures directly relates to the physical structure of biological membranes; however, these membranes are much too complex to study directly. Therefore, membranes of simple but controllable compositions are required to model biological membranes. In this study, we explored the chemical and mechanical phase behavior of a ternary lipid mixture meant to model the plasma (outer) membrane of a mammalian cell. We used confocal fluorescence microscopy (CFM) and electron spin resonance (ESR) to construct a compositional phase diagram at 23°C that represents the chemical equilibrium of the model membrane. This phase diagram contains three two-phase coexistence regions (L_d + L_o, L_d + gel, and L_o + gel) and a three-phase

coexistence region ($L_d + L_o$ + gel). In addition, using ESR exclusively, we developed and applied a method to determine the infinite number of tie-lines, called the tie-line field, that partition the $L_d + L_o$ coexistence region into the compositions of the coexisting phases. Finally, CFM was used exclusively to explore the phase morphology and dynamics of this model membrane. We observed fluid phase percolation, long-range order/patterns among fluid phase domains, unusual shapes of solid phase domains, phase domain transitions within fluid-fluid phase coexistence, and light-induced phase separation. Elucidating the phase behavior of this model membrane is a step towards understanding the structure of biological membranes.

BIOGRAPHICAL SKETCH

Andrew has always been curious about the world around him; he would more enjoy examining a shiny rock or a slimy creature than play with normal childhood toys. Naturally critical and introspective, Andrew spent a huge amount of time in his head, constantly questioning what he thought and believed. His incessant thinking was rewarded when Andrew was nominated "Most Intellectual" of his class at Lassiter High School. His insatiable desire to learn carried on while he attended the Georgia Institute of Technology. Because of his fascination with Life and Death, Andrew focused on biology, but with the accumulation of additional knowledge from extracurricular math and physics classes, he was drawn to understand the fundamental nature of Nature. Therefore, Andrew went on to graduate school to obtain his PhD in at first molecular biology and then in biophysics. He not only wanted the degree as an achievement for a lifelong ambition to reach the zenith of scientific knowledge, but to follow in his revered father's footsteps. If the past is any prediction of the future, then Andrew's curiosity will continue to question and investigate the world around him, and, in time, he will hopefully achieve immortality by passing on what he has learned.

This dissertation is dedicated to my parents.

ACKNOWLEDGMENTS

I thank Prof. David Shalloway, Prof. Gerald Feigenson, Prof. Jeff Buboltz, Prof. Jack Freed, Prof. Barbara Baird, and Prof. Benjamin Widom for being scientific advisers. In addition, I thank the GANN Fellowship, NIH training grants in Molecular Biology and Biophysics, Graduate School Fellowships, and my parents for financial support. Finally, I thank my family, friends, and lab members for morale support. If I had the space and time, I would like to acknowledge all the random people I have met at Cornell and Ithaca who, in some way or another, have guided and shaped me on the path of enlightenment, but that process would take an eternity and would never guarantee to converge. In summary, I quote the great Sir Isaac Newton, "If I have seen further it is only by standing on the shoulders of giants".

TABLE OF CONTENTS

LIST OF FIGURES

LIST OF TABLES

Chapter One: Introduction

Phase science, the study of phase behavior, traces it roots to the development of equilibrium thermodynamics over a hundred years ago. Most of this early work focused on gases and their changes in state with changing pressure and temperature. Phase science originated from Gibbs' work on the equilibrium thermodynamics of mixtures with the phase rule and the concept of a chemical potential, Van der Waals' work with his equation of state, and Korteweg's work on the theory of plaits. However, with the advent of quantum and statistical mechanics, work in phase science shifted more to the molecular understanding of phase structure and critical phenomena. Theoretical work on multi-component multi-phase systems was few and far between; however, experimental work into phase behavior, aided by regular binary solution theories, blossomed because of the huge industrial and practical applications, especially in materials science, colloid and interface science, and chemical engineering. But as chemical systems of interest become more complex, especially in biology, a better understanding of phase science and the thermodynamics of mixing was necessary.

I. Phase Behavior

The phase behavior of a thermodynamic system is defined by stating the number, composition, and nature of the coexisting phases (1). Phase diagrams graphically depict phase behavior in terms of the state variables, such as temperature, pressure, and mole fractions of the chemical components. The governing law for construction and interpretation of phase diagrams is Gibbs' phase rule. The phase rules gives the number of intensive thermodynamic variables that need to be independently fixed (i.e. thermodynamic degrees of freedom) to uniquely specify the equilibrium state of an open system if the number of chemical components and phases are known. Topologically, the degrees of freedom (f) specify the geometrical

representation or dimension of the thermodynamic system in the space of the intensive variables. For example, f = 0 (invariant) is a point, f = 1 (univariant) is a line or curve, and f = 2 (divariant) is a field, plane, or surface. Another phase rule, Duhem's Theorem, states that the total number of independent variables (intensive and extensive) to uniquely specify the equilibrium state of a closed system (if the total composition is known and constant) is two. The two phase rules, combined with the Morey-Schreinemaker Coincidence Theorem (or Schreinemaker's Rules) concerning the limits of stability, provide the tools to construct and interpret thermodynamically consistent phase diagrams in the space of intensive variables. Similar rules can be applied to phase diagrams in the space of extensive variables (2). In this work we are mostly interested in compositional phase diagrams, where the state variables are the intensive mole fractions (ratios of the extensive mole numbers), and first-order phase transitions, or systems consisting of coexisting phases.

Compositional phase diagrams depicting first-order phase transitions consist of coexistence curves and tie-lines. Coexistence curves divide the phase diagram into coexistence regions, which contain compositions at which the system separates into two or more phases. Therefore, a coexistence region is labeled by the number of coexisting phases, such as a two-phase region or three-phase region. A coexistence curve is also called a connodal because the curve is the locus of connodes, which are the stable compositions of the coexisting phases (3). For two-phase regions the coexistence curve, sometimes called the binodal, is divided into two phase boundaries, with each phase boundary the locus of connodes (binodes) for that particular phase (Figure 1.1). Two phase boundaries can join at a critical point, which is a point on the coexistence curve where the compositions of the two coexisting phases are equal and defines the limit of stability of the two phases (Figure 1.1). Two other curves through the coexistence region and emanating from the critical point are the

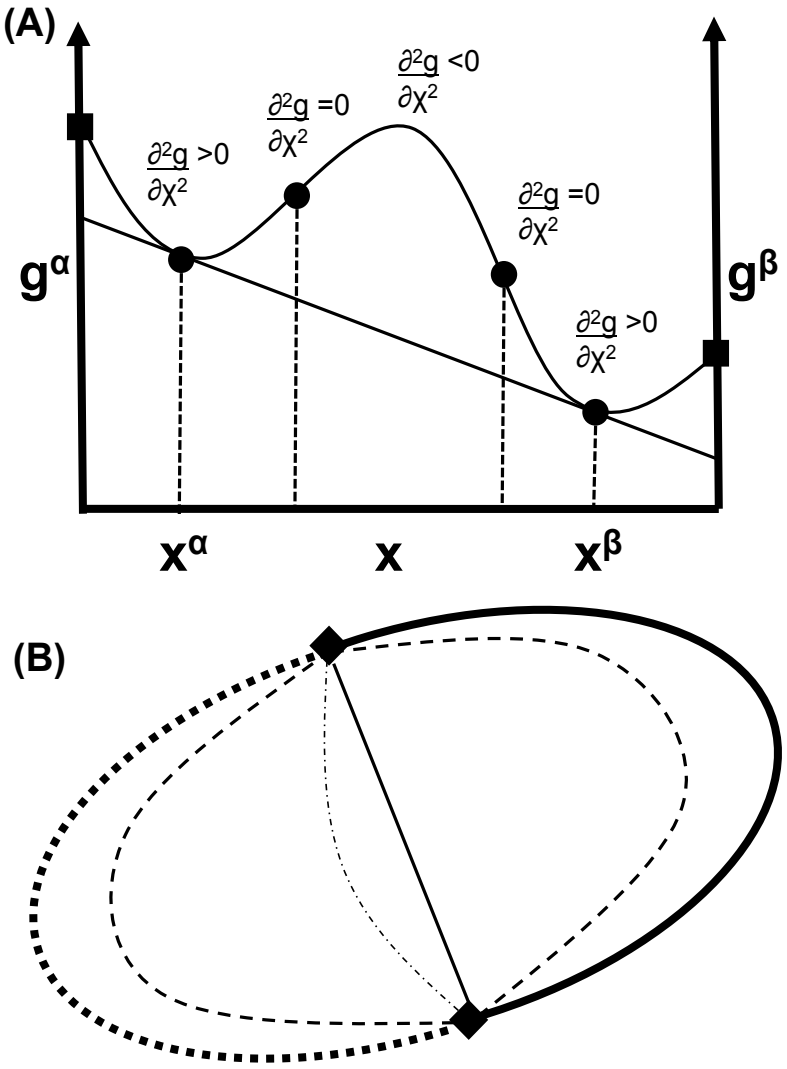

Figure 1.1: Phase behavior and phase diagrams involve the topological description of free-energy surfaces. A) The "common-tangent" construction determines the phase boundaries (x^{α} and x^{β}) in binary systems and phase stability is defined by the curvature (i.e. 2nd derivative) and the change in curvature of the free-energy surface (g^{α} and g^{β} are the free energies of the alpha and beta phases, respectively). B) In ternary systems, the coexistence curve, divided into two phase boundaries (thicker solid and dotted lines) with two critical points (diamonds), and the spinodals (thinner dashed lines) for two-phase coexistence regions are projections from the free-energy surface to the phase diagram (i.e. Gibbs triangle). The phase percolation (continuity) threshold curve (thin dash-dot line), where the connectivity of the phases change at some point along a tie-line, and the equal phase fraction curve (thin solid line connecting the diamonds), where the material fractions of the two phase are equal (i.e. 50%) along a tie-line, can also be defined.

spinodals (Figure 1.1). The area between the phase boundaries and the spinodals is the meta-stable region, where the system is locally stable but globally unstable (with respect to coexisting phases). The area between the spinodals is the unstable region, where the system is both locally and globally unstable. In addition, a line passing through the coexistence region and connecting the two coexisting connodes is called a tie-line. Therefore, since there are an infinite number of connodes on each phase boundary, any two-phase region is divided up into an infinite number of tie-lines. To the author's knowledge, the only thermodynamic restriction of tie-lines, as dictated by the phase rule, is that they cannot intersect.

Along with chemical equilibrium (the compositions at which coexisting phases have the same chemical potentials), the nature of a phase is another important aspect of the phase behavior of a thermodynamic system. The nature of a phase is its dynamic and thermodynamic (typically mechanical) properties, and is generally different for every phase composition; however, two states each in one phase but with different compositions can be labeled the same phase because the nature of the phases is similar. For example, two nematic liquid crystals of different composition can have different average rotational diffusion coefficients, compressibility moduli, and viscosities but are still in the nematic phase. Also, experimentally, the identification of a phase in a coexisting multi-phase system relies on the different nature of the phases. Phase identification helps determine the number of coexisting phases, which is required for both delineating the coexistence region and positioning the region relative to other coexistence regions. Unfortunately, some common methods used to construct compositional phase diagrams, such as FRET and magnetic resonance spectroscopy, are indirectly related to the compositions of the coexisting phases. This unavoidable reality complicates the experimental detection of a compositional first-order phase transition because the measurement can sometimes vary substantially with

composition although the system exists in one phase. An ideal measurement for detecting coexisting phases would not vary much with composition but vary greatly with the nature of the phase.

An extension to, and possibly separation from, the concept of the nature of a phase is the mechanical phase behavior, both equilibrium and non-equilibrium, of a thermodynamic system. The spatial distribution of coexisting phases and their interfacial phenomena are becoming increasingly important in understanding complicated thermodynamic systems, especially in biology where colloids dominate. Mechanical equilibrium is defined as the equivalence of pressure fields between coexisting phases, but it also pertains to the minimization of surface and line tensions. An alternate definition is when a phase's area/volume/curvature ceases to change for constant thermodynamic elastic moduli (e.g. for bending and compression), surface tension, and line tension, which all depend on the compositions of the coexisting phases. In contrast, mechanical non-equilibrium (i.e. phase dynamics) is when the phase's area/volume/curvature continues to change over time; for example, shape transitions of phase domains and phase separation from an initially homogeneous but meta-stable state. A mechanically non-equilibrium state can often be mistakenly assumed to be equilibrated because the rate of change is either so slow as not to be noticed or actually halted in a kinetically trapped state. Assurance in reaching equilibrium requires absolute control of state variables, waiting a sufficiently long time regarding the system dynamics, and convergence to the same state when perturb away from the nominally equilibrated state.

Phase percolation is an important mechanical property of multi-phase systems; it refers to when a phase is either disconnected within the other phase or continuous and surrounding the other phase. The percolation threshold for a phase is the minimum material fraction of that phase at which it first becomes continuous (4);

therefore, the property is implicitly defined along a thermodynamic tie-line, where the material fractions of each phase changes but the compositions of the phases do not. When applied to a three-component two-phase coexistence region, the percolation threshold is a locus of points within the coexistence region and forms a curve (Figure 1.1, the phase percolation threshold curve). Along with the material fraction of the phase, the percolation threshold depends on the size and shapes of the phase domains, being lower when the phase is made up of asymmetric domains (4). The material fraction of a phase is not the same as the area fraction; they are related through the equilibrium area per molecule, which, for example, is typically higher for a fluid phase than a solid phase.

II. Lipid Phase Behavior

Research into lipid phase behavior has been on-going for over fifty years because of the importance these molecules play in the structure and function of biological membranes. The hundreds of different amphiphilic lipids varying in size, shape, and polarity yield an astonishing array of different phases when mixed with water, both three-dimensional and quasi two-dimensional. The two main classes of lipids relevant to this study are the phospholipids, glycerophospholipids and sphingophospholipids, and sterols, particularly cholesterol. Chemically, phospholipids contain an anionic or neutral (zwitterionic) headgroup and a nonpolar (hydrocarbon) region, either consisting of one acyl chain (lysophospholipids) or two acyl chains of varying length and unsaturation (i.e. number of carbon double bonds). At physiological conditions, some phospholipids (e.g. phosphatidylethanolamine) naturally exist in a three-dimensional phase, such as the inverted hexagonal phase (H_{II}), but most phospholipids exist in the quasi two-dimensional phase, the lipid bilayer (5). Depending on temperature, hydrocarbon unsaturation, headgroup to hydrocarbon size ratio, headgroup ionization (which depends on pH and salt

concentration), and water content, transitions between the H_{II} and bilayer phase can occur (Figure 1.2). The lipid bilayer is a "quasi" two-dimensional phase because it consists of two coupled molecular layers; a true two-dimensional phase is one molecular layer (e.g. the lipid monolayer at an air-water interface). Although three-dimensional lipid phases may have some physiological functions, particularly in vesicle fusion/fission during exocytosis/endocytosis, the lipid bilayer is most relevant biologically because it is the natural physiological state for all cell membranes. Of concern in this study is the phase behavior that can exist within the lipid bilayer; these phases are called lamellar phases.

At room temperature and pressure, pure saturated phospholipid systems are naturally either in a liquid-disordered phase (called L_d) or a gel phase, of which there are a few (L_β, $L_{\beta'}$, and $P_{\beta'}$), depending on acyl chain length and asymmetry (i.e. the two chains differ in length). Pure unsaturated phospholipid systems can exist in either phase depending on the type of unsaturation (trans or cis carbon double bonds) but generally exist in the L_d phase, although they can form gels at lower temperatures. At very high temperatures, beyond the L_d-H_{II} phase transition, all phospholipids will generally decompose into lysophospholipids and fatty acids before mixing appreciably with water. The lamellar, isobaric phase diagrams of binary mixtures, either of unsaturated and saturated phospholipids or two saturated phospholipids each with symmetric acyl chains but of different length, with mole fraction and temperature state variables generally show a two-phase coexistence region of L_d and gel phases within some range of temperatures (Figure 1.3). The tie-line orientations for these phase diagrams are trivial since all tie-lines are perpendicular to the vertical temperature axis (parallel to the mole fraction axis) as a consequence of thermal equilibrium. According to Gibb's phase rule for binary phospholipid mixtures with variable temperature, a three-phase eutectic or peritectic may exist, with the most likely

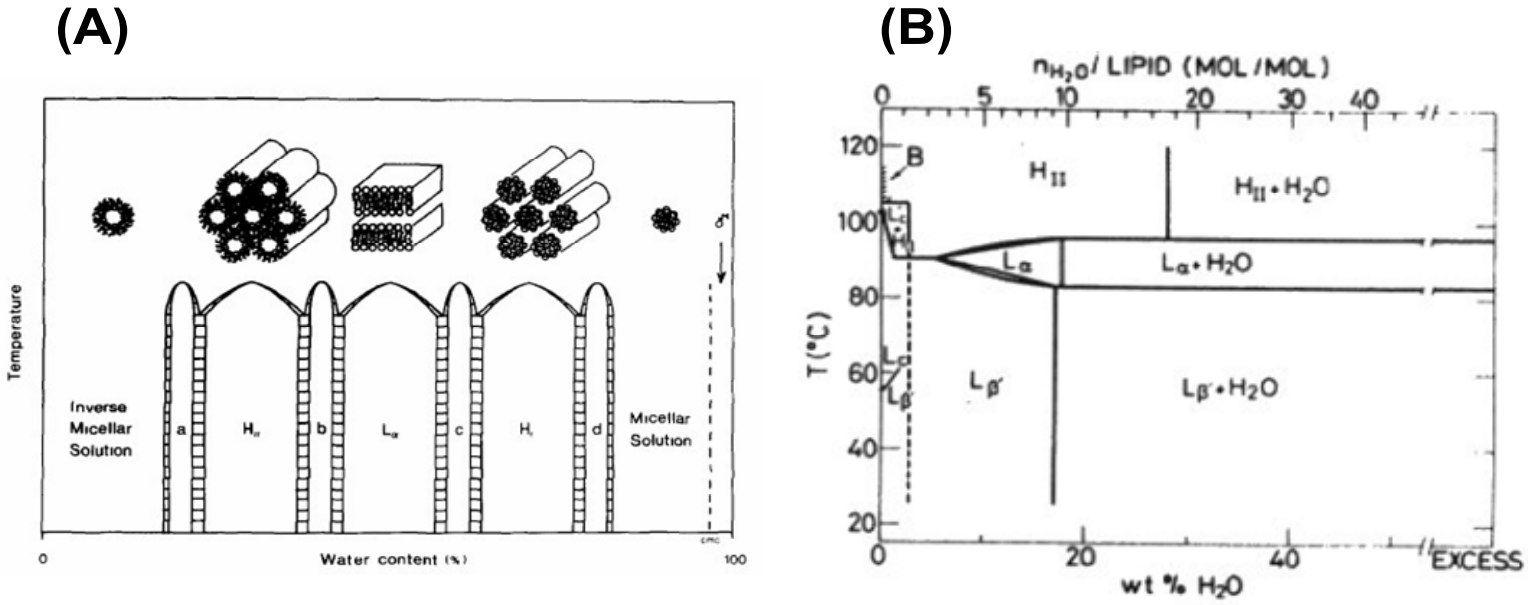

Figure 1.2: Lyotropic (i.e. dependent on water content) phase diagrams of phospholipids that can form non-bilayer phases. A) In a hypothetical temperature/water content binary phase diagram (from reference 6) typical for lysophospholipids the phase boundaries are nearly vertical because the phase transitions are strongly dependent on water content and weakly dependent on temperature. The three-dimensional structures of the phases are also shown. B) On the contrary, in the binary phase diagram for the DAPE/water system (from reference 7) the phase boundaries are nearly horizontal because the phase transitions are strongly dependent on temperature and weakly dependent on water content.

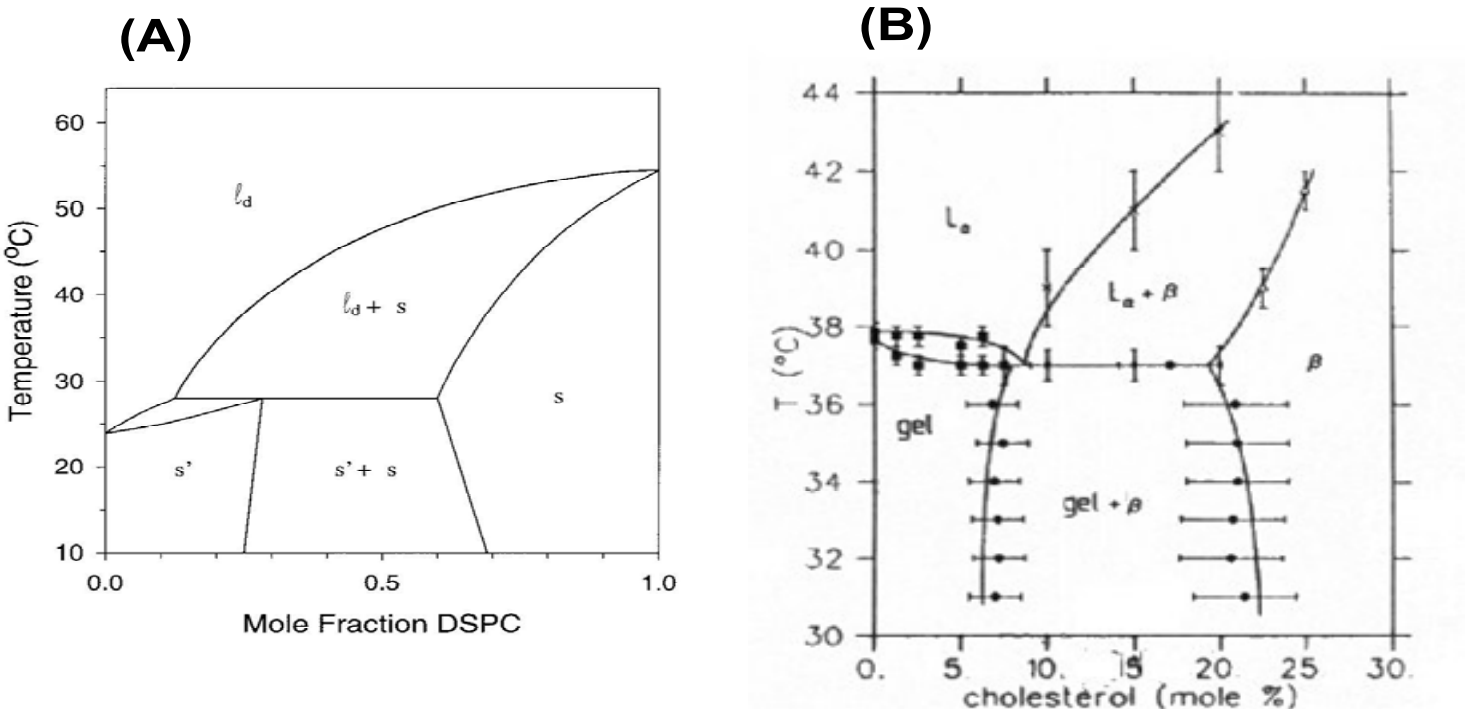

Figure 1.3: The temperature phase diagrams of some binary lipid mixtures can show invariant points of three coexisting phases. A) DMPC/DSPC phase diagram (from reference 8) shows a pertectic phase transition (gel 1 [s'] → L_d + gel 2 [s] with increasing temperature) around 27°C. B) DPPC/cholesterol phase diagram (from reference 9) shows a eutectic phase transition (L_d [L_α] → gel + L_o [β] with decreasing temperature) around 37°C.

observance at lower temperatures being two solid phases and a fluid; but, this has only been observed in a few mixtures (Figure 1.3A). Some mixtures of gel-favoring phospholipids at room temperature and cholesterol do show eutectic behavior, where the three coexisting phases are two fluid phases and a gel (Figure 1.3B). The addition of cholesterol to either pure phospholipid systems or binary phospholipid mixtures results in another fluid lamellar phase, called a liquid-ordered phase (L_o), with physical properties similar to both L_d and gel phases.

A number of ternary (three-component) lipid phase diagrams for phospholipid bilayers have been explored and constructed (10-15). The ternary mixtures studied consist of an unsaturated phospholipid that favors an L_d phase at room temperature, a saturated phospholipd that favors a gel phase at room temperature, and cholesterol, because they are better models for biological membranes than binary systems. The saturated phospholipid/cholesterol and saturated/unsaturated phospholipid binary mixtures typically contain a two-phase coexistence region. The existence of a two-phase coexistence region for unsaturated phospholipid/cholesterol binary mixture depends on the type of unsaturated phospholipid. According to Gibbs' phase rule at constant temperature and pressure, a three-component lipid mixture can exhibit three-phase coexistence with variable mole fractions. This three-phase coexistence region within the Gibbs' composition triangle is itself a triangle with each vertex representing the composition of the L_d, gel, or L_o phase. Based on the phase behavior of the binary mixtures, represented by the sides of the composition triangle, and the phase rule, the possible topologies of the phase behavior for the ternary mixture can be constructed (Figure 1.4). Furthermore, three two-phase coexistence regions and three-phase triangles have been confirmed for some of the ternary lipid mixtures studied (11-15). Research into the mechanical phase behavior of bilayers has paralleled research into lamellar phases given the importance of bilayer deformation of biological membranes

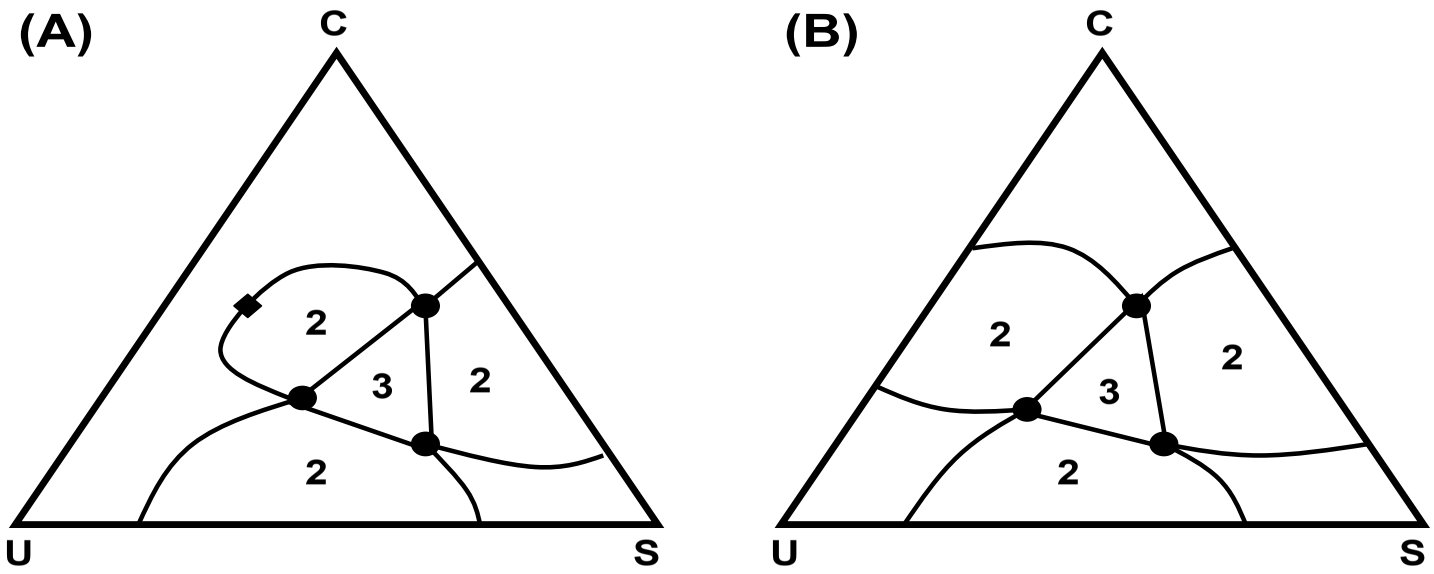

Figure 1.4: Ternary phase diagrams (S = saturated lipid, U = unsaturated lipid, and C = cholesterol) containing a three-phase coexistence region (the internal triangle labeled "3") can only be in two topological forms depending on the presence or absence of a two-phase coexistence region within the binary mixtures (represented by the edges on the composition triangle). A) If the U/C binary mixture (edge connecting vertices U and C) does not contain a two-phase coexistence region (i.e. line segment), then the two-phase coexistence region (areas labeled "2") corresponding to the missing phases within the ternary composition space that intersects the three-phase coexistence region must have a miscibility critical point (black dot). B) If the U/C binary mixture does contain a two-phase coexistence region (line segment on that edge), then the extension of that region must intersect the three-phase coexistence region without a miscibility critical point.

(e.g. the red blood cell). Extensive experimental work on vesicles (i.e. closed bilayers) was performed to investigate mechanical properties, such as thermodynamic moduli and surface tension, and theoretical models were developed to explain these results, but the initial focus was on variable temperature and the fluid lamellar phase (16-18). However, vesicles consisting of coexisting lamellar phases manifested their own unique mechanical behaviors and illustrated the important effects of the interfacial line tension between coexisting phases (19, 20). Also, the mechanical phase behavior of lipid bilayers is coupled to its chemical phase behavior. The dynamic process of phase separation into chemically distinct coexisting phases can influence the final mechanical state of the bilayer, and the mechanical properties and deformations of the bilayer can influence the compositions of the coexisting phases (21-23).

III. Biological Relevance of Lipid Phase Behavior

Biological membranes are complex mixtures of lipids and proteins within the physical structure of a phospholipid bilayer (24, 25). Across all living systems, these bilayers exist within a wide range of temperatures and pressures, and contain a huge variety of lipid species. Furthermore, in the eukaryotes specifically, the composition of the cell membrane (i.e. plasma membrane) and internal membranes (i.e. golgi, ER, nucleus, etc) varies across animals, plants, and fungi. To add to the complexity, even the outer and inner leaflets (the two individual monolayers of the bilayer) of the cell membrane have different lipid compositions. Just as varied as their compositions, these membranes are involved in a number of important biological functions, such as protein sorting, signal transduction, and exocytosis/endocytosis (26, 27). Therefore, in adherence to the current structure-function paradigm in biology, understanding the physical structure of biological membranes will help to understand their function. The original physical model of biological membranes, called the “fluid mosaic”

model, was that the phospholipid bilayer was a fluid but passive barrier where the membrane-associated proteins were allowed to diffuse freely across the membrane in performing their functions. However, because of the observation of certain polarized biological membranes of different composition (e.g. apical and basolateral sections of the cell membrane of epithelial cells), coexisting phases in model membranes, and a new fluid cholesterol-rich phase (i.e. L_o phase); a modified model of the phospholipid bilayer was proposed (27). This new model states that the bilayer consists of at least two coexisting lipid phases, with the domains of one phase, called "lipid rafts", enriched in sphingolipids and cholesterol (28). The proposed function of this laterally heterogeneous membrane was the selective concentration or separation of membrane proteins to affect their biochemical reactions (28). The vision was that raft domains were interspersed and diffusing within a continuous non-raft phase; however, the exact material fraction of the membrane that was the raft phase and the sizes and shapes of the raft domains was to be determined.

Fluorescence microscopy and single-particle tracking experiments of raft-associated proteins within biological membranes have demonstrated that these bilayers contain heterogeneous environments, but the results cannot distinguish between coexisting phases or non-ideal mixing/aggregation (24, 25, 29). Fluorescence microscopy and spectroscopy experiments on model membranes, both on well-defined ternary lipid mixtures containing cholesterol that model the plasma membrane (30-33) and mixtures composed of lipids extracted from biological membranes (31, 34-36), show that bilayers can exhibit coexisting fluid L_o and L_d phases with rounded domains of visible size. Therefore, the nature of the raft phase in biological membranes and the L_o phase in model membranes may be similar. However, phase continuity (i.e. L_o domains disconnected in an L_d background or L_d domains disconnected in a L_o background) depends on the material fraction of the coexisting phases, the size and

shape of the phase domains, and the kinetic process of phase separation (37). Furthermore, the partitioning of proteins between coexisting phases thought important to raft function will likely depend on both phase composition and elasticity, such as curvature and expansion/compression (38-40).

The outstanding questions on the lipid raft model concern the stability of lipid rafts, either a thermodynamic equilibrium phase or a kinetic non-equilibrium phase with a controlled structure/lifetime, and the size/shape of lipid rafts, which most likely will depend on both proteins and the mechanical properties of the bilayer (38-40). However, because of the immense complexity of biological membranes, studies must rely on model membrane systems, both lipids only and lipid/protein mixtures, to determine how these macromolecules interact in controlling the lateral heterogeneity of the bilayer. Also, better experimental methods and theories need to be developed to construct and interpret phase diagrams of complex mixtures. Moreover, researching the chemical and mechanical phase behavior of lipid mixtures within a bilayer structure is necessary to understand the structure and function of biological membranes.

REFERENCES

1. Laughlin, R. G. *Tetrahedron* **1997**, 53, 9997.
2. Shimizu, A. *J. Phys. Soc. Jpn*. **2008**, 77, 104001.
3. Levelt Sengers, J. M. H. "The theory of plaits on surfaces – Korteweg" Ch. 5 in *How fluids unmix: Discoveries by the School of Van der Waals and Kamerlingh Onnes*; Royal Netherlands Academy of Arts and Sciences: Amsterdam, 2002.
4. Vaz, W. L. C.; Almeida P. F. F. *Curr. Opin. Struct. Bio.* **1993**, 3, 482.
5. Gruner, S. M. *Ann. Rev. Biophys. Biophys. Chem.* **1985**, 14, 211.
6. Seddon, J. M. *Biochim. Biophys. Acta.* **1990**, 1031, 1.
7. Seddon, J. M.; Cevc G.; Kaye R. D.; Marsh D. *Biochemistry* **1984**, 23, 2634.
8. Pokomy, A.; Almeida P. F. F.; Vaz W. L. C. *Biophys. J.* **2001**, 80, 1384.
9. Vist, M. R.; Davis, J. H. *Biochemistry* **1990**, 29, 451.
10. Feigenson, G. W.; Buboltz, J. T. *Biophys. J.* **2001**, 80, 2775.
11. Zhao, J.; Wu, J.; Heberle, F. A.; Mills, T. T.; Klawitter, P.; Huang, G.; Costanza, G.; Feigenson, G.W. *Biochim. Biophys. Acta* **2007**, 1768, 2764.
12. de Almeida, R. F. M.; Fedorov, A.; Prieto, M. *Biophys. J.* **2003**, 85, 2406.
13. Veatch, S. L.; Keller S. L. *Biochim. Biophys. Acta* **2005**, 1746, 172.
14. Veatch, S. L.; Gawrisch, K.; Keller, S. L. *Biophys. J.* **2006**, 90, 4428.
15. Pokorny, A.; Yandek, L. E.; Elegbede, A. I.; Hinderliter, A.; Almeida, P. F. F. *Biophys. J.* **2006**, 91, 2184.
16. Needham, D.; Evans, E. *Biochemistry* **1988**, 27, 8261.
17. Evans, E. A.; Waugh, R. *J. Colloid Interf. Sci.* **1977**, 60, 286.
18. Seifert, U. *Adv. Phys.* **1997**, 46, 13.
19. Julicker, F.; Lipowsky, R. *Phys. Rev. E* **1996**, 53, 2670.
20. Sackmann, E.; Feder, T. *Mol. Membr. Biol.* **1995**, 12, 21.

21. Seifert, U. *Phys. Rev. Lett.* **1993**, 70, 1335.

22. Taniguchi, T. *Phys. Rev. Lett.* **1996**, 76, 4444.

23. Jiang, Y.; Lookman, T.; Saxena, A. *Phys. Rev. E* **2000**, 61, R57.

24. Feigenson, G. W. *Biochim. Biophys. Acta* **2008**, 1788, 47.

25. Feigenson, G. W. *Annu. Rev. Biophys. Biomol. Struct.* **2007**, 36, 63.

26. Van Meer, G.; Voelker, D. R.; Feigenson, G. W. *Nat. Rev. Mol. Cell Bio.* **2008**, 9, 112.

27. Edidin, M. *Annu. Rev. Biophys. Biomol. Struct.* **2003**, 32, 257.

28. Simons, K.; Vaz, W. L. C. *Annu. Rev. Biophys. Biomol. Struct.* **2004**, 33, 269.

29. London, E. *Biochim. Biophys. Acta* **2005**, 1746, 203.

30. Samsonov, A. V.; Mihalyov, I.; Cohen, F. S. *Biophys. J.* **2001**, 81, 1486.

31. Dietrich, C.; Bagatolli, L. A.; Volovyk, Z. N.; Thompson, N. L.; Levi, M.; Jacobson, K.; Gratton, E. *Biophys. J.* **2001**, 80, 1417.

32. Veatch, S. L.; Keller S. L. *Biochim. Biophys. Acta* **2005**, 1746, 172.

33. Zhao, J.; Wu, J.; Heberle, F. A.; Mills, T. T.; Klawitter, P.; Huang, G.; Costanza, G.; Feigenson, G.W. *Biochim. Biophys. Acta* **2007**, 1768, 2764.

34. de la Serna, J. B.; Perez-Gil J.; Simonsen, A. C.; Bagatolli, L. A. *J. Biol. Chem.* **2004**, 279, 40715.

35. Baumgart, T.; Hammond, A. T.; Sengupta, P.; Hess, S. T.; Holowka, D. A.; Baird, B. A. *Proc. Natl. Acad. Sci.* **2007**, 104, 3165.

36. Montes, L-R.; Alonso, A.; Goni, F. M.; Bagatolli, L. A. *Biophys. J.* **2007**, 93, 3548.

37. Vaz, W. L. C.; Almeida P. F. F. *Curr. Opin. Struct. Bio.* **1993**, 3, 482.

38. Hancock, J. F. *Nat. Rev. Mol. Cell Bio.* **2006**, 7, 456.

39. Janmey, P. A.; Kinnunen, P. K. J. *Trends Cell Biol.* **2006**, 16, 538.

40. McMahon, H. T.; Gallop, J. L. *Nature* **2005**, 438, 590.

Chapter Two: Compositional Phase Diagram and Mechanical Phase Behavior of a Ternary Lipid Mixture

I. Introduction

The basic structure of biological membranes is the phospholipid bilayer, which forms spontaneously in an aqueous environment because of the hydrophobic effect, or the very low entropy of the phospholipids' exposed hydrophobic acyl chains in water. Thermodynamically, the phospholipid/water mixture phase separates into a phospholipid bilayer, which at the solubility limit (i.e. saturation) contains a very small amount of water, and an aqueous solution containing a very small amount of individual phospholipids. Both the bilayers and individual phospholipids tend to adsorb to the container interfaces, with the bilayer predominately at the container/water interface and the phospholipids at the air/water interface. Also, because of this very low solubility in water, the freely floating phospholipid bilayer can be regarded as a closed system thermodynamically, in that there is no net transfer of phospholipids between the bilayer and the surrounding water, and closed physically, in that there are no "edges" of exposed acyl chains. Depending on the pressure, temperature, and composition (mole fraction of the chemical components), the phospholipid bilayer can itself exist in different states of matter and/or phase separate into different coexisting phases (1). In general, all state variables are important for the phase behavior of biological membranes; however, specifically, composition is the main variable in determining the phase behavior of membranes that exist at a constant physiological temperature and pressure but contain hundreds of different phospholipids (2).

A rigorous understanding of the phase behavior of multi-component phospholipid bilayers at constant temperature and pressure necessitates the experimental construction of compositional phase diagrams, which graphically

represents a thermodynamic system with changing composition. An N component closed system is represented by an N−1 dimensional simplex; therefore, a binary system (N = 2) is represented as a line segment (dimension = 1) and a ternary system (N = 3) is represented by a triangle (dimension = 2). A point within this compositional simplex represents the total composition of the system; furthermore, if the system consists of coexisting phases, this point lies within a phase coexistence region, a set of points bounded by a coexistence curve that is divided into phase boundaries. For our purposes, the phase diagram represents just the bilayer, where we can ignore the water component of the surrounding aqueous phase when the polar headgroups of the phospholipids are saturated, or, in other words, when the bilayer resides in excess water. Experimentally, the sample examined is the colloidal system of the bilayer and surrounding water, so the first step in phase diagram construction is varying the composition of the bilayer. However, because of the very low solubility of phospholipids in water, it is impractical to vary the composition of the bilayer simply by the external addition of lipid to the sample; therefore, a sample is made for each composition studied and with each new component the number of samples required increases geometrically. Also, to delineate phase boundaries with sufficient accuracy and to reveal subtle or unexpected features of composition-driven phase behavior, samples should be made over the full range of relevant compositions and in sufficiently small compositional increments. Therefore, even for binary or ternary bilayer systems, a large number of samples are required. The second step in phase diagram construction is choosing the best experimental method for detecting a phase transition from one phase to another, distinguishing between one phase and coexisting phases, and efficient expedience. Because of the large number of samples required, an efficient experimental method must have a relatively fast data acquisition rate per sample to insure completion of the phase diagram within a reasonable amount of time.

In addition, phase diagram construction should employ several independent experimental methods, so that the phase boundaries and any novel features of the phase behavior can be corroborated.

The experimental method of Confocal Fluorescence Microscopy (CFM) has been successfully implemented in the construction of compositional phase diagrams of ternary phospholipid bilayer mixtures (3-6). The method is applied to samples of giant uni-lamellar vesicles (GUVs), which are single bilayers closed into an approximate sphere (diameter > 10 μm). Because of the large size of GUVs, coexisting phases within the bilayer can be visually observed using CFM provided that the sizes of the phase domains are larger than the wavelength of the fluorescence. In addition, the method relies on the fluorescent probes partitioning favorably into one phase to give contrast between coexisting phases. Multiple probes can be used, with each probe selected to label a single phase. Because of the selective partitioning of the fluorescent probes, CFM can distinguish one phase from coexisting phases, but cannot detect a phase change from one phase to another one phase. Also, CFM cannot distinguish one phase with homogeneous fluorescence with coexisting phases that are nanoscopic in size (i.e. domain size dimensions on the order of nanometers).
In addition to studying the chemical equilibrium of phase separation (i.e. coexisting phases of different compositions), CFM can be used to study the mechanical phase behavior, both equilibrium and non-equilibrium, of phase-separated GUVs by visually observing the shapes, sizes, interactions, and transitions of the coexisting phase domains (7-14). An important consideration in interpreting this mechanical phase behavior is the sources of stress within and across the bilayer of the GUV. Both the hydrophobic effect and the normal pressure differential from osmosis contribute to the surface tension of a GUV (15, 16). Along with the surface tension, an additional source of stress within the bilayer stems from the closed topology of the GUV (17).

The closure of the bilayer imposes a curvature that generally opposes the intrinsic or spontaneous curvature, which is typically near zero for symmetric bilayers (i.e. the two monolayers have the same composition). Experimentally, the surface tension and normal pressure differential are very difficult or impossible to control during GUV formation and subsequent phase separation; therefore, the mechanical properties of the GUV are left to vary while the strain energy is dissipated during relaxation to equilibrium.

The experimental method of Electron Spin Resonance (ESR) has also been successfully implemented in the construction of compositional phase diagrams of binary systems (18-21). The method is typically applied to samples of multi-lamellar vesicles (MLVs), which are many closed bilayers concentrically arranged. In excess water (i.e. the phospholipid headgroups are supersaturated) the multiple bilayers interact weakly with each other, so each bilayer can be assumed as independent. Because of sample preparation, the main difference from GUVs is the absence of a normal pressure differential across the bilayer of MLVs resulting in low surface tension. The data from a bilayer sample obtained from an ESR experiment is a spectrum from a spin-probe, which is generally a lipid that has been chemically modified by attachment of a free radical. An ESR spectrum is independent of phase domain size and is sensitive to a phase transition from one phase to another one phase. However, a spectrum cannot distinguish individual phases present in the coexisting phases without sophisticated spectral analysis and application of the linear superposition model for physical properties of multi-phase systems. This model assumes that the spin-probe partitions between the distinct (possibly submicroscopic or nanoscopic) coexisting phases, and only an insignificant fraction of the probe is at the interface between the phases. Therefore, because the probe is reporting on the internal physical properties of a phase, the spectrum from a multi-phase system is the

linear combination of the spectra from each coexisting phase weighted by the fraction of total spin-probe in that phase. The process of locating phase boundaries essentially involves finding the optimal basis set of this linear combination with appropriate constraints (such as normalization and non-negativity of the experimental spectra in the absorption mode). Then, with the proper basis set, the compositions of the coexisting phases can be located; however, so far, this approach can only be applied to binary systems with variable temperature, where the directions (i.e. slopes) of the required thermodynamic tie-lines are known (22-24). Furthermore, the best results are obtained when the spectra from the coexisting phases are significantly different from each other and the spin-probe's partition coefficient is not much different from unity.

In this work we applied CFM and ESR to thoroughly construct a nearly complete compositional phase diagram and examine interesting mechanical phase behavior of a ternary bilayer mixture. This mixture, brain-sphingomyelin /dioleoylphosphatidylcholine/cholesterol (SPM/DOPC/Chol, chemical structures in Figure 2.1), was chosen because 1) it models the outer leaflet (i.e. outer monolayer of the bilayer) of the animal cell plasma membrane, and 2) previous studies using fluorescence microscopy showed visible fluid phase coexistence at specific compositions of this mixture (14, 25). The constructed phase diagram, consisting of three two-phase coexistence regions and a three-phase coexistence region, is very similar to other published ternary phase diagrams of bilayer mixtures (4, 5). Also, CFM was used to investigate phase percolation (connectivity or continuity), an important property of multi-phase systems and biological membranes. In addition, CFM observations of phase morphology and dynamics, such as long-range order/patterns among fluid phase domains, unusual shapes of solid phase domains, phase transitions within fluid-fluid phase coexistence, and light-induced phase separation have shed light on the mechanical phase behavior of this bilayer system.

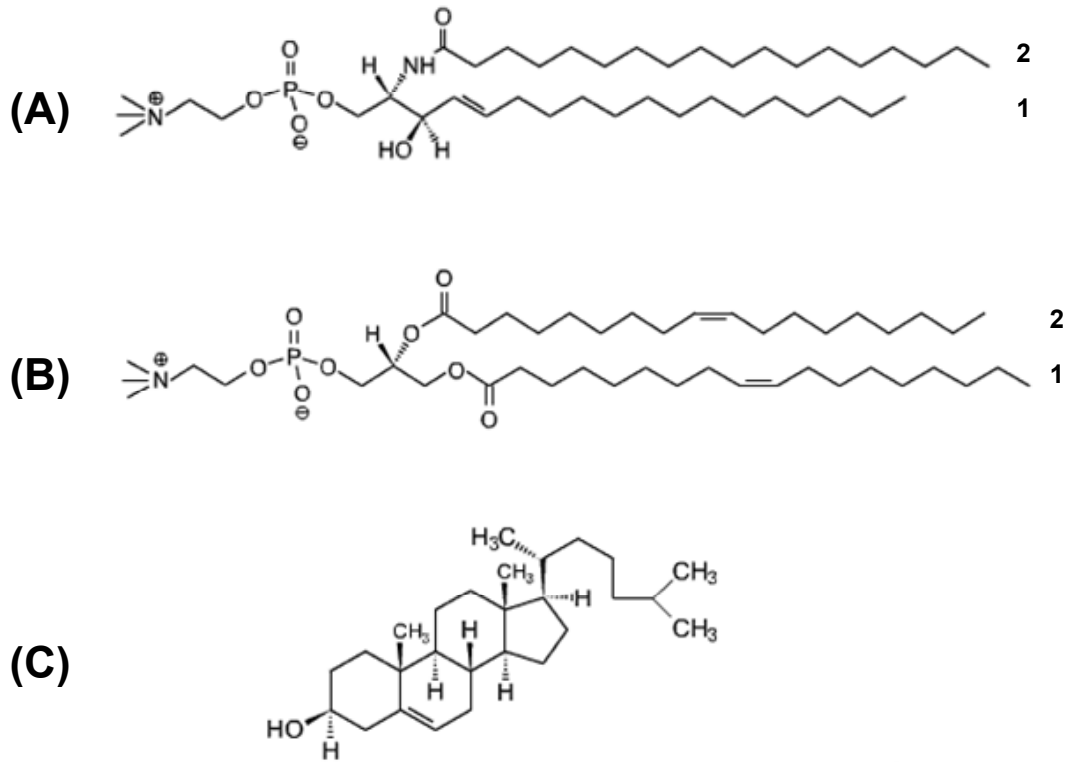

Figure 2.1: The chemical structures of the lipids used in this study. A) Sphingomyelin is based on the molecule sphingosine (acyl chain 1), which always has a 16 carbon acyl chain. The amide linked acyl chain (acyl chain 2) is variable in chemical structure for naturally derived brain sphingomyelin (SPM in this study). The structures (carbon # : unsaturation position) and proportions are the following (Avanti Polar Lipids): 1.7% 16:0, 45.5% 18:0, 5.1% 20:0, 7.2% 22:0, 6.0% 24:0, 6.3% 24:1, 28.2% other, which is most likely chain length < 16. Most amide linked acyl chains are unsaturated and 18 carbons long (structure pictured); however, there is considerable chain mismatch with position one, which can lead to significant interdigitation between the two monolayers of the bilayer. B) The glycerophospholipid, dioleoylphosphatidylcholine (DOPC), is based on the molecule glycerol. The acyl chains (#1 and #2) are symmetric and unsaturated, each 18 carbons long with a double bond between position 9 and 10 along the chain. C) Cholesterol is a type of sterol only found in animal cell membranes.

Elucidating the phase behavior of this model membrane system may provide valuable information in understanding the structure and dynamics of real biological membranes.

II. Experimental Details

A. Materials

The phospholipids (SPM and DOPC) and the spin label 1-palmitoyl-2-(16-doxyl stearoyl) phosphatidylcholine (16PC) were purchased from Avanti Polar Lipids, Inc. (Alabaster, AL). Cholesterol was obtained from Sigma-Aldrich (St. Louis, MO). The fluorescent probes 1,1'-dieicosanyl-3,3,3′,3′-tetramethylindocarbocynanin perchlorate (C20:0-DiI) and 1-hexadecanoyl-2-(4,4-difluoro-5,7-dimethyl-4-bora-3a,4a-diaza-*s*-indacene-3-pentanoyl)-*sn*-glycero-3-phosphocholine (16:0,Bodipy)-PC were obtained from Invitrogen (Eugene, OR). Stock solutions of the lipids were prepared by diluting or dissolving the shipped stock in chloroform in a sealable vial. Purity > 99% of the stock solutions was determined by thin-layer chromatography developed in chloroform/methanol/water = 65:25:4 (by volume) for phospholipids, hexane/diethyl ether/chloroform = 7:3:3 for cholesterol, and chloroform/methanol = 9/1 for C20:0-DiI. All materials were used without further purification, and all solvents used were HPLC grade. The purity of lipid stock solutions was checked every three months. The concentration of the phospholipid stock solutions was determined by a slightly modified procedure for the "determination of total phosphorous" published on Avanti Polar Lipid, Inc.'s website for technical information (http://www.avantilipids.com/TechnicalInformation.html). The concentration of the cholesterol stock solution was determined from an accurate mass (± 0.1mg) of the powdered cholesterol stock and the preparation of the solution in a 50 mL ± 0.05 volumetric flask. The concentrations of fluorescent probe stocks were determined by absorption spectroscopy using an HP 8452A spectrophotometer

(Hewlett-Packard, Palo Alto, CA). Extinction coefficients used were 143,000 M^{-1} cm^{-1} at 549 nm for C20:0-DiI and 91,800 M^{-1} cm^{-1} at 504 nm for (16:0, Bodipy)-PC (from Invitrogen).

B. Sample Preparation of GUVs and Observation/Imaging by CFM

GUV samples were prepared by the method of "gentle hydration" (26). Briefly, measured volumes of the lipid and both fluorescent probe stocks were dispensed using a Hamilton repeating dispenser into glass test tubes using a 50 μL Hamilton syringe to give the desired lipid composition and a probe concentration equal to 0.1 mol% of the total lipids. The "gentle hydration" method requires charged lipids to obtain GUVs; therefore, the DOPC stock contained 10% DOPG, which was chosen because both lipids have a similar gel-fluid transition temperature (≈ −20°C). The lipid/probe solutions were dried from organic solvent into a thin film by rotary vacuum at 55°C, well above the gel-fluid transition temperature of SPM (≈ 41°C). Residual solvent was removed by high vacuum for 1 h. The dry film was then gently hydrated by wet N_2 gas for 45 min at 55°C. Pre-warmed buffer (10 mM KCl, 2 mM PIPES, 1 mM EDTA, pH 7.0) was added, and the sample incubated under argon for ≈24 h at 55°C to produce GUVs. The samples were placed in a Styrofoam box to slowly cool to room temperature (23°C) before a few μl, ringed by high-vacuum silicone grease, were deposited on a glass microscope slide and covered with a no. 1 coverslip. The sample was allowed to settle for a few minutes before observation. The GUV samples were initially observed under the eyepiece illuminated with the Hg arc lamp. CFM images of selected GUVs were obtained with an MRC600 confocal fluorescence microscope (Bio-Rad, Hercules, CA) in a series of z-sections (0.5 μm increments) by alternating laser excitation (488 nm for (16:0, Bodipy)-PC and 543 nm for C20:0 DiI) and fluorescence emission collected through the confocal aperture into separate green/red channels with a 560-nm dichroic beamsplitter, and emission filters

of 522/35BP for Bodipy-PC and 586LP for C20:0-DiI. The objective was an Olympus 40x water immersion, numerical aperture 0.75.

C. Determination of Phase Boundaries by CFM

To determine phase boundaries by CFM the coexisting phases must be visible (i.e. the size of the phases, at least in one dimension, must be greater than the wavelength of the fluorescence (400-700 nm)), hereafter referred to as microscopic. The use of more than one fluorescent probe facilitates the identification of the phases (L_d, gel, or L_o) by correlating the probe's chemical structure with the observation of which phase the probe preferentially partitions, along with the probe's partitioning behavior in other lipid systems. However, the probe's partitioning behavior alone is not enough to conclusively identify a phase because the partition coefficient is also dependent on composition not just the nature of the phase (27). Also, if the probe partitions strongly into one phase to provide enough contrast, then only one probe can be used to observe two coexisting phases. Therefore, the identification would be that one phase is the "bright" phase and the other phase is the "dark" phase regardless of the nature of the phases.

The procedure we used to determine phase boundaries in the SPM/DOPC/Chol system was straightforward. Initially, samples were prepared in a grid of 15% mole fraction increments of SPM out of total phospholipid (i.e. $\xi_{SPM}/(\xi_{SPM} + \xi_{DOPC})$) and 5% mole fraction increments of cholesterol, then afterward at many different compositions. Replicates (2-3) of the same sample, each prepared on glass slides, were observed under the confocal fluorescence microscope. The entire slide illuminated with the Hg arc lamp was scanned using the eyepiece and if the majority of GUVs observed showed microscopic phase separation, then the composition was recorded as within a coexistence region, and conversely if not. Representative GUVs at each sample composition were imaged and saved.

D. Sample Preparation of MLVs and ESR Spectra Collection

Spin-labeled lipid MLVs consisting of SPM, DOPC, and cholesterol were prepared as follows. Measured volumes of lipid stocks and the spin-label stock were dispensed using a Hamilton repeating dispenser into glass test tubes using a 50 μL Hamilton syringe to give the desired lipid compositions. The concentration of spin-label in the lipid dispersion was 0.2% of the total lipids. These lipid-chloroform solutions were then converted to lipid-buffer suspensions by Rapid Solvent Exchange (28). The buffer used was 50 mM Tris, 10 mM NaCl, and 0.1 mM EDTA at pH 7.0. The samples were stored under an argon atmosphere in the dark at room temperature for at least 24 hours to reach equilibrium. After a few days the samples were centrifuged and the pellets were transferred to 1.5–1.8-mm-diameter × 100-mm-length glass capillaries with excess buffer. After the samples were centrifuged in the capillaries, the supernatant (excess buffer) was removed to less than a millimeter above the pellet and the ends of the capillaries were flame sealed. ESR spectra were obtained on a Bruker Instruments EMX ESR spectrometer at a frequency of 9.3 GHz at room temperature (≈23°C). The ESR capillary was placed inside a 2mm NMR tube which was marked to position the sample pellet in the middle of the resonator. This configuration allowed for efficiency and consistency in switching samples, tuning, and sample measurements. The spectrometer settings for all samples were as follows: center field = 3477 G, sweep width = 120 G, microwave power = 2 mW, modulation frequency = 100 KHz, modulation amplitude = 0.5 G, resolution (points) = 1024. The number of scans for each spectrum varied, but all spectra were aligned with respect to magnetic field and normalized before analysis.

E. Determination of Phase Boundaries in Binary Systems by ESR

Assuming the linear superposition model applies, the method to determine phase boundaries in binary systems from ESR spectra involves the separation of multi-

component ESR spectra into a number of linearly independent spectral components. In the literature this process of component separation is called either self-modeling curve resolution (SMCR) or multivariate curve resolution (MCR) (29). The method has been applied to uv-vis absorbance spectra of chemical mixtures to determine the individual component spectra; however, it has not been applied to determine compositional phase boundaries in model membrane systems. Therefore, we applied a rudimentary version of MCR to ESR spectra along the SPM/DOPC and SPM/Chol binary axes in the SPM/DOPC/Chol lipid system with encouraging results that warrants further development of the method.

Before analysis, the derivative ESR spectra were integrated into absorbance spectra and then normalized to unit area. Each absorbance spectrum is converted into an absorbance data vector, which is a discretization of the absorbance intensity versus magnetic field. The ESR data vectors from sample compositions along the binary axis were organized into a spectral data matrix, **S**, with the number of rows (M) equal to the number of discrete magnetic field values and the number of columns (N) equal to the number of compositional points sorted by mole fraction from 0 to 1. This data matrix has the following structure,

$$\mathbf{S} \equiv \left[\mathbf{S}^{\alpha} \quad \mathbf{S}^{\gamma} \quad \mathbf{S}^{\beta}\right], \qquad \text{(Eqn. 2.1)}$$

where $\mathbf{S}^{\alpha}$ is the matrix of spectral data within the one-phase region of the alpha phase, $\mathbf{S}^{\beta}$ is the matrix of spectral data within the one-phase region of the beta phase, and $\mathbf{S}^{\gamma}$ is the matrix of spectral data within the alpha + beta coexistence region. A priori the phase boundary spectra that partition the data matrix into these three regions are unknown; however, ordering the columns of the data matrix by increasing mole fraction and knowing that a two-phase region is flanked by one-phase regions determines the matrix structure. In addition, the constraints imposed on the **S** matrix were non-negativity (i.e. positive definite) and closure (i.e. normalization),

$$S_{ij} \geq 0, \forall\, i = 1,\ldots,M \text{ and } j = 1,\ldots,N$$
$$\left\| S_j \right\| = \sum_{i=1}^{M} S_{ij} = 1 \qquad \text{(Eqn. 2.2)}$$

The non-negativity constraint reflects the fact that absorbance intensities are defined as non-negative scalars; therefore, negative intensities that occur within the noise of the baseline are set to zero. The closure constraint is just the discrete version of the integral normalization of the absorbance spectra to unit area rescaled by a constant magnetic field interval,

$$\int_{-\infty}^{\infty} \mathrm{S(B)}\, dB \approx \sum_{i=1}^{M} S_{ij} \Delta B_i = \Delta B \sum_{i=1}^{M} S_{ij} = 1$$

Under the linear superposition model, the coexistence spectra, $\mathbf{S}^{\gamma}$, are a convex linear combination of the phase boundary spectra,

$$\begin{aligned} &\mathbf{S}_j^{\gamma} = f_j^{\alpha} S^{\alpha} + f_j^{\beta} S^{\beta} \\ &\mathbf{S}^{\gamma} \subset \mathbf{S} \\ &S^{\alpha} \in \mathbf{S}^{\alpha}, S^{\beta} \in \mathbf{S}^{\beta} \end{aligned} \quad , \qquad \text{(Eqn. 2.3)}$$

with constraints on the coefficients,

$$\begin{aligned} &f_j^{\alpha} + f_j^{\beta} = 1 \\ &0 \leq f_j^{\alpha} \leq 1 \\ &0 \leq f_j^{\beta} \leq 1 \end{aligned} \quad , \qquad \text{(Eqn. 2.4)}$$

where f^{α} is the fraction of total spin-probe in the alpha phase, f^{β} is the fraction of total spin-probe in the beta phase, S^{α} is the alpha phase boundary spectrum, and S^{β} is the beta phase boundary spectrum. With the definitions,

$$\begin{aligned} &\mathbf{B} \equiv \begin{bmatrix} S^{\alpha} & S^{\beta} \end{bmatrix} \\ &\mathbf{f} \equiv \begin{bmatrix} f_j^{\alpha} & f_j^{\beta} \end{bmatrix}^{\mathrm{T}} \end{aligned} , \qquad \text{(Eqn. 2.5)}$$

the coexistence spectra can be written in matrix form,

$$\mathbf{S}^{\gamma} = \mathbf{B} \bullet \mathbf{f} , \qquad \text{(Eqn. 2.6)}$$

where **B** is a M×2 matrix and **f** is an 2×X matrix (X is the number of coexistence spectra). An approximation to the **S** data matrix, $\mathbf{S}^{*}$, which includes the full

compositional range (i.e. includes the alpha and beta one-phase regions) can be written,

$$\mathbf{S}^* = \mathbf{B} \bullet \mathbf{f}^*,$$

where the $\mathbf{f}^*$ matrix (2×N) is the $\mathbf{f}$ matrix extended by N−X rows of [1 0] for the alpha phase or [0 1] for the beta phase,

$$\mathbf{f}^* = \begin{bmatrix} 1 & 0 \\ \vdots & \vdots \\ f_j^{\alpha} & f_j^{\beta} \\ \vdots & \vdots \\ 0 & 1 \end{bmatrix}^{\mathrm{T}} . \qquad \text{(Eqn. 2.7)}$$

The assumption in this approximation is that the one-phase spectra are the same as their respective phase boundary spectra. Because spectral intensities vary with composition in a one-phase region, the validity of this assumption is obviously questionable; however, the linear superposition model only applies to the data near and within the coexistence region, so a method to determine phase boundaries using data from the entire compositional range must systematically and rationally address the flanking one-phase regions. Furthermore, there is no requirement that the data must explicitly contain the phase boundary spectra or be very near the phase boundary spectra, but there is a requirement that the data overlap both the one-phase regions and the coexistence region.

Therefore, within the previous formulation where $\mathbf{S}$ is known and $\mathbf{B}$, $\mathbf{f}^*$ are unknown, we seek the solution to the following minimization problem,

$$\min_{\mathbf{S}^*} \left\| \mathbf{S} - \mathbf{S}^* \right\|^2 = \left\| \mathbf{S} - \mathbf{B} \bullet \mathbf{f}^* \right\|^2 . \qquad \text{(Eqn. 2.8)}$$

When $\mathbf{B}$ and $\mathbf{f}^*$ are unconstrained, the formal solution to this problem (in the literature called “total least squares”, TLS) is rank reduction through the singular value decomposition (SVD) of the $\mathbf{S}$ data matrix (30). The rank of the $\mathbf{S}^*$ matrix is two.

From the SVD of **S**,

$$\mathbf{S} = \mathbf{U} \bullet \mathbf{W} \bullet \mathbf{V}\,, \qquad \text{(Eqn. 2.9)}$$

the columns of the **U** matrix (M×N) are the orthonormal basis vectors (eigenspectra) for the space of data vectors, the **W** matrix (N×N) is the diagonal matrix of singular values ordered from highest to lowest, and the rows of the **V** matrix (N×N) are the orthonormal basis vectors of the dual space to the space of data vectors. The rank two reduction of the **S** matrix to the solution $\mathbf{S}^*$ involves keeping the two highest singular values and setting the rest to zero,

$$\begin{aligned} \mathbf{S}^* &= \mathbf{U} \bullet \mathbf{D}^2 \\ \mathbf{D}^2 &= \mathbf{W}^2 \bullet \mathbf{V} \end{aligned}\,, \qquad \text{(Eqn. 2.10)}$$

where $\mathbf{W}^2$ is the modified singular value matrix **W** and therefore $\mathbf{D}^2$ is a N×N matrix that can be truncated to a 2×N matrix by removing the N−2 rows of zeros. To conform to the non-negativity and closure constraints (Eqn. 2.2) on the data vectors, the following N number of standard linear least squares problems are solved,

$$\min_{\mathbf{D}_j^2} \left\| \mathbf{S}_j - \begin{bmatrix} U_1 & U_2 \end{bmatrix} \bullet \mathbf{D}_j^2 \right\|^2\,, \qquad \text{(Eqn. 2.11)}$$

with constraints,

$$\mathbf{S}_j \geq \mathbf{0}$$

$$\left\| \mathbf{S}_j \right\| = D_j^2 \left\| U_1 \right\| + D_j^2 \left\| U_2 \right\| = 1 \Rightarrow \sum_{i=1}^{M} S_{ij} = D_j^2 \sum_{i=1}^{M} U_{i1} + D_j^2 \sum_{i=1}^{M} U_{i2} = 1\,,$$

where each $\mathbf{D}_j^2$ is a 2×1 vector, U_1 is the orthonormal basis vector (eigenspectrum) paired with the highest singular value (i.e. first column of **U**), and U_2 is the basis vector paired with the second highest singular value (i.e. second column of **U**). The $\mathbf{D}^2$ matrix contains the coefficients of the linear combination of the eigenspectra. The coefficients are the projections of the data vectors onto the eigenspectra. According to the assumption that the one-phase spectra are the same as the phase boundary spectra, the one-phase spectra should have the same (constant) projected coefficients as the phase boundary spectra. Also, each data vector has a pair of coefficients, but, because

of the normalization constraint, they are dependent, so only the coefficient corresponding to the first eigenspectrum was analyzed for the phase boundary compositions. In this analysis, the phase boundaries of a two-phase coexistence region along a binary axis can be obtained from a plot of the coefficients of the first eigenspectrum for all N data vectors versus the mole fraction for each data vector. Visually, the phase boundaries are the points that mark the transition between a flat region and an increasing/decreasing region. A data-fitting procedure, which employs a simple model relating the $\mathbf{D}^2$ and $\mathbf{f}^*$ matrices, has been developed; however, the method has not been applied in this study because the verification and optimization of the method requires more work. In addition, the solution to Eqn. 2.8 under the constraints on **B** and **f*** (Eqn. 2.2 and Eqn. 2.4, respectively) can be obtained by the method of MCR with alternating least squares, MCR-ALS (31), but this algorithm has not yet been implemented.

The two main obstacles to the future development of this method are the systematic, rational modeling of the one-phase regions and the extension to phase diagrams of more the two components. Regarding the one-phase regions, the relevant question is how to determine if a possible phase boundary spectrum is the true phase boundary spectrum. This determination must involve both a way to distinguish spectra within the same phase but different composition and to detect a phase transition through changing spectral intensities. One degenerate case is when spectra are identical within error (i.e. noise) and each, theoretically, are equally likely to be the true phase boundary spectrum. Another case is when spectra are different but, when looking at a set of data spanning the proposed phase boundary, the changes in the spectral intensities with varying composition within the one-phase region are indistinguishable from the changes in the spectral intensities within the coexistence region caused by the changing fractions of total spin-probe (f^{α} and f^{β} in Eqn. 2.3).

The fractions of total spin-probe are dependent on the probe's partition coefficient and the phase's mole fraction given by the lever rule; therefore, spectral changes through the coexistence region can be modeled because the phase boundary spectra do not change. However, a suitable model for the changes in spectral intensities within a one-phase region must not merely reproduce the predictions of the model for the coexistence region.

Regarding the extension of the method to phase diagrams of three or more components, its most applicable use would be determining the vertices (i.e. invariant or triple points) of the three-phase triangle. In this case, the solution would involve the rank three reduction of the data matrix through its SVD. However, formation of the appropriate data matrix (as in Eqn. 2.1) is nontrivial for a two-dimensional composition space where a compositional point is represented by a vector of mole fractions instead of a scalar mole fraction as for the one-dimensional composition space in a binary system. In addition, three-phase triangles are not only flanked by three one-phase regions that need to be modeled, but also by three two-phase regions.

III. Results

A combination of CFM and ESR experiments have delineated the compositional phase boundaries of three two-phase coexistence regions and inferred the possibility of a three-phase coexistence triangle within the SPM/DOPC/Chol model membrane system. The three two-phase coexistence regions are $L_d + L_o$, L_d + gel, and L_o + gel, and the three-phase coexistence region is $L_d + L_o$ + gel. The phase boundaries of the $L_d + L_o$ region were determined by CFM, and the phase boundaries of the L_d + gel and L_o + gel regions along the binary axes were determined by ESR. Although the phase boundaries determined from CFM and ESR are for different coexistence regions, results from other experiments (data not shown) corroborate the phase diagram. In addition, CFM has revealed other interesting phase behavior

involving phase morphology, phase dynamics, and mechanical phase transitions at specific compositions within the ternary phase diagram. However, these mechanical phase behaviors were not examined thoroughly and directly through a specific experiment, but images were taken in the course of executing the experiment to determine the coexistence curve of the $L_d + L_o$ coexistence region (Figure 2.2). In addition, since this work was completed, most of the results in the SPM/DOPC/Chol lipid system (7, 14, 25) or similar results in other lipid systems (32, 33) have been published. The results presented here are to demonstrate our investigation and interpretation of the phase behavior.

A. Observations of Phase-Separated GUVs Using CFM

Coexistence curve for the $L_d + L_o$ coexistence region

In Figure 2.2 the sample compositions examined for phase coexistence are plotted, with inset CFM images showing representative GUVs at selected compositions exhibiting either microscopic (visible) coexisting L_d and L_o phases or uniform fluorescence, which would indicate either no coexisting phases, which, in this case, is most likely, or nanoscopic coexisting phases. The $L_d + L_o$ coexistence region extends over a wide range of compositions within the center of the phase diagram and bounded by an elliptical coexistence curve. Both L_d and L_o phase domains were circular and diffusive, consistent with fluid-fluid phase coexistence (14, 25). Also, both the fluorescent probes used, (16:0, Bodipy)-PC and C20:0-DiI, partitioned into the same phase at all sample compositions. Because (16:0-Bodipy)-PC partitioned into the L_d phase in other lipid systems (3, 4, 34), the bright phase in Figure 2.2 was identified as the L_d phase. Because it partitioned into solid phases in other lipid systems (3, 4, 34), C20:0-DiI was assumed to partition into the ordered L_o phase. Surprisingly, the contrast between coexisting L_d and L_o phases was often greater for

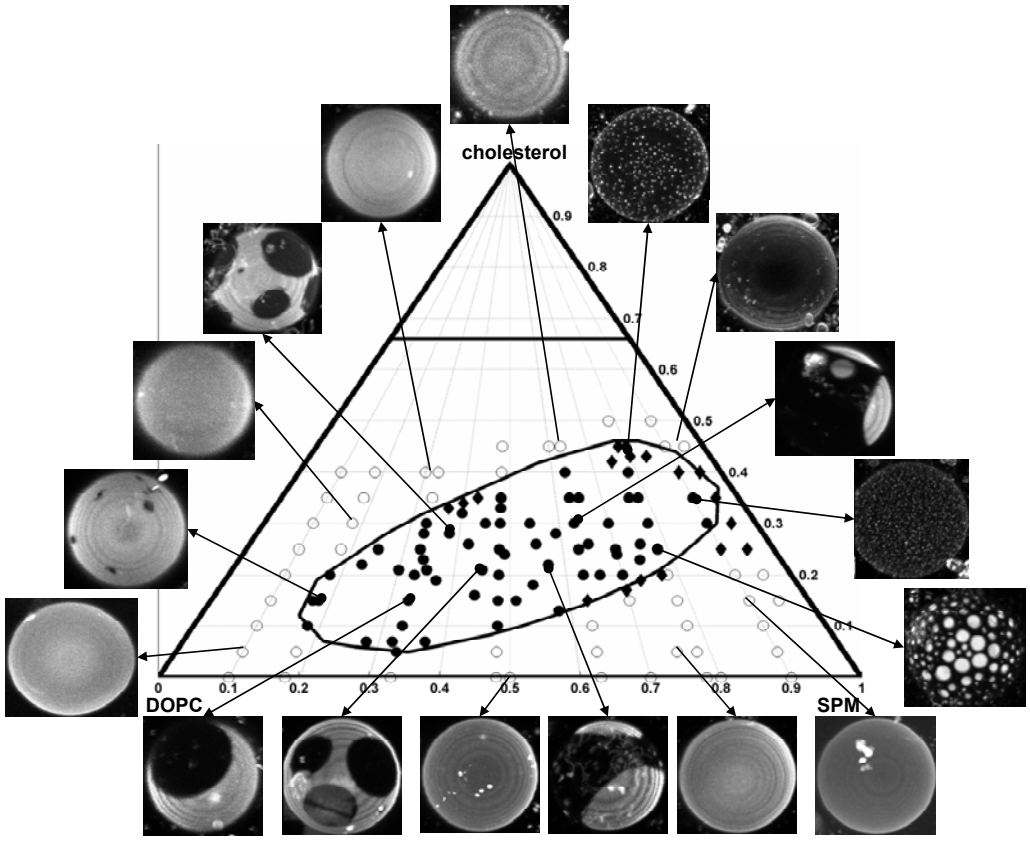

Figure 2.2: The experimental coexistence curve for the $L_d + L_o$ coexistence region in the SPM/DOPC/cholesterol system at 23°C determined by CFM. The sample compositions examined were labeled as having uniform fluorescence (open circles) or coexisting visible phases (filled circles) with circular domains. Some compositions near the coexistence curve (black diamonds) had GUVs that were initially uniform but phase separated over time when illuminated (see Figure 2.7). Insets are CFM images of GUVs (20 – 40 μm in diameter) at selected compositions. Although the GUVS contained both C20:0-DiI and (16:0, Bodipy)-PC, the images show just the DiI fluorescence because of the greater contrast. The sloped grid lines are mole fraction of SPM out of total phospholipid ($\xi^{pl}_{SPM} = \xi_{SPM}/(\xi_{SPM} + \xi_{DOPC})$) and the horizontal grid lines are mole fraction of cholesterol (ξ_{chol}).

C20:0-DiI, suggesting that the partition coefficient into the L_o phase was less for C20:0-DiI than (16:0-Bodipy)-PC. In any case, only one selectively partitioning probe is needed to confirm the coexistence of two phases; therefore, the dark phase was identified as the L_o phase.

The coexistence curve is divided into two phase boundaries, one for the L_o phases and one for the L_d phases. From identifying the bright phase as the L_d phase, compositions near the L_d phase boundary show GUVs with the bright phase dominant in membrane area; similarly, from identifying the dark phase as the L_o phase, compositions near the L_o phase boundary show GUVs with the dark phase dominant in membrane area. Therefore, from the GUV images in Figure 2.2 the L_d phase boundary contains compositions that are high in DOPC and low in cholesterol and the L_o phase boundary contains compositions that are high in SPM and high in cholesterol. Based on the approximate location of the L_o and L_d phase boundaries, the L_o phase contains an upper limit $\xi_{chol} \approx 0.45$, and the L_d phase contains a lower limit $\xi_{chol} \approx 0.05$. Because the DOPC/Chol binary axis does not contain a coexistence region (4, 5), a mixing critical point is located on the section of the coexistence curve near the DOPC/Chol binary axis. The opposite section of the coexistence curve from this critical point and closer to the SPM/Chol axis either contains the two invariant points of the intersecting edge of a three-phase triangle or another mixing critical point, although the former possibility is more likely. The exact location of these points that separate the L_d and L_o phase boundaries cannot be accurately determined from the CFM data.

Phase morphology, dynamics, and mechanical transitions

In addition to mapping coexistence curves, CFM on GUVs provides a way to directly observe the mechanical phase behavior of microscopic coexisting bilayer phases. For nearly all GUVs at compositions within the $L_d + L_o$ coexistence region

the equilibrium shape of the phase domains were circular (Figure 2.2). For compositions where the dominant area fraction is the L_d phase, circular L_o domains of varying size diffused easily and rapidly within the continuous background L_d phase of lower viscosity. The L_o domains frequently and readily fused on contact. For compositions where the dominant area fraction is the L_o phase, many circular L_d domains ranging from tiny to small in size diffused very slowly within the continuous background L_o phase of higher viscosity. If two L_d domains did make contact they generally fused but not always. For compositions within the middle of the coexistence region where the area fractions of the fluid phase are similar, the size distribution of domains and the frequency of domain fusion varied for different GUVs, but seemed to be correlated to which phase had the larger area fraction.

In relation to the area fraction of the phases, an attempt was made to determine the percolation threshold curve through the $L_d + L_o$ coexistence region. This curve is a locus of points, where each point is on one thermodynamic tie-line, which marks the transition where the phase changes continuity, either from a connected background phase to disconnected domains or from disconnected phase domains to a connected background (35). The percolation threshold not only depends on the area fraction of a phase, but also on its size and shape (35). The determination of phase continuity was clear in GUVs from compositions closer to the phase boundaries and near the end of the tie-lines, where the dominant phase in area fraction was also the connected background phase. However, phase continuity could not be determined for compositions within the middle of the coexistence region and presumably near the middle of the tie-lines. Figure 2.3 shows CFM images of GUVs at different compositions where neither phase could be determined as continuous because L_d (L_o) circular domains resided within L_o (L_d) circular domains that resided within other L_d

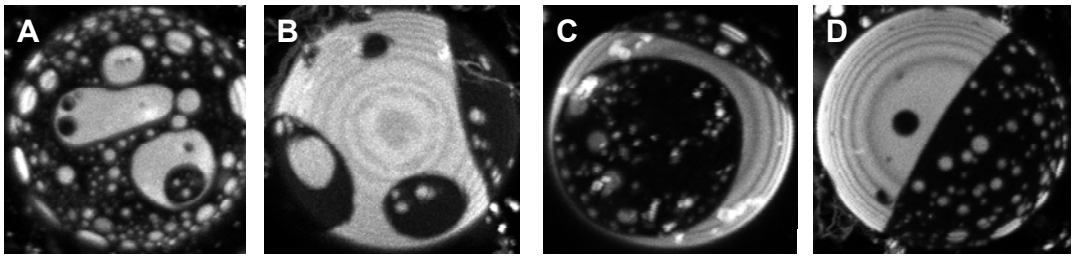

Figure 2.3: Phase percolation (continuity) is indeterminable for many compositions within the middle of the $L_d + L_o$ coexistence region. CFM images of GUVs (A-D) show circular domains of one phase residing within circular domains of the other phase.

(L_o) circular domains. However, the determination of phase continuity could have possibly been made at a later time after sufficient domain fusion into larger domains.

Some GUVs at different compositions with coexisting L_d and L_o phases either consist of long-ranged, spatially patterned circular domains or contain unusual domain shapes. Figure 2.4A shows a GUV consisting of disconnected circular L_d phase domains arranged approximately hexagonally within a continuous L_o phase background. The L_d domains seem have positive curvature (i.e. membrane bends outward). In contrast, Figure 2.4B shows a GUV consisting of disconnected circular L_o phase domains arranged approximately hexagonally within a continuous L_d phase background. In this case, the L_o domains seem to have negative curvature (i.e. membrane bends inward). Another possibility is that the L_o phase has a small positive curvature but the L_d phase has a much greater positive curvature, which makes the L_o domains appear to bend inward. Also, in both images (Figure 2.4A/B) all the circular domains have generally the same diameter and have ceased to diffuse and fuse, although still fluctuate locally. At compositions where the area fractions of the phases are similar, sufficient domain fusion can create large circular domains of one phase that protrude or bud from the other phase (Figure 2.4C). Depending on the composition, the budding domains can be either L_d or L_o. In addition, also depending on composition, domains can bud to such an extent that the GUV will divide into two GUVs, each of a different phase. The GUV in Figure 2.4D consisting of long, thin, curved L_d phase domains of approximately the same widths was extremely rare but very interesting. A certain points along a domain two other domains branched apart at an angle of approximately 120°. Seemingly, most, if not all, of the observed branch points consisted of three emanating domains with an angle of 120° between them. Also, the curvature of some of these domains was great enough to form loops, or two branched domains curved into each other to form the loop. In addition, the GUV also

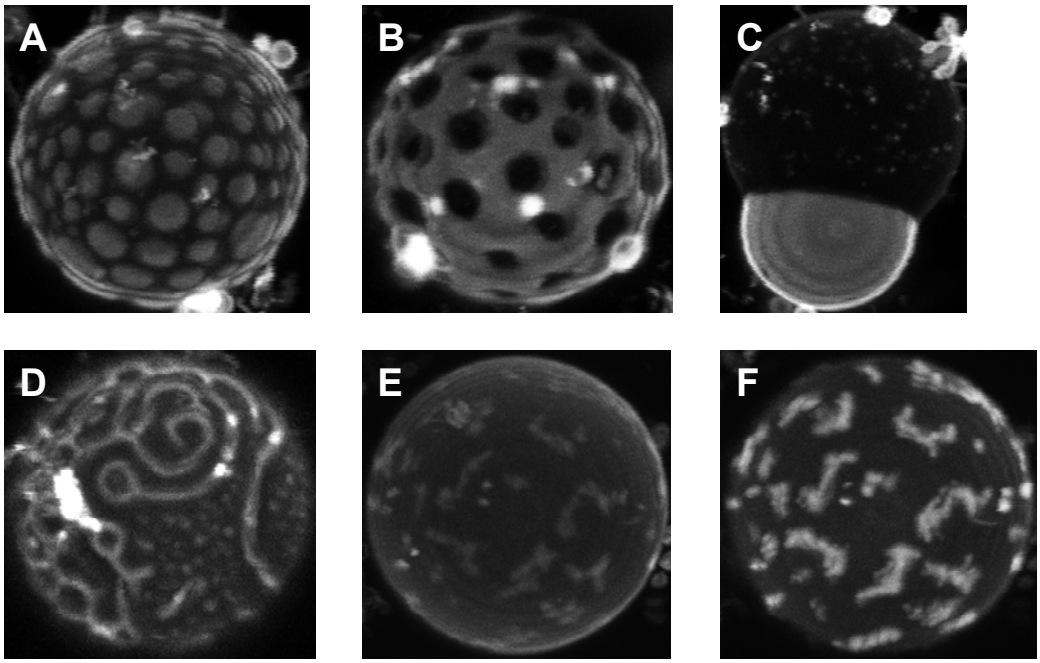

Figure 2.4: GUVs with coexisting L_o and L_d phases exhibit long-range order/patterns. A) Circular L_d phase domains with positive curvature arranged hexagonally within a continuous L_o phase, $\xi^{pl}_{SPM} = 0.40$, $\xi_{chol} = 0.32$. B) Circular L_o phase domains with negative curvature arranged hexagonally within a continuous L_d phase, $\xi^{pl}_{SPM} = 0.64$, $\xi_{chol} = 0.15$. C) An L_d domain budding from a GUV ($\xi^{pl}_{SPM} = 0.65$, $\xi_{chol} = 0.26$) consisting of an L_o phase. D) Possible observation of bubble and stripe L_d phase domains coexisting, $\xi^{pl}_{SPM} = 0.48$, $\xi_{chol} = 0.15$, although seen only once. The same GUV, (16:0, Bodipy)-PC fluorescence on the left (E) and the C20:0-DiI fluorescence on the right (F), showing bright domains with a jagged appearance and a shape mismatch between the two fluorescence channels.

shows a region of small circular L_d domains, but the resolution was not high enough to determine if these domains were hexagonally arranged. The images in Figure 2.4E/F are the same GUV with the left image (E) showing the (16:0, Bodipy)-PC fluorescence and the right image (F) showing the C20:0-DiI fluorescence. Interestingly, the jagged bright domains look similar to gel (solid) domains and have a peculiar zigzag appearance, but the composition is approximately the 1:1:1 SPM:DOPC:Chol ratio, which is well within the $L_d + L_o$ coexistence region. Also, the perimeters of the domains from the two images do not seem to match, with the domain shapes reported from (16:0, Bodipy)-PC being slightly different from the domain shapes reported from C20:0-DiI. However, this GUV was extremely rare, being the only one seen out of all the compositions examined.

Although the three vertices of the presumed three-phase coexistence triangle could not be located using CFM, some GUVs at compositions within the $L_d + L_o$ coexistence region but very near where the three-phase region is expected to be located may contain evidence of a gel phase. Because of the compositional heterogeneity inherent in GUV preparation, the actual composition of a particular GUV from a nominally prepared composition near the three-phase region may actually lie within the three-phase region. If such is the case, the gel phase would be in a minor material and area fraction. The presence of amorphous or angular/linear domain shapes and spatial asymmetries between the two fluorescence channels can be used to identify the gel phase. The top and bottom rows in Figure 2.5 are two GUVs from different compositions near the three-phase region. The first column (A and C) shows the (16:0, Bodipy)-PC fluorescence and the second column (B and D) shows the C20:0-DiI fluorescence. The partitioning behavior of the fluorescent probes was unknown for coexisting L_d and gel phases, but C20:0-DiI was expected to partition into the gel phase (3, 4, 34). The phase domains in the GUV of Figure 2.5A/B were

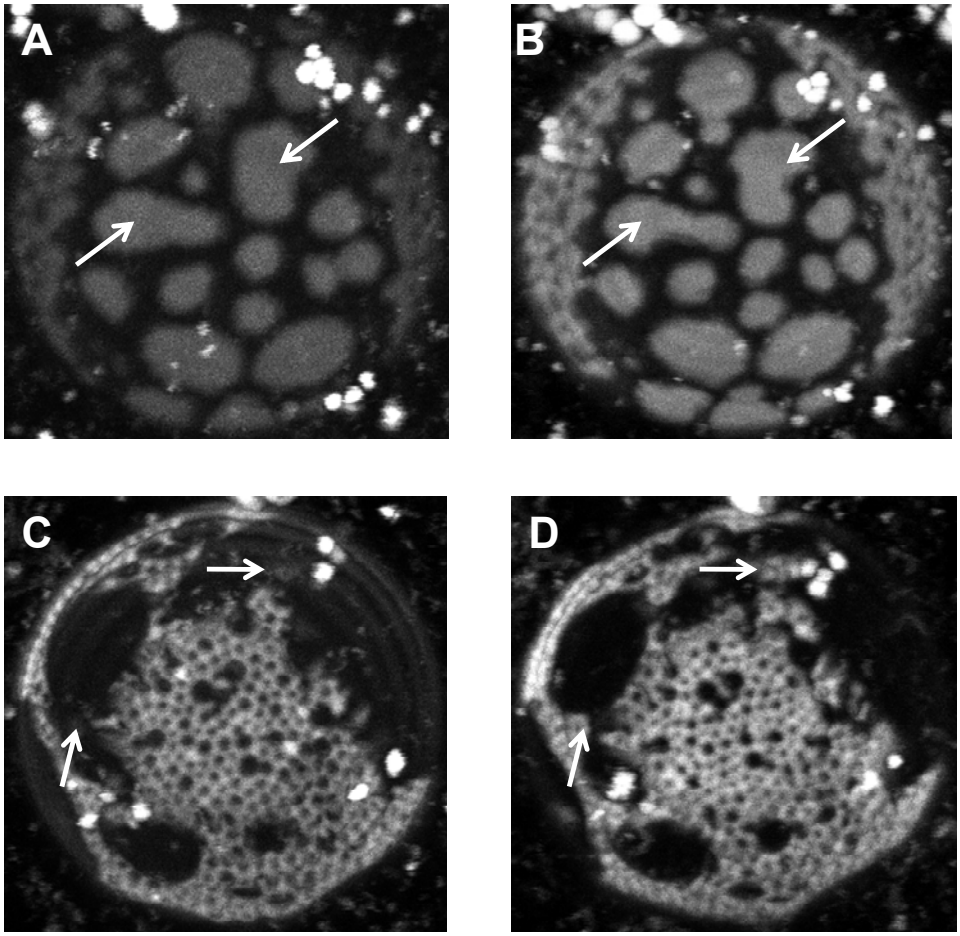

Figure 2.5: Fluorescence asymmetries and amorphous domain shapes may indicate the coexistence of three phases, an L_d, L_o, and a gel. The top row are the CFM images, (16:0, Bodipy)-PC fluorescence on the left (A) and the C20:0-DiI fluorescence on the right (B), of the same GUV ($\xi^{pl}_{SPM} = 0.70$, $\xi_{chol} = 0.17$). The white arrows in A and B point to amorphous L_d domains with a perimeter mismatch between fluorescence channels. The bottom row are the CFM images, (16:0, Bodipy)-PC fluorescence on the left (C) and the C20:0-DiI fluorescence on the right (D), of the same GUV ($\xi^{pl}_{SPM} = 0.78$, $\xi_{chol} = 0.25$). The white arrows in C and D point to areas where fluorescence is one channel is absent in the other channel (i.e. fluorescence asymmetry).

amorphous and some domain border regions containing (16:0, Bodipy)-PC fluorescence did not contain C20:0-DiI fluorescence resulting in a domain perimeter mismatch between the two fluorescence channels. Amorphous domains were also seen in the GUV of Figure 2.5C/D, along with areas that contained C20:0-DiI fluorescence but did not contain (16:0, Bodipy)-PC fluorescence. However, other areas contained (16:0, Bodipy)-PC fluorescence but did not contain C20:0-DiI fluorescence.

At another composition within the $L_d + L_o$ coexistence region near both the L_o phase boundary and the three-phase region, some GUVs were in the process of a mechanical phase transition. In Figure 2.6 the top and bottom rows are two different GUVs from the same composition near the three-phase region. The first column (A and C) shows the (16:0, Bodipy)-PC fluorescence and the second column (B and D) shows the C20:0-DiI fluorescence. As can be seen, the dark L_o phase has the dominant area fraction and forms the continuous background phase. However, the L_d phase consists of many long, thin domains that intersect at small non-circular domains. Over a short amount of time and possibly light-induced (see below) the thin L_d domains split and contract into the non-circular intersecting regions to eventually form only individual circular L_d phase domains. Unfortunately, a time series of this transition could not be obtained because of the speed of the progression. In addition, from the relative fluorescence intensities of the two phases in each fluorescence channel, the partition coefficients of the two probes are very different from each other although both favorably partition into the L_d phase. This observation is typical for compositions with high concentrations of SPM and cholesterol, suggesting that the partition coefficient of the probes change with the compositions of the coexisting phase (i.e. across tie-lines).

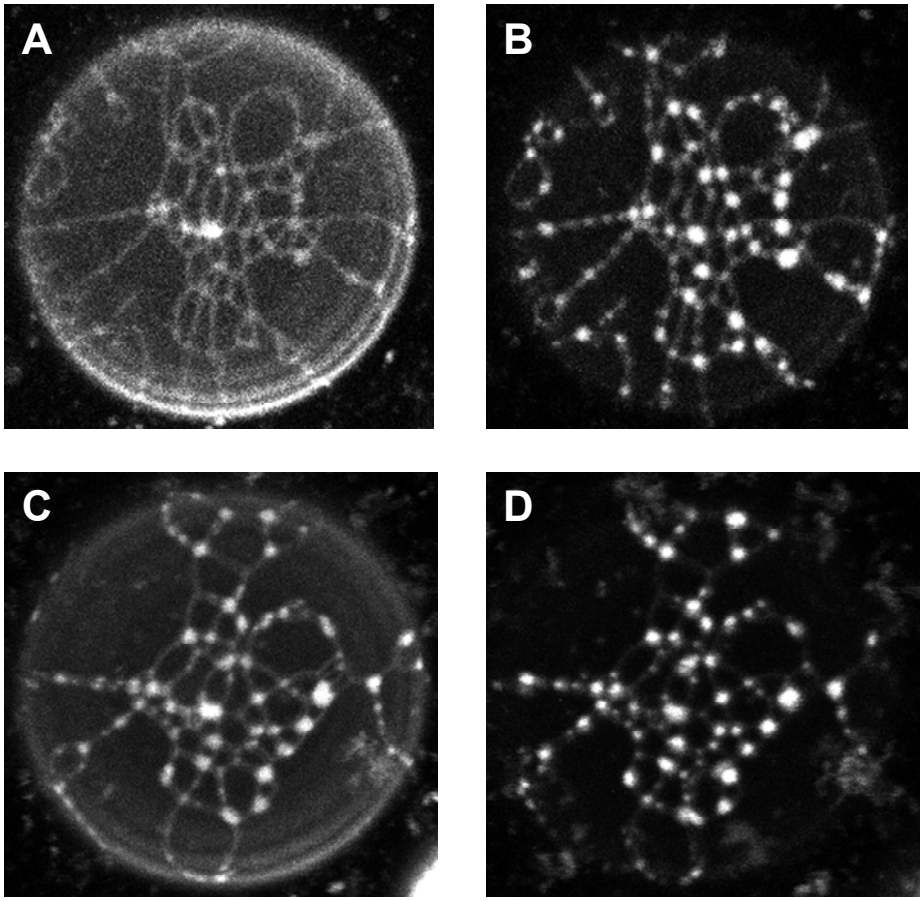

Figure 2.6: At a composition within the $L_d + L_o$ coexistence region near both the L_o phase boundary and the three-phase region ($\xi^{pl}_{SPM} = 0.90$, $\xi_{chol} = 0.30$), light-induced mechanical phase transitions were observed. Two CFM images of the same GUV on the top row and same GUV on the bottom row show the initial network of thin L_d stripe phases intersecting at non-circular domains within a L_o background phase. Images A/C reporting the (16:0, Bodipy)-PC fluorescence and images B/D reporting the C20:0-DiI fluorescence. The L_d phase strings eventually split and contract forming only individual circular L_d phase domains, although this process was not captured in images.

Related to the mechanical phase transitions of coexisting fluid domains, the dynamic process of phase separation was also observed in some GUVs at different compositions near the $L_d + L_o$ coexistence curve and around the vertex of the three-phase triangle separating the $L_d + L_o$ and L_o + gel coexistence regions (black diamonds in Figure 2.2). These GUVs initially appeared homogeneous under the microscope but phase separated over time, seemingly instigated by light excitation of the fluorescent probes. A common progression of this light-induced phase separation is shown in Figure 2.7A-H, which is a series of images of the same GUV at approximately one minute time intervals (the GUV was homogeneous at time zero but was unable to capture an image fast enough before phase separation commenced). The results in Figure 2.7A-D show the initial appearance of many very small L_o phase domains that eventually fuse together into larger domains, resulting in a web or net-like appearance of the L_d phase. In Figure 2.7E two large L_o domains are separated by a thick ring of L_d phase. Figure 2.7E-H shows the thinning, splitting, and contracting of this L_d stripe domain into a circular domain, which is very similar to the mechanical phase transitions observed in relation to Figure 2.6. This progression was typical for different compositions in that the phase separation started with many small domains and continued with domain fusion into larger domains; however, which phase became the continuous background phase depended on the composition. Also, the rate of phase separation varied with composition. In general, the rate of phase separation increased with increasing concentration of SPM and/or cholesterol. Figure 2.7I-L was another interesting progression (at approximately one minute time intervals) of mechanical phase transitions induced by light. Figure 2.7I was the initial appearance and Figure 2.7H-L again shows long thin L_d phase domains of approximately identical widths thinning, splitting, and contracting into circular domains and possibly protruding from the GUV as tubules. Another interesting observation was the out-of-

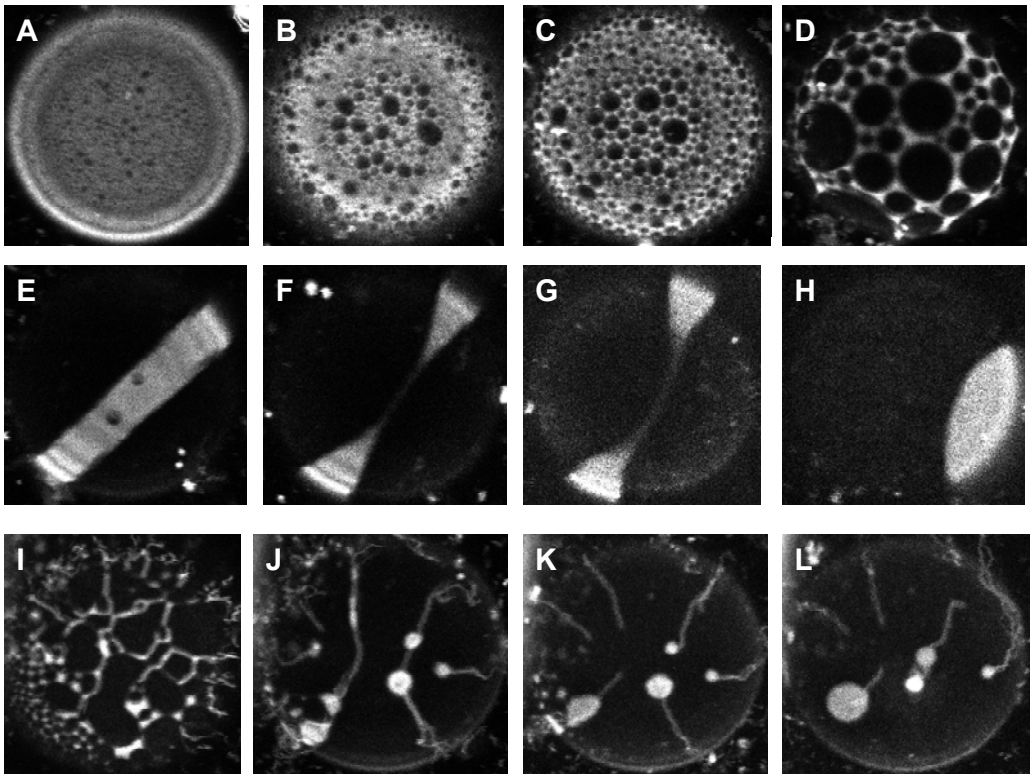

Figure 2.7: Light excitation of the fluorescent probes seems to instigate phase separation in homogenous GUVs at compositions near the $L_d + L_o$ coexistence curve. (A-H) A series of CFM images of the same GUV at one minute intervals showing the initial appearance of small circular L_o domains that eventually fuse together to form one large L_o domain. Also, note the thinning, splitting, and contracting of the wide L_d domain into a circular domain (E-H), which is similar to the transition of the stripe phases shown in Figure 2.6. A series of CFM images in approximately 1 min intervals of the same GUV (I-L) that show light-induced mechanical phase transformations of stripe domains thinning and contracting into circular domains.

plane (i.e. curvature) fluctuation of the bilayer during phase separation. Initially, when just the equatorial section of a homogenous GUV was illuminated, the bilayer was a circle as normally. When the light-induced phase separation commenced, the circle distorted and fluctuated rapidly but eventually returned to a circle. These bilayer curvature fluctuations occurred at many of the compositions where the light-induced phase separation was observed.

Although the progress of the light-induced phase separation exhibited in Figure 2.7A-H was typical for different compositions, a variety of intermediate stages were observed in a closer examination of a specific composition ($\xi^{pl}_{SPM} = 0.9$, $\xi_{chol} = 0.25$). Figure 2.8A-E shows various intermediate stages of phase separation starting from a homogenous GUV at this composition, which is probably within the three-phase coexistence region. The states observed in Figure 2.8A-C were either stable or meta-stable and did not change much over a long time (several minutes until photobleaching rendered the GUV unobservable). For example, the fusion of domains does not always result in circular domains (Figure 2.8A). A stable network of long thin L_d domains can be formed (Figure 2.8B/C). The GUV in Figure 2.8C was similar to those observed in Figure 2.6 but the L_d phase network lasted for a much longer time. A commonality among the GUVs in Figure 2.8A-C and Figure 2.6 is that a combination of L_o domain fusion within a web-like continuous L_d phase structure and the splitting and contraction of thin L_d domains eventual leads to a continuous L_o phase with a mixture of circular and non-circular L_d domains with emanating thin L_d domains, which would again split and contract forming only circular L_d domains. The stages in Figure 2.8D/E were observed from the same GUV at different times and were unique because the domains did not start as many small circular domains but appeared as fluctuating amorphous domains spread across the whole GUV. Also, the fluorescent probe (only (16:0, Bodipy)-PC in this case) seemed to change its degree of

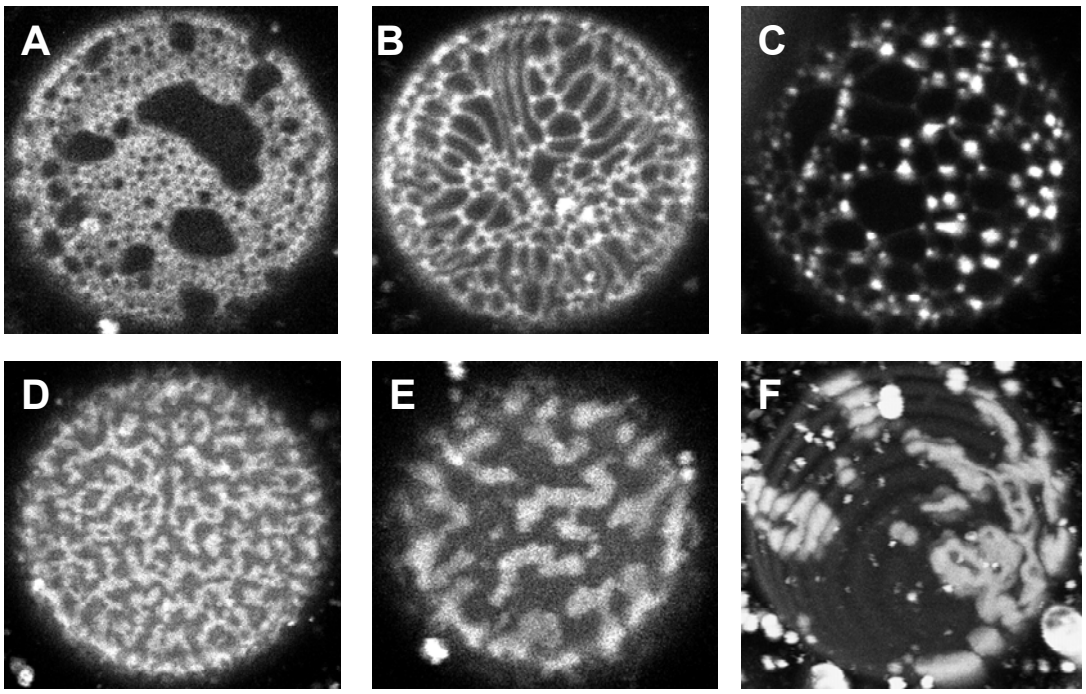

Figure 2.8: Some GUVs at a composition (ξ^{pl}_{SPM} = 0.90, ξ_{chol} = 0.25) within or near the three-phase coexistence region exhibited different intermediate states during light-induced phase separation that were stable for long periods of time. CFM images A-C were labeled with just C20:0-DiI, images D and E were labeled with just (16:0, Bodipy)-PC, and image F contained both probes. A) Domains fusing into large domains that did not immediately circularize. B and C) A stable network of L_d stripe domains of varying width could form. Spinodal decomposition may have been observed (D and E the same GUV). F) A GUV at another composition near the three-phase coexistence region (ξ^{pl}_{SPM} = 0.70, ξ_{chol} = 0.17) that initially showed bright domains that resembled a gel phase, but light excitation caused the domains to break up and circularize.

partitioning into the L_d phase, which resulted in a gradual increase in intensity of the L_d phase concurrently with a gradual decrease of the intensity of the L_o phase. The GUV in Figure 2.8F was from a different composition than the images in Figure 2.8A-D but near the three-phase region. This image shows bright amorphous domains which initially were thought of as gel phase domains, but after being illuminated the domains broke up or dissolved resulting in circular L_o domains in a continuous background of the L_d phase.

All GUVs observed at compositions within the presumed L_d + gel coexistence region were homogeneous (Figure 2.2) when prepared on a microscope slide and observed the same day. However, after a sample at a specific composition was prepared on a microscope slide and left for a day, some rare GUVs did show visible gel phase domains of odd shapes. The images in Figure 2.9A-D were of GUVs from the same composition ($\xi^{pl}_{SPM} = 0.48$, $\xi_{chol} = 0.05$), which is located within the L_d + gel coexistence region (Figure 2.13). Based on the expectation of the fluorescent probes partitioning into the L_d phase, the dark or black phase in these images was identified as some condensed gel phase enriched in SPM. Because their occurrence was very rare, this condensed phase was assumed meta-stable or in a non-equilibrium state. The three-fold symmetric arrangement of the elliptical gel phase domains (i.e. three lobes emanating from a common center) in Figure 2.9A has not been previously observed in any bilayer lipid system. Figure 2.9B shows the gel phase with amorphous domains and Figure 2.9C shows the gel phase with a mixture of elliptical and amorphous domains within a continuous L_d phase, where the folded appearance of the bilayer probably results from the different curvature of the phases. The top of the GUV in Figure 2.9D was in contact with the glass coverslip and formed an homogeneous disk, but, interestingly, elliptical gel phase domains, similar to the ones seen in Figure

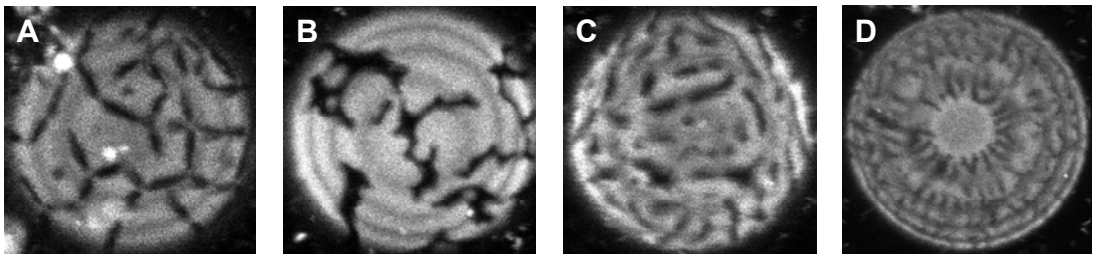

Figure 2.9: A few very rare GUVs showed a SPM-rich gel phase with odd domain shapes at a composition (ξ^{pl}_{SPM} = 0.48, ξ_{chol} = 0.05) within the L_d + gel coexistence region. A) A gel phase with a three-fold symmetric arrangement of elliptical domains (three lobes emanating from a common center) residing in an L_d phase background. B) A gel phase with amorphous domains residing in an L_d phase background. C) A gel phase with a mixture of amorphous and elliptical domains interspersed within an L_d phase background of positive curvature. D) Elliptical domains arranging their long axes approximately perpendicular to the perimeter of the circular region formed when the GUV adhered to the coverslip.

2.9A/C, can be seen arranged with their long axes approximately perpendicular to the perimeter of the contacted region.

B. MCR analysis of ESR spectra to locate phase boundaries on the binary axes

Confirmation of DPPC/DLPC phase boundaries (L_d + gel)

Initially, the MCR analysis was tested on spectra obtained along the DPPC/DLPC binary axis, for which the phase boundaries of the L_d + gel coexistence region are known (3, 36, 37). Figure 2.10A shows 19 experimental ESR spectra (solid line) along the DPPC/DLPC axis in 0.05 mole fraction increments. The pure DPPC spectra ($\xi_{DPPC} = 1$) was left out of the analysis because pure DPPC forms a chain-tilted gel phase (L_{β}') instead of the coexisting gel phase (L_{β}) (21, 37). Along with the experimental spectra (solid line), Figure 2.10A also shows the estimated spectra (dotted line, $\mathbf{S}^*$ in eq. 2.10) formed by the linear combination of the two eigenspectra obtained from the SVD of the data matrix, which consisted of the experimental spectra. As can be seen, the approximate spectra are nearly identical to the experimental spectra, which support the assumption that the experimental ESR spectra can be represented in the space of two spectral basis components (i.e. the two eigenspectra). The dual space to the space of eigenspectra consists of the coefficients of the linear combination of the eigenspectra, with two coefficients for each estimated spectrum. However, only the coefficients of the first eigenspectra are required to locate the phase boundaries because the two coefficients are dependent due to the normalization constraint on the absorbance vectors (i.e. experimental spectra). Figure 2.10B is the plot of the coefficients of the first eigenspectrum versus mole fraction DPPC. Determined by CFM, FRET, and equilibrium surface pressure, the L_d and gel phase boundaries along the DPPC/DLPC binary axis are between mole fraction DPPC = 0.235-0.32 and mole fraction DPPC = 0.785-0.85, respectively (3, 36, 38). The L_d and gel phase boundaries determined by MCR analysis of ESR spectra were mole

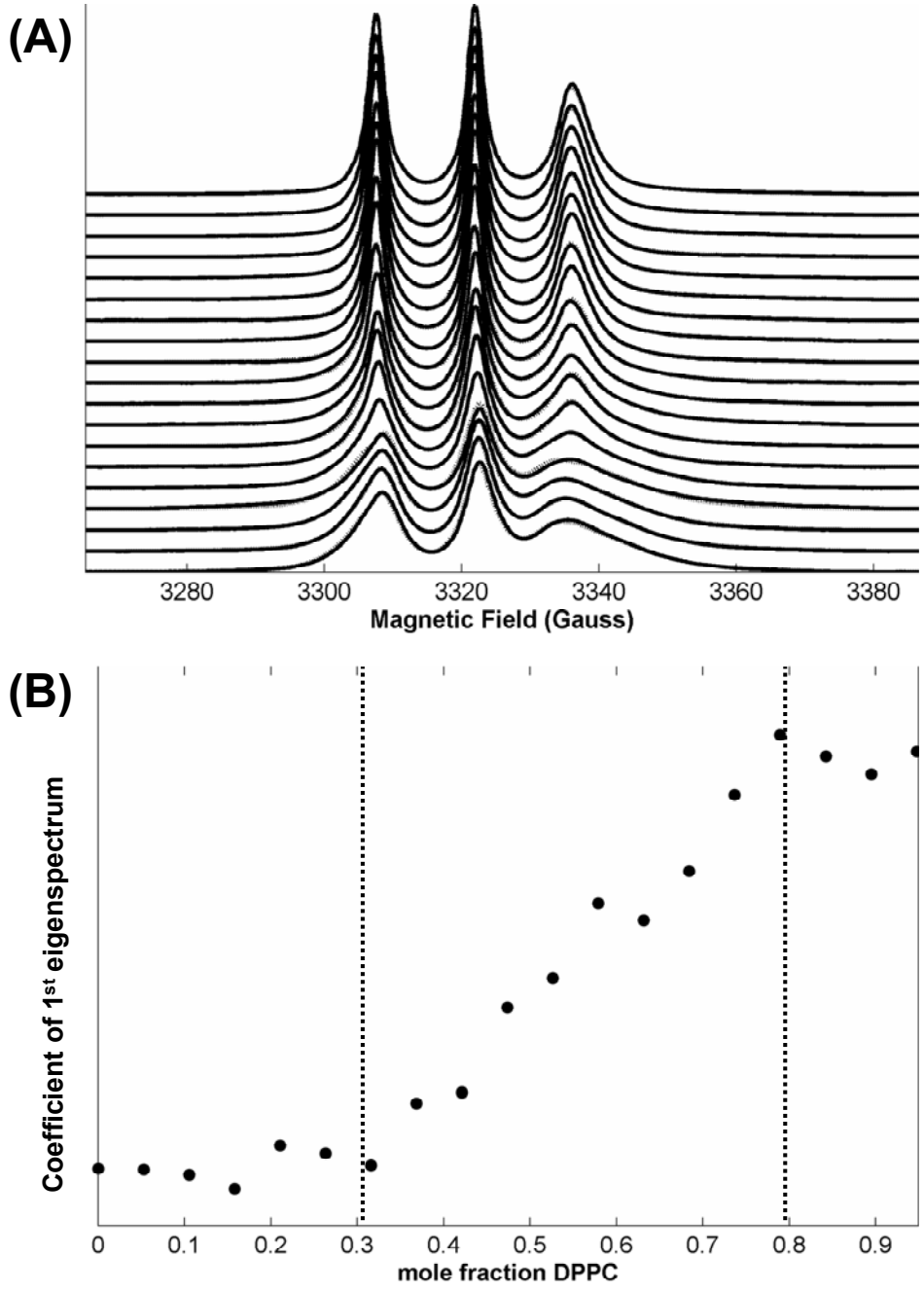

Figure 2.10: The MCR analysis of experimental ESR spectra along the DPPC/DLPC binary axis confirms the known phase boundaries for the L_d + gel coexistence region. A) The approximate spectra (dotted lines), which are the linear combination of the eigenspectra basis, reproduce almost exactly the experimental spectra (solid lines). B) A plot of the coefficients of the first eigenspectrum versus mole fraction of DPPC reveals the phase boundaries by visual inspection (vertical dotted lines).

fraction DPPC ≈ 0.30 and mole fraction DPPC ≈ 0.80, respectively. These boundaries can be seen visually in Figure 2.10B as the points where the coefficients increase from a relatively flat region of DLPC-rich L_d phases (mole fraction DPPC <≈ 0.30) to a relatively flat region of DPPC-rich phases (mole fraction DPPC >≈ 0.80).

Phase boundaries (L_d + gel) for the SPM/DOPC binary axis

Unlike the corresponding regions in other lipid systems (3-5), CFM showed no evidence of a microscopic L_d + gel phase coexistence region along the SPM/DOPC binary axis (Figure 2.2). Therefore, MCR analysis of ESR spectra was used to locate the phase boundaries for this presumed region. The same MCR analysis that was applied to the ESR spectra along the DPPC/DLPC binary axis was applied to ESR spectra along the SPM/DOPC binary axis. The results are displayed in Figure 2.11. The experimental (solid line) and approximate spectra (dotted line) in 0.05 mole fraction increments are plotted in Figure 2.11A and the coefficients of the first eigenspectrum are plotted in Figure 2.11B. Based on the visual inspection of the coefficient plot (Figure 2.11B), the L_d and gel phase boundaries were determined as mole fraction SPM ≈ 0.35 and mole fraction SPM ≈ 0.95, respectively. The outlier (sample 3 with mole fraction SPM = 0.1) in Figure 2.11B can easily be seen in Figure 2.11A as the mismatch between the experimental and approximate ESR spectra. In addition, the outlier spectrum was not visually similar to its neighboring spectra (samples 2 and 4), although all three spectra were from samples in the single L_d phase region.

Phase boundaries (L_o + gel) for the SPM/Chol binary axis

Similar to the corresponding regions in other lipid systems (3-5), CFM showed no evidence of a microscopic L_o + gel phase coexistence region along the SPM/Chol binary axis (Figure 2.2). Therefore, MCR analysis of ESR spectra was used to locate the phase boundaries for this presumed region. Figure 2.12 shows the results of the

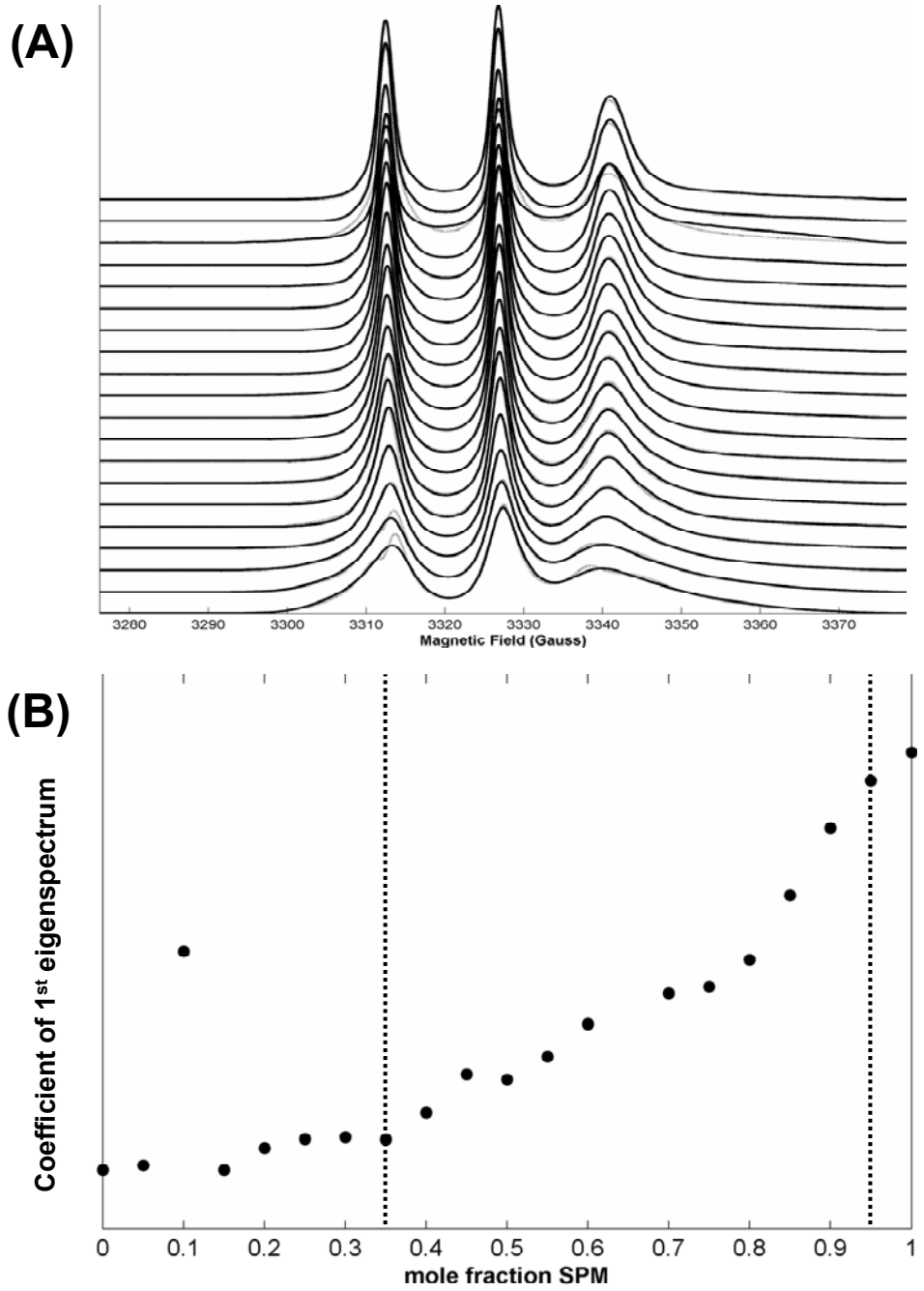

Figure 2.11: The MCR analysis of experimental ESR spectra along the SPM/DOPC binary axis determines the phase boundaries for the L_d + gel coexistence region. A) The approximate spectra (dotted lines) reproduce the experimental spectra (solid lines), except the outlier sample 3 (mole fraction SPM = 0.1). B) A plot of the coefficients of the first eigenspectrum versus mole fraction of SPM reveals the phase boundaries by visual inspection (vertical dotted lines).

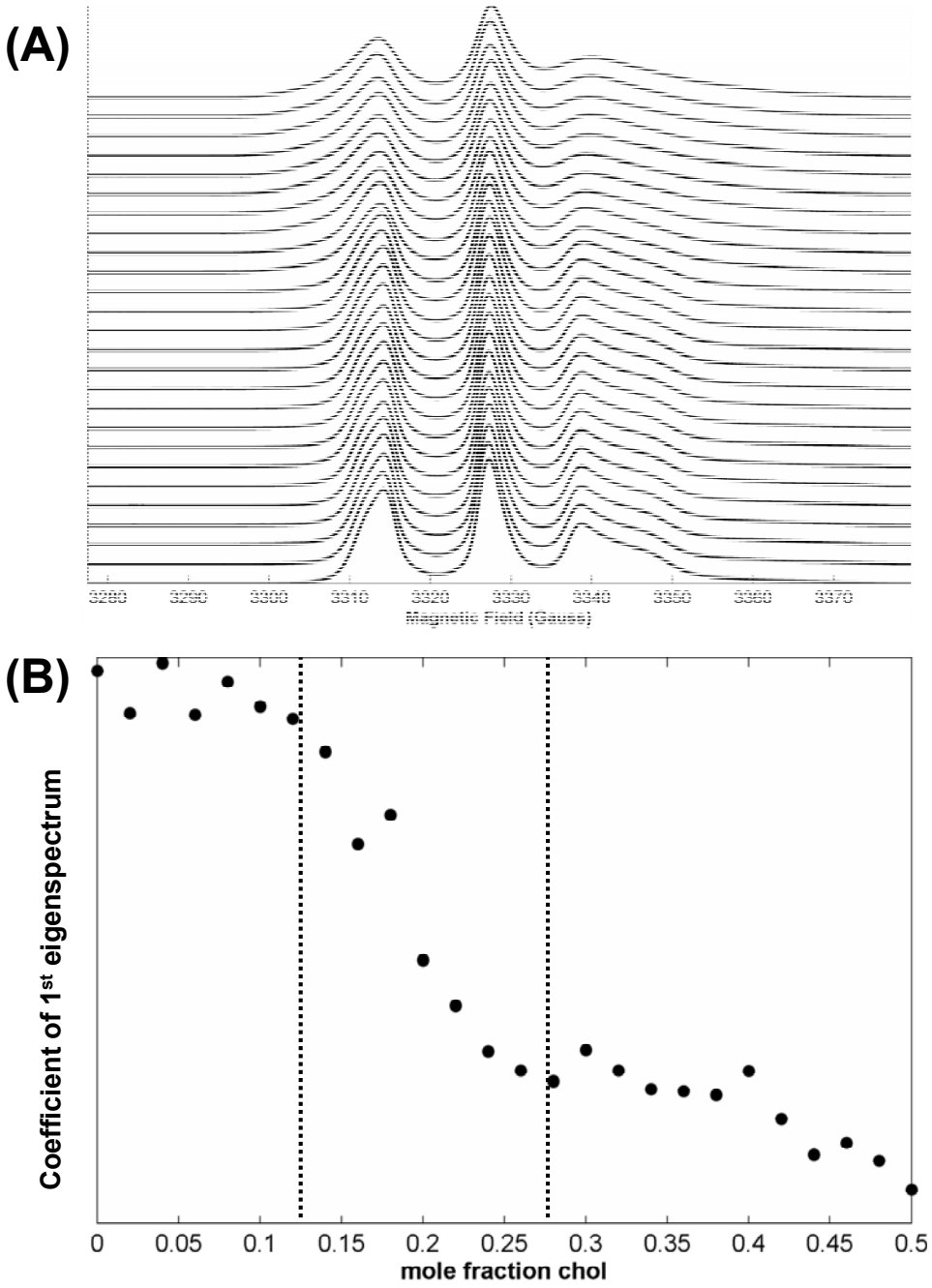

Figure 2.12: The MCR analysis of experimental ESR spectra along the SPM/Chol binary axis determines the phase boundaries for the L_o + gel coexistence region. A) The approximate spectra (dotted lines) reproduce the experimental spectra (solid lines). B) A plot of the coefficients of the first eigenspectrum versus mole fraction of cholesterol reveals the phase boundaries by visual inspection (vertical dotted lines).

MCR analysis on the ESR spectra along the SPM/Chol binary axis. The experimental (solid line) and approximate spectra (dotted line) in 0.02 mole fraction increments are plotted in Figure 2.12A and the coefficients of the first eigenspectrum are plotted in Figure 2.12B. Again, based on the visual inspection of the coefficient plot (Figure 2.12B), the gel and L_o phase boundaries were determined as mole fraction Chol ≈ 0.12 and mole fraction Chol ≈ 0.28, respectively. The coefficients begin to decrease from a relatively constant value after mole fraction Chol > 0.4, which indicates a deviation from the assumption that the coefficients are constant throughout an entire one-phase region. However, the decomposition to a two-component spectral basis still gave a good agreement between the approximate and experimental ESR spectra (Figure 2.12A).

IV. Discussion

The phase behavior of the SPM/DOPC/Chol lipid bilayer was investigated using the experimental methods of CFM and ESR. A compositional phase diagram of this model membrane mixture was determined with these methods, which have been successfully used previously to construct compositional phase diagrams of other lipid mixtures (3-6, 18-21). Because of their current applicability and limitations, CFM and ESR could not corroborate the phase boundaries determined by either method alone; therefore, this study stresses the importance of using multiple methods to construct phase diagrams. In addition, as also demonstrated in this work, CFM provides a useful tool in studying the mechanical phase behavior of GUVs. Percolation, size/shape, and the mechanical transitions of phase domains seem to be increasingly relevant to the structure and function of biological membranes (39, 40).

A. SPM/DOPC/Chol Compositional Phase Diagram at 23°C

We have constructed a nearly complete compositional phase diagram for the SPM/DOPC/Chol bilayer lipid mixture at 23°C (Figure 2.13). The phase diagram

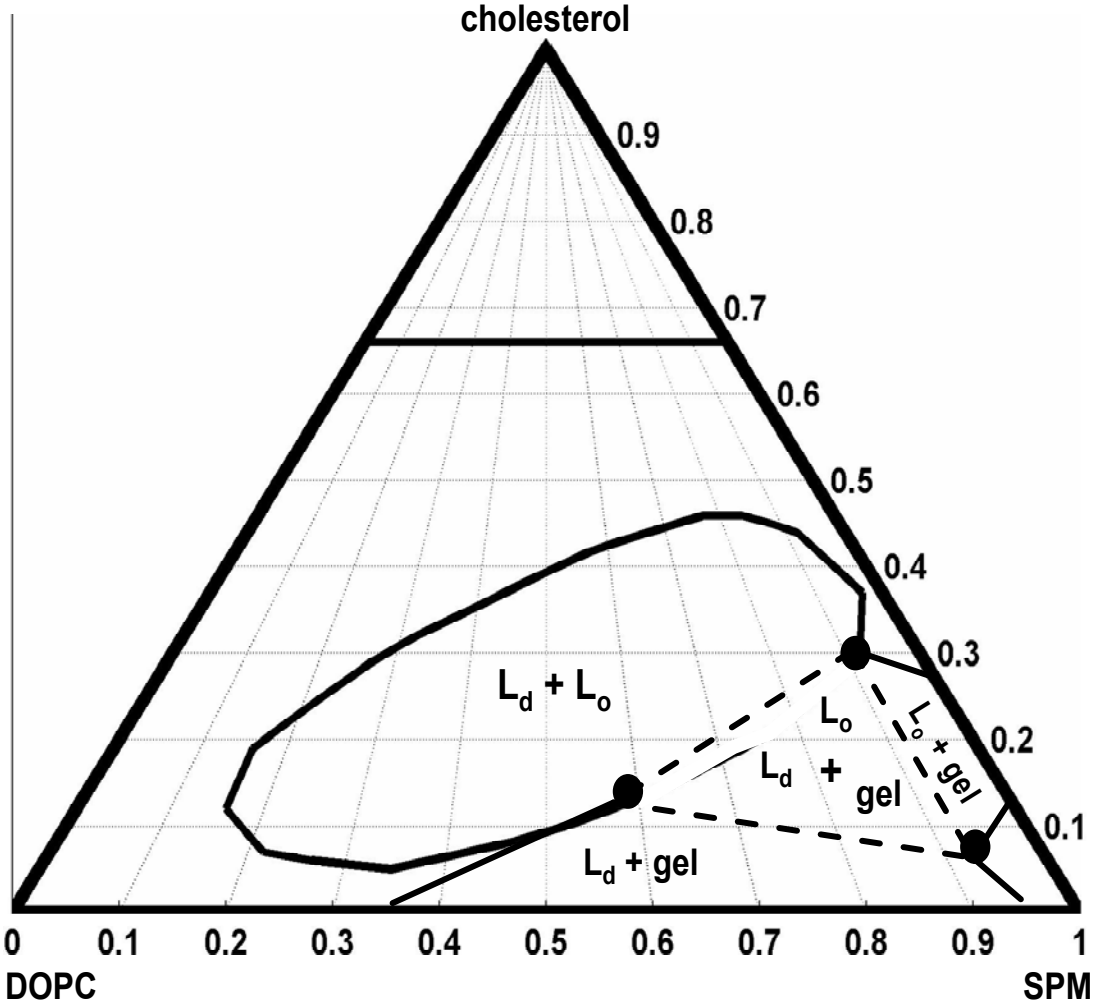

Figure 2.13: The SPM/DOPC/cholesterol phase diagram at 23°C contains three two-phase coexistence regions ($L_d + L_o$, L_d + gel, and L_o + gel) and single three-phase coexistence region ($L_d + L_o$ + gel triangle). The $L_d + L_o$ region was determined by CFM on GUV samples. The L_d + gel phase boundaries on the SPM/DOPC axis and the L_o + gel phase boundaries on the SPM/Chol axis were determined by MCR analysis of ESR spectra from MLV samples. The $L_d + L_o$ + gel coexistence triangle was not directly determined but inferred (see discussion).

consists of three two-phase coexistence regions ($L_d + L_o$, L_d + gel, and L_o + gel) and a three-phase coexistence triangle ($L_d + L_o$ + gel). Because previous studies on GUVs showed that coexisting L_d and L_o phases were microscopic (visible), CFM was used to delineate the elliptical coexistence curve of the $L_d + L_o$ coexistence region. In addition, because the coexisting phases in the L_d + gel and L_o + gel coexistence regions were nanoscopic (non-visible), MCR analysis of ESR spectra was used the determine the phase boundaries along the SPM/DOPC and SPM/Chol binary axes. Using known rules of phase diagram construction based on the phase rule and some simple physical assumptions, extensions of the L_d + gel and L_o + gel phase boundaries into ternary composition space and the approximate locations of the vertices of the three-phase coexistence triangle can be estimated (Figure 2.13). From the DOPC/SPM binary axis the L_d and gel phase boundaries for the L_d + gel coexistence region extend towards each other narrowing the coexistence region and decreasing the compositional difference between the coexisting phases. The physical assumption being that a small addition of cholesterol to coexisting L_d and gel phases increases the miscibility of the phase-separating phospholipids (3-5). However, from the SPM/Chol binary axis the L_o and gel phase boundaries for the L_o + gel coexistence region extend away from each other widening the coexistence region and increasing the compositional difference between the coexisting phases. In this case, the physical assumption implies that a small addition of DOPC to coexisting L_o and gel phases decreases the miscibility of SPM and cholesterol. This assumption seems counterintuitive because it suggests that SPM and cholesterol interact repulsively, which has not been found to be the case (1, 2, 5, 7, 14, 19, and 27). However, the idea posited suggests that both an increase (decrease) in the cholesterol (SPM) mole fractions of the L_o phase and a decrease (increase) in the cholesterol (SPM) mole fractions of the gel phase are needed to compensate for the perturbation in each phase

of the increase in DOPC mole fraction. In other words, SPM and cholesterol do not interact repulsively, but that the repulsions between DOPC and SPM/cholesterol are greater than the attraction between SPM and cholesterol. Furthermore, the integrity of the gel phase depends on the SPM concentration and the integrity of the L_o phase depends on the cholesterol concentration

Unfortunately, direct confirmation of the three-phase coexistence region by a CFM image of a GUV consisting of an L_d, L_o, and gel phases was not found. However, the three-phase coexistence region was inferred from CFM images of rare GUVs at compositions within the $L_d + L_o$ coexistence region but very near the presumed three-phase coexistence region that showed non-circular phase domains and fluorescence asymmetries. This evidence cannot be considered conclusive since non-circular domains can be the result of very low line tensions between coexisting L_d and L_o phases. Also, fluorescence asymmetries can be caused by multilamellar GUVs with uncoupled bilayers where domain fluorescence from a domain in one bilayer is attenuated by the other bilayer, although this scenario is highly unlikely as non-unilamellar vesicles are typically easy to spot and therefore avoided. Also, experimental artifacts may occur from the alternating excitations of the probes at a time scale similar to domain movements or fluctuations, although, again, this is highly unlikely because laser excitation of the probes is almost instantaneous. Positive identification of three phases was hampered by the difficulty in finding fluorescent probes that partition favorably into the gel phase or the L_o phase in SPM systems (34). Partitioning into the L_d phase was assumed for (16:0, Bodipy)-PC, but partitioning into the L_d phase was unexpected for C20:0-DiI. In fact, a wide variety of fluorescent membrane probes do not partition into a SPM-rich L_o phase, except for poly-aromatic hydrocarbon probes containing conjugated benzene-rings, such a perylene (34). Even without having direct proof from a CFM image, the existence of three two-phase

coexistence regions and ESR spectra at compositions within the presumed region showing multiple components (data not shown) strongly suggests that the three-phase coexistence region exists.

Currently, ESR spectral analysis cannot be applied to determine coexistence curves for three-component (ternary) two-phase regions (i.e. $L_d + L_o$); and, since CFM cannot be applied to nanoscopic coexisting phases, the two methods could not corroborate their determined phase boundaries. Therefore, both experimental procedures were necessary to solve the phase diagram. In the future, an extension of the MCR analysis of ESR spectra has the potential to determine the locations of the vertices of the three-phase coexistence triangle. A two-component two-phase region is topologically similar to a three-component three-phase region because the number of components equals the number of phases (at constant temperature and pressure); therefore, the compositions of the coexisting phases are invariant (i.e. thermodynamic degrees of freedom equals zero). The process of finding the phase boundary spectra for a three-phase coexistence triangle is almost the same as for the binary axes, where an orthonormal basis of rank three can be constructed by SVD on an appropriate spectral data matrix (30).

There are now many published complete or nearly complete phase diagrams of ternary lipid bilayer mixtures (3-6). Because of this growing amount of information there has been a need to categorize the phase behavior of all these lipid mixtures. One theme is to divide phase diagrams into two types based on whether or not the $L_d + L_o$ coexistence region has microscopic (visible) or nanoscopic (non-visible) coexisting phases (41). The size and shape of phase domains is no doubt an important phase behavior, especially regarding biological membranes; however, these phase properties are more appropriate for the mechanical equilibrium or non-equilibrium behavior of these mixtures, instead of the chemical equilibrium that the compositional phase

diagrams represent. Therefore, a better way of categorizing compositional phase diagrams is by the topology of the $L_d + L_o$ coexistence region. The $L_d + L_o$ coexistence region of the SPM/DOPC/Chol phase diagram (Figure 2.13) is a "half closed" region because of the miscibility critical point near the DOPC/Chol binary axis and the intersection with a three-phase coexistence triangle. A "closed" two-phase coexistence region would have two miscibility critical points. The SPM/POPC/Chol phase diagram (42) has an "open" $L_d + L_o$ coexistence region because this region intersects both the POPC/Chol binary axis and the three-phase coexistence triangle; therefore, it does not have a miscibility critical point. The "half closed" and "open" coexistence regions are topologically different. Not surprisingly, the SPM/DOPC/Chol phase diagram (Figure 2.13) is topologically identical to the DSPC/DOPC/Chol and DPPC/DOPC/Chol phase diagrams (4, 5, 13, and 43) because all three of these lipid systems have half closed $L_d + L_o$ coexistence regions. In addition, these phase diagrams have in common an L_d + gel, L_o + gel, and an $L_d + L_o$ + gel coexistence regions. However, interestingly, compositions within the L_d + gel coexistence regions of the DSPC/DOPC/Chol and DPPC/DOPC/Chol systems showed GUVs containing visible coexisting phases, but coexisting L_d and gel phases in the SPM/DOPC/Chol system are not visible. This difference is most likely attributed to the differences in chemical structure between sphingophospholipids (SPM) and glycerophospholipids (DSPC and DPPC) and its effect on the gel phase. Because the percolation threshold in some SPM binary systems lies close to the L_d phase boundary, the SPM gel phase may be highly reticular or branched at a size scale that cannot be microscopically visualized (35, 44). Also, coexisting L_o and gel phases from all three lipid mixtures are not visible, so an experimental determination of the percolation threshold may also indicate a reticular gel phase (45). However, for this coexistence region nanoscopic phases cannot be attributed to differences in chemical structure

between sphingolipids and glycerophospholipids, but probably to general interactions between phospholipids and cholesterol. Even for the visibly coexisting L_d and L_o phases in the SPM/DOPC/Chol system there were complications in determining the percolation threshold. For compositions near the L_d and L_o phase boundaries percolation was obvious, but within the middle of the coexistence region, the percolation threshold curve could not be delineated because which phase was continuous could not be determined (Figure 2.3). The most likely reason was that the GUVs were in the still in the process of achieving mechanical equilibrium (i.e. domain coarsening, shape modification) and that neither phase had an obviously dominant area fraction. Moreover, percolation and light-induced phase separation into microscopic phases, possibly artifactual (see below), complicates a rigorous and unambiguous categorization of lipid phase behavior based on the size and shape of phase domains, especially when these properties are still poorly understood.

Contrary to supported bilayers and MLVs, freely floating GUVs provide the best model to study the mechanical phase behavior of model membranes because mechanical transformations, such as bilayer bending to adopt an energy minimizing curvature, can be directly observed. However, the problem with this model system is the uncontrolled compositional/thermal history and poor equilibration with respect to the osmotic pressure differential during GUV formation that leads to variability in the mechanical states of the GUVs within a sample. In both of the two main GUV sample preparations (26, 46), the process of going from a lipid solution to an aqueous suspension of GUVs involves a dehydrated/desolvated lipid film, similar to stacked bilayers, that can possibly allow for the demixing of the lipid components and result in GUVs of variable composition. Also, and probably most importantly, after the incubation of the GUV suspension above the gel/L_d transition temperature of the highest melting phospholipid, the sample should be annealed to avoid meta-stable

states and to allow proper equilibration instead of cooling uncontrollably (as was the case unfortunately in this study). Thermal annealing is especially critical for mechanically stressed bilayers such as GUVs. Furthermore, during GUV formation smaller vesicles fuse into larger vesicles to increase volume and minimize the osmotic pressure differential and its contribution to surface tension (47). Therefore, most GUVs are nearly spherical having the smallest surface area to volume ratio. However, poor equilibration from rapid cooling and slow movement of water across the bilayer can lead to GUVs having excess surface area, which is more surface area than a sphere of equal volume. This variability in surface tension and excess surface area of the GUVs can influence the shape, size, and curvature that phase domains can adopt (8, 9, and 48), independent of other variables dependent on composition, such as elastic moduli, spontaneous curvature, domain area fraction, and line tension. Furthermore, the mechanical state of the GUV can influence the equilibrium compositions reached during phase separation (49). The applicability of the GUV model system to biological membranes relies on the existence of a pressure differential across the membranes of the cell, which, under certain physiological conditions, most likely exists.

B. Mechanical Equilibrium of Coexisting Fluid Phase Domains

Because of sample history, GUVs are most likely not in mechanical equilibrium when observed under the microscope. However, equilibration proceeds the fastest within the plane of the bilayer because the translational diffusion of the lipids is much faster than diffusion normal to or across the bilayer. Minimization of the interfacial line energy for a constant line tension and fixed area results in a circular domain, which is the shape that has the lowest perimeter to area ratio. Initially, a domain adopts a circular shape as a local energy minimum within the plane of the bilayer; however, the global energy minimum of the entire GUV involves not only the

shape of individual domains but the interactions between domains, bilayer curvature, surface tension, excess surface area required for bending, and total line energy. Occasionally these competing energetic contributions result in a global mechanical equilibrium of the GUV that shows long-range order.

A wide range of diverse systems consisting of coexisting phases exhibit long-range domain ordering or patterning, called superstructure phases or modulated phases (50, 51). The formation of superstructure phases involves the competition, sometimes called "frustration", of opposing attractive and repulsive forces of varying origin in attaining the mechanical equilibrium of coexisting phases, resulting in a periodic modulation of an internal order parameter (51, 52). Two two-dimensional superstructure phases, the "bubble" phase, which is hexagonally arranged circular phase domains within a continuous background of another phase, and the "stripe" phase, which is thin locally-parallel domains of alternating phases, have been characterized (50, 51). In lipid systems, the bubble and stripe phases have been observed in lipid monolayers at the air-water interface (53, 54) and lipid bilayers (7, 8, Figure 2.4A/B/D in this work). These superstructure phases for lipid monolayers were determined to be modulated by the line tension and the electrostatic dipole density difference between the coexisting phases (55-57). In minimizing the free energy the positive line tension favors domain fusion and/or large phase domains with compacted, circular shapes (i.e. bubbles), whereas the electrostatic dipolar repulsion favors dispersed small domains (nanodomains) and/or domains with extended, elongated shapes (i.e. thin stripes). Interestingly, from a theoretical analysis, domain shape is not controlled by the line tension and dipolar density difference independently, but the relevant parameter is their ratio (57). The bubble and stripe phases were theoretically predicted to coexist in lipid monolayers (54, 57), but this has not observed experimentally.

In lipid bilayers, which can be thought of as two coupled monolayers supporting each other, the electrostatic dipole density difference between coexisting phases still exists, but the magnitude and influence of this physical property to the free energy is presumed to be much less for bilayers because of the strong shielding by water on both sides of the bilayer (58). However, the energy of elastic deformations, such as bending and compression/expansion, and the line energy between coexisting phases are more important to bilayer stability. Consequently, the relationship between phase separation, curvature, and line tension both theoretically (49, 59-62) and experimentally (7-9, 13, 63) has been studied. The bubble phase observed in bilayers (7, 8, Figure 2.4A/B/C in this work) was proven to be modulated by not only the line tension and bending energy, but also required both a surface tension and elastic compressibility/expansion energy contribution (8). Also, a critical domain size was predicted, and observed (8, Figure 2.4A/B), for the partially budded state, which corresponds to an energy minimum between the flat and fully budded states. This domain size reflects the balance between the line tension trying to minimize the domain boundary and the domain bending energy resisting an overly-bent fully budded state (8, 64). In addition, the stripe phase was found to be stable for low line tensions and high surface tensions, and it could coexist with the bubble phase (64). Repulsion between phase domains has been theoretically predicted from the elastic deformations of splay and tilt that occur at the interface between coexisting phases (65), and we have observed, as well as others, phase domain repulsion at certain compositions (8, 9, 13). Interestingly, similar to the energetic parameter controlling domain shape in monolayers, the relative parameter from a theoretical analysis that controls domain shape in bilayers seems to be the ratio of the bending modulus (a thermodynamic variable specifying the energy required to bend the bilayer) to line tension, called the persistence, invagination, or characteristic length (8, 60, 64).

Furthermore, the coexistence of bubble and stripe phases may have been observed for bilayers in the SPM/DOPC/Chol system (Figure 2.4D). However, the possibility still exists that this bubble + stripe coexisting state has not achieved mechanical equilibrium.

C. Mechanical and Chemical Non-Equilibrium of Coexisting Fluid Phase Domains

Evidence of non-equilibrium phenomena was observed at all compositions within the $L_d + L_o$ coexistence region. These phenomena seem to be divided into three types: 1) circular domain growth/coarsening of chemically distinct phases, 2) light-induced transitions from chemically distinct L_d stripe domains to circular domains, 3) light-induced phase separation from a homogenous phase into mechanically and chemically distinct coexisting phases. In phenomenon one and two, chemical equilibrium, manifested as coexisting phases, was already established when observed under the microscope, but the phases were still in the process reaching mechanical equilibrium. Chemical equilibration between fluid phases within the plane of the bilayer is expected to be fast because of the rapid translational diffusion. In phenomenon three, relaxation to chemical and mechanical equilibrium occurred simultaneously and only occurred near the coexistence curve.

GUVs at most of the compositions within the coexistence region exhibited the coarsening of circular phase domains, with the predominant method being domain fusion. Domain fusion is the most efficient method of matter transport (66) and was also observed to be the predominant method of domain coarsening in the DPPC/DOPC/Chol system (13). When they reach a critical size and if there is excess surface area the phase domains will bulge from the bilayer causing a repulsion between domains that will delay further domain fusion (8, 9). The establishment of mechanical equilibrium results in either domains ceasing to fuse because of the

interdomain repulsion and arranging symmetrically within the bilayer or complete fusion into fully separated phases that will either partially bud from each other (Figure 2.4C) or separate into two vesicles. The exact outcome will depend on the composition and magnitudes of the elastic moduli, line tension, surface tension, area fractions, and excess surface area (8, 9, 64).

At a unique composition near the three-phase coexistence region, light-induced transitions of L_d stripe domains into circular domains was observed (Figure 2.6). These shape transitions are probably light-induced because they occurred immediately after observation and transpired very fast. Also, the transitions seem to be driven by the minimization of the line energy. Interestingly, at approximately the same composition within the DPPC/DOPC/Chol system, shape transitions from circular L_d domains to stripe domains (called viscous fingering) were observed as temperature is raised through the miscibility temperature (13). It is possible that in the SPM/DOPC/Chol system the stripe domains were kinetically trapped during the uncontrolled cooling of the GUV sample, and the photo-oxidation of the fluorescent probes and unsaturated lipids caused the collapse of the stripe domains into circular domains by increasing the line tension (see below).

The light-induced phase separation observed at compositions near the $L_d + L_o$ coexistence curve in the SPM/DOPC/Chol system (Figure 2.7/8) has been studied in detail in other lipid systems (32, 33). Although the exact mechanism is unclear, lipid peroxides and hydroxylated lipids, caused when the excitation of the fluorescent probes promotes a cascade of free-radical chemical reactions, induce phase separation. The oxidized lipids both increase the area fraction and line tension of intrinsically microscopic coexisting phases or cause nanoscopic coexisting phases to become microscopic (32), presumably by also increasing the line tension. The light-induced phase shape transitions observed in the SPM/DOPC/Chol system (Figure 2.6, Figure

2.7I-L, Figure 2.8F) can be explained by oxidized lipids increasing the line tension. Also, as in the SPM/DOPC/Chol system (Figure 2.2), light-induced phase separation was also observed to occur near phase boundaries in other lipid systems (33). The lipid peroxides are thought to cause lipid clusters formed in highly non-ideal lipid mixtures to coalesce (33).

In general, phase separation proceeds by two mechanisms: nucleation or spinodal decomposition (66-69). Both processes occur at compositions within the coexistence region; however, nucleation occurs near the coexistence curve within the meta-stable region (i.e. globally unstable, locally stable) and spinodal decomposition occurs farther from the coexistence curve between the spinodals (i.e. globally and locally unstable). Dynamically, nucleation is when, from an initially homogeneously mixed but meta-stable bilayer, small domains of one phase at the coexisting composition separate from the other phase at randomly located but discrete points throughout the system and grow in size by accretion from diffusing constituents, Ostwald ripening, and domain fusion. On the other hand, spinodal decomposition is when, from an initially homogeneously mixed but unstable bilayer, one phase separates from the other phase spatially throughout the system with continuously changing and differentiating compositions by diffusion until the coexisting compositions are obtained. In other words, nucleation is a phase separation that is large in degree (composition change) but small in extent (size); whereas spinodal decomposition is small in degree but large in extent (67).

Describing the light-induced phase separation as an artifact depends on the initial state of the bilayer. An artifact is something that was created that would not normally be present. Homogeneous fluorescence could mean either that the bilayer consists of nanoscopic phases, the bilayer is mixed but meta-stable, or the bilayer is mixed but stable. If the oxidized lipids increase the line tension between nanoscopic

phases causing the phases to grow in size to minimize the line energy, then the light-induced phase separation into microscopic phases is an artifact regarding phase size (32, 33). If the bilayer was mixed but stable and lipid oxidation destabilizes the mixture and promotes phase separation either by introducing lipid repulsion and/or simply changing the composition, then the light-induced phase separation is an artifact regarding phase coexistence. However, if the bilayer was mixed but meta-stable where the equilibrium state is coexisting phases but the system is kinetically trapped and lipid oxidation provides the stimulus to phase separate, then the light-induced phase separation is not really an artifact because any perturbation could potentially cause phase separation. This situation is useful in constructing compositional phase diagrams because meta-stable states are near the coexistence curve but still within the coexistence region (Figure 2.2); therefore, identifying these compositions results in a more accurate location of the coexistence curve instead of designating them as outside the coexistence region. However, determining whether a homogeneous GUV is meta-stable or stable is difficult, and a mechanical perturbation instead of a chemical perturbation would be a better way to induce phase separation in constructing compositional phase diagrams.

The mechanism of phase separation in the SPM/DOPC/Chol system depends on composition. Because of the initial appearance of many small domains (Figure 2.7) and the fact that the phase separation occurs near the coexistence curve suggesting meta-stable states, nucleation of L_o phase domains around aggregates of the oxidized lipids is the most likely explanation of the light-induced phase separation. However, for some compositions near the three-phase region (Figure 2.8A-C) the light-induced phase separation was probably an artifact regarding either phase coexistence or phase size. Furthermore, it should be noted that for most of the compositions within the L_d + L_o coexistence region microscopic phase separation was not induced by light because

they were already present when first observed. Spinodal decomposition was most likely the dominate mechanism of phase separation for these compositions, but was not observed because it occurred while the GUV samples were cooling. Spinodal decomposition may have been observed in the SPM/DOPC/Chol system (Figure 2.8D/E) and was observed in the DPPC/DOPC/Chol system (13). In addition, a combination of uncontrolled cooling/GUV stress, spinodal decomposition, and heterogeneous SPM (Figure 2.1) could have resulted in the rare phase shapes (Figure 2.4D-F, Figure 2.6, Figure 2.7I-L, and Figure 2.8F).

D. Domain Shapes of a SPM-rich Gel Phase

Contrary to fluid phases, the gel (or solid) phases exhibit a larger variety of domain shapes (10-12). The phase morphology of gel domains in lipid bilayers depends strongly on composition, mechanical properties, thermal history, and equilibration time (10, 11). The composition of the bilayer determines the degree of immiscibility and lipid packing, especially the ordering of molecular tilt or orientation. The degree of non-ideal mixing can control domain shapes, where gel phases of lower immiscibility form more reticular or fractal shapes and higher immiscibility form more compact shapes (70). Also, the lipid packing of phosphatidylcholines, such as DPPC, and sphingomyelin, which has the same chemical headgroup, can cause these molecules to orient in particular directions, forming the tilted gel phases, $P_{\beta'}$ and $L_{\beta'}$ (71, 72). The tilted nature of these gel phases can lead to anisotropic line tensions, which can also influence domain shape (73, 74). Although both these phases are tilted, the $P_{\beta'}$ phase, called the "ripple" phase, has a characteristic periodic height difference resembling a wave, whereas the $L_{\beta'}$ phase is flat. Therefore, the surface tension of the GUV can influence the formation of the tilted gel phases, where the $P_{\beta'}$ phase forms at low surface tensions and the $L_{\beta'}$ phase forms at high surface tensions (75). Finally, because of the slow translational and rotational diffusion of lipids within

gel phases, domain shape is sensitive to the dynamics of phase separation, particularly nucleation (76), which occurs uncontrollably during rapid cooling (i.e. supercooling).

The dark domains observed within the L_d + gel coexistence region of the SPM/DOPC/Chol system were probably the $P_{\beta'}$ phase. Brain sphingomyelin can exist in the $P_{\beta'}$ phase (71). Some GUVs had a folded appearance (Figure 2.9C) suggesting that these vesicles had a low surface tension conducive to $P_{\beta'}$ formation (75). The gel domains were only observed after the GUV sample remained on the microscope slide for over 24 hours, suggesting that a loss of water possibly caused a decrease in the surface tension for a fraction of the GUVs, which already had a natural variability in surface tension because of slow equilibration of osmosis and rapid cooling after formation. Also, our GUV samples contained 10% DOPG, a negatively charged lipid that when added to a bilayer introduces a repulsion which reduces surface tension (77). The addition of 10% DOPG to DPPC/DOPC GUVs promoted the formation of the $P_{\beta'}$ phase (77). Finally, the $P_{\beta'}$ phase excludes many fluorescent probes (78). The three-fold symmetric arrangement of elliptical gel phase domains (Figure 2.9A) has not been seen in bilayers before. These tri-domain structures may have two possible paths of formation, either 1) the elliptical gel phase domains diffuse independently, where an anisotropic line tension caused the tips to attract each other and the sides to repulse each other, or 2) the elliptical gel phase domains grow out of a common nucleated center. Evidence for the first formation is that even in the same GUV the three-fold symmetric arrangement is not strictly obeyed, where some elliptical domains seem to be clustered or the tips of just two domains are in contact. Also, other GUVs (Figure 2.9D) seem to have independent elliptical domains where again the tips play an organizing role by contacting the adhesion line of the GUV to the glass coverslip. For solid domains in lipid monolayers, elliptical domains were theoretically found to be more stable than circular domains when gel domains reached

and surpassed a certain size (79). However, evidence for the second formation can also be found in monolayer studies, where a similar tri-domain structure of a solid phase was observed (54, 80). Also, the lipids in this monolayer phase were found to be tilted (80).

REFERENCES

1. Feigenson, G. W. *Biochim. Biophys. Acta* **2008**, 1788, 47.
2. Van Meer, G.; Voelker, D. R.; Feigenson, G. W. *Nat. Rev. Mol. Cell Bio.* **2008**, 9, 112.
3. Feigenson, G. W.; Buboltz, J. T. *Biophys. J.* **2001**, 80, 2775.
4. Zhao, J.; Wu, J.; Heberle, F. A.; Mills, T. T.; Klawitter, P.; Huang, G.; Costanza, G.; Feigenson, G.W. *Biochim. Biophys. Acta* **2007**, 1768, 2764.
5. Veatch, S. L.; Keller S. L. *Biochim. Biophys. Acta* **2005**, 1746, 172.
6. Veatch, S. L.; Gawrisch, K.; Keller, S. L. *Biophys. J.* **2006**, 90, 4428.
7. Baumgart, T.; Hess, S. T.; Webb, W. W. *Nature* **2003**, 425, 821.
8. Semrau, S.; Idema, T.; Schmidt, T.; Storm, C. *Biophys. J.* **2009**, 96, 4906.
9. Yanagisawa, M.; Imai, M.; Masui, T.; Komura, S.; Ohta, T. *Biophys. J.* **2007**, 92, 115.
10. Wesolowska, O.; Michalak, K.; Maniewska, J.; Hendrich, A. B. *Acta Biochim. Pol.* **2009**, 56, 33.
11. Gordon, V. D.; Beales, P. A.; Zhao, Z.; Blake, C.; MacKintosh, F. C.; Olmsted, P. D.; Cates, M. E.; Egelhaaf, S. U.; Poon, W. C. K. *J. Phys.: Condensed Matter* **2006**, 18, L415.
12. Bagatolli, L. A.; Gratton, E. *Biophys. J.* **2000**, 79, 434.
13. Veatch, S. L.; Keller, S. L. *Biophys. J.* **2003**, 85, 3074.
14. Samsonov, A. V.; Mihalyov, I.; Cohen, F. S. *Biophys. J.* **2001**, 81, 1486.
15. Marsh, D. *Biophys. J.* **2007**, 93, 3884.
16. Evans, E. A. *Biophys. J.* **1974**, 14, 923.
17. Evans, E. A.; Waugh, R. *J. Colloid Interf. Sci.* **1977**, 60, 286.
18. Recktenwald, D. J.; McConnell, H. M. *Biochemistry* **1981**, 20, 4505.
19. Sankaram, M. B.; Thompson, T. E. *Biochemistry* **1990**, 29, 10670.

20. Collado, M. I.; Goni F. M.; Alonso, A.; Marsh, D. *Biochemistry* **2005**, 44, 4911.

21. Chiang, Y. W.; Costa-Filho, A. J.; Freed, J. H. *J. Phys. Chem B* **2007**, 111, 11260.

22. Vist, M. R.; Davis, J. H. *Biochemistry* **1990**, 29, 451.

23. Thewalt, J. L.; Bloom, M. *Biophys. J.* **1992**, 63, 1176.

24. Hsueh, Y. W.; Gilbert, K.; Trandum, C.; Zuckermann, M.; Thewalt, J. *Biophys. J.* **2005**, 88, 1799.

25. Dietrich, C.; Bagatolli, L. A.; Volovyk, Z. N.; Thompson, N. L.; Levi, M.; Jacobson, K.; Gratton, E. *Biophys. J.* **2001**, 80, 1417.

26 Akashi, K.; Miyata, H.; Itoh, H.; Kinosita, K. Jr. *Biophys. J.* **1996**, 71, 3242.

27. Bagatolli, L. A. *Biochim. Biophys. Acta* **2006**, 1758, 1541.

28. Buboltz, J. T.; Feigenson, G. W. *Biochim. Biophys. Acta* **1999**, 1417, 232.

29. Jiang, J.; Liang, Y.; Ozaki, Y. *Chemometr. Intell. Lab.* **2004**, 71, 1.

30. Markovsky, I.; Van Huffel, S. *Signal Process* **2007**, 87, 2283.

31. Wentzell, P. D.; Karakach, T. K.; Roy, S.; Martinez, J. M.; Allen, C. P.; Werner-Washburne, M. *BMC Bioinformatics* **2006**, 7, 343.

32. Ayuyan, A. G.; Cohen, F. S. *Biophys. J.* **2006**, 91, 2172.

33. Zhao, J.; Wu, J.; Shao, H.; Kong, F.; Jain, N.; Hunt, G.; Feigenson, G. W. *Biochim. Biophys. Acta* **2007**, 1768, 2777.

34. Baumgart, T.; Hunt, G.; Farkas, E. R.; Webb, W. W.; Feigenson, G. W. *Biochim. Biophys. Acta* **2007**, 1768, 2182.

35. Vaz, W. L. C.; Almeida P. F. F. *Curr. Opin. Struct. Bio.* **1993**, 3, 482.

36. Buboltz, J. T. *Phys. Rev. E* **2007**, 76, 021903.

37. Chiang, Y. W.; Shimoyama, Y.; Feigenson, G. W.; Freed J. H. *Biophys. J.* **2004**, 87, 2483.

38. Buboltz, J. T.; Feigenson, G. W. *Langmuir* **2000**, 16, 3606.

39. Janmey, P. A.; Kinnunen, P. K. J. *Trends Cell Biol.* **2006**, 16, 538.

40. McMahon, H. T.; Gallop, J. L. *Nature* **2005**, 438, 590.

41. Feigenson, G. W. *Annu. Rev. Biophys. Biomol. Struct.* **2007**, 36, 63.

42. de Almeida, R. F. M.; Fedorov, A.; Prieto, M. *Biophys. J.* **2003**, 85, 2406.

43. Veatch, S. L.; Soubias, O.; Keller, S. L.; Gawrisch, K. *P. N. A. S.* **2007**, 104, 17650.

44. Bar, L. K.; Barenholz, Y.; Thompson, T. E. *Biochemistry* **1997**, 36, 2507.

45. Almeida, P. F. F.; Vaz, W. L. C.; Thompson, T. E. *Biophys. J.* **1993**, 64, 399.

46. Angelova, M. I.; Soleau, S.; Meleard, Ph.; Faucon, J. F.; Bothorel, P. *Progr. Colloid Polym. Sci.* **1992**, 89, 127.

47. Mathivet, L.; Cribier, S.; Devaux, P. F. *Biophys. J.* **1996**, 70, 1112.

48. Baumgart, T.; Das, S.; Webb, W. W.; Jenkins, J. T. *Biophys. J.* **2005**, 89, 1067.

49. Seifert, U. *Phys. Rev. Lett.* **1993**, 70, 1335.

50. Seul, M.; Andelman, D. *Science* **1995**, 267, 476.

51. Andelman, D.; Rosensweig, R. E. *J. Phys. Chem. B* **2009**, 113, 3785.

52. Groves, J. T. *Annu. Rev. Phys. Chem.* **2007**, 58, 697.

53. McConnell, H. M.; Tamm, L. K.; Weis, R. M. *Proc. Natl. Acad. Sci.* **1984**, 81, 3249.

54. McConnell, H. M. *Annu. Rev. Phys. Chem.* **1991**, 42, 171.

55. Keller, D. J.; McConnell, H. M.; Moy, V. T. *J. Phys. Chem.* **1986**, 90, 2311.

56. Andelman, D.; Brochard, F.; Joanny, J-F. *J. Chem. Phys.* **1987**, 86, 3673.

57. McConnell, H. M. *Proc. Natl. Acad. Sci.* **1989**, 86, 3452.

58. Liu, J.; Qi, S.; Groves, J. T.; Chakraborty, A. K. *J. Phys. Chem. B* **2005**, 109, 19960.

59. Andelman, D.; Kawakatsu, T.; Kawasaki, K. *Europhys. Lett.* **1992**, 19, 57.

60. Julicker, F.; Lipowsky, R. *Phys. Rev. E* **1996**, 53, 2670.

61. Taniguchi, T. *Phys. Rev. Lett.* **1996**, 76, 4444.

62. Jiang, Y.; Lookman, T.; Saxena, A. *Phys. Rev. E* **2000**, 61, R57.

63. Sackmann, E.; Feder, T. *Mol. Membr. Biol.* **1995**, 12, 21.

64. Harden, J. L.; MacKintosh, F. C.; Olmsted, P. D. *Phys. Rev. E* **2005**, 72, 011903.

65. Kuzmin, P. I.; Akimov, S. A.; Chizmadzhev, Y. A.; Zimmerberg, J.; Cohen, F. S. *Biophys. J.* **2005**, 88, 1120.

66. Frolov, V. A. J.; Chizmadzhev, Y. A.; Cohen, F. S.; Zimmerberg, J. *Biophys. J.* **2006**, 91, 189.

67. Cahn, J. W.; Hilliard, J. E. *J. Chem. Phys.* **1959**, 31, 688.

68. Koch, S. W.; Desai, R. C.; Abraham, F. F. *Phys. Rev. A* **1983**, 27, 2152.

69. Schmelzer, J. W. P.; Abyzov, A. S.; Moller, J. *J. Chem. Phys.* **2004**, 121, 6900.

70. Schram, V.; Lin, H-N.; Thompson, T. E. *Biophys. J.* **1996**, 71, 1811.

71. Meyer, H. W.; Bunjes, H.; Ulrich, A. S. *Chem. Phys. Lipids* **1999**, 99, 111.

72. Katsaras, J.; Tristram-Nagle, S.; Liu, Y.; Headrick, R. L.; Fontes, E.; Mason, P. C.; Nagle, J. F. *Phys. Rev. E* **2000**, 61, 5668.

73. Leidy, C.; Kaasgaard, T.; Crowe, J. H.; Mouritsen, O. G.; Jorgensen, K. *Biophys. J.* **2002**, 83, 2625.

74. Kaasgaard, T.; Leidy, C.; Crowe, J. H.; Mouritsen, O. G., Jorgensen, K. *Biophys. J.* **2003**, 85, 350.

75. Needham, D.; Evans, E. *Biochemistry* **1988**, 27, 8261.

76. Bernchou, U.; Ipsen, J. H.; Simonsen, A. C. *J. Phys. Chem. B* **2009**, 113, 7170.

77. Li, L.; Cheng, J-X. *Biochemistry* **2006**, 45, 11819.

78. Mesquita, R. M. R. S.; Melo, E.; Thompson, T. E.; Vaz, W. L. C. *Biophys. J.* **2000**, 78, 3019.

79. Keller, D. J.; Korb, J. P.; McConnell, H. M. *J. Phys. Chem.* **1987**, 91, 6417.

80. Moy, V. T.; Keller, D. J.; McConnell, H. M. *J. Phys. Chem.* **1988**, 92, 5233.

***Chapter Three: The Determination of Tie-Line Fields For Coexisting Lipid Phases: An ESR Study**

A novel method we refer to as the tie-line field (TLF) method has been developed to globally determine the tie-lines of any three-component two-phase coexistence region by fitting electron-spin resonance (ESR) spectra obtained from compositions on the coexistence curve and within the coexistence region. The TLF method is illustrated by applying it to the liquid-ordered (L_o) and liquid-disordered (L_d) phase coexistence region of the lipid system brain-sphingomyelin/dioleoylphosphatidylcholine/cholesterol (SPM/DOPC/Chol), for which an estimate of a tie-line was previously obtained by an earlier method also using ESR spectra. The essential aspect of the TLF method is the unique parameterization of the coexistence region called a "ruled surface". The use of the ruled surface enables one to guarantee that tie-lines do not cross, as required by the phase rule, whereas previous methods lack this important constraint. It also makes simultaneous use of the full data set in determining the TLF and leads to a more efficient experimental design than previously used. The method is first tested out on synthetic data sets, then least-squares fitting of the ESR spectra with the parameterized model results in a tie-line field consistent with other known information on this lipid system. The best-fit tie-line field consists of the set of tie lines which are not exactly parallel; they exhibit a gradual change in slope with the largest slope within the coexistence region connecting the coexistence curve compositions with the highest and lowest cholesterol concentrations. The results are compared with those from more constrained methods of representing the tie-line fields as well as with the previous tie-line determination for the SPM/DOPC/Chol system. An accurate determination of the tie-line field of phase

coexistence regions in lipid systems is a necessary step in determining coexisting lipid compositions to serve as models of cell plasma membranes.

I. Introduction

In this Chapter we introduce a new method for determining tie-lines in two-phase regions of multi-component model membrane systems which directly provides the whole set of tie-lines, properly called the tie-line field. This work grew out of our previous work on the development of a simple methodology for using ESR spectra for this purpose (1, 2) which was recently applied to the two-phase liquid-ordered (L_o) + liquid-disordered (L_d) coexistence region of the three component SPM/DOPC/cholesterol (SPM = brain sphingomyelin, DOPC = dioleoylphosphatidylcholine) lipid system (2, 3). The limitations of that method, which independently seeks out each individual tie-line from a set of trial tie-lines, became clear and motivated us to find a more global approach using ESR spectra that removes the weaknesses of the earlier approach. These weaknesses include inefficient use of the experimental data, difficulty in constraining the individual tie-lines from intersecting, and overcoming uncertainties in some details of relevant features of the phase diagram. After developing this method herein, we illustrate its use for the two-phase $L_o + L_d$ coexistence region of SPM/DOPC/chol, which then enables us to: i) compare with results obtained with the earlier method (2) and to ii) draw new conclusions about the tie-line field for this system.

In sub-section A of this Introduction we provide a review of the relevant background, and in sub-section B we introduce key aspects of the new methodology.

A. Lipid Phase Diagrams and Tie-Lines

Lipid phase behavior has been studied for many years because of its importance to the structure and function of cell membranes (4-7). The hundreds of different amphiphilic lipids varying in size and polarity yield an astonishing array of

different phases when mixed with water. In particular, lipid bilayers exhibit two-dimensional phases called lamellar phases which are relevant biologically. At, or near room temperature and pressure, pure saturated phospholipid systems are naturally either in a liquid-disordered phase (called L_d) or a gel phase (called S_o for solid-ordered or L_β) depending on acyl chain length. Pure unsaturated phospholipid systems can exist in either phase depending on the type of unsaturation (trans or cis carbon double bonds) but generally exist in the L_d phase, although they can form gels at lower temperatures.

The lamellar, isobaric phase diagrams of binary mixtures of unsaturated and saturated phospholipids, with mole fraction and temperature as the state variables, generally show a two-phase coexistence region of L_d and gel phases within some range of temperatures. The tie-line fields for these phase diagrams are immediately known, since all tie-lines are perpendicular to the vertical temperature axis (parallel to the mole fraction axis) because of thermal equilibrium (ref 8 and references therein). However, the addition of cholesterol to either pure phospholipid systems or binary phospholipid mixtures results in a third lamellar phase, called a liquid-ordered phase (L_o), with physical properties in-between L_d and gel phases. This L_o phase can coexist with either the L_d or gel phases. Also, according to Gibbs' phase rule, a three-component lipid mixture consisting of two phospholipids, one L_d-favoring and the other gel-favoring, plus cholesterol can exhibit three-phase coexistence with variable mole fractions. This three-phase coexistence region is a triangle in the phase diagram with each vertex representing the composition of the L_d, gel, or L_o phase. Coexistence regions and three-phase triangles have been confirmed for the distearoylphosphatidylcholine(DSPC)/DOPC/cholesterol (9) and the dipalmitoylphosphatidylcholine(DPPC)/DOPC/cholesterol (10) lipid systems, and there is good evidence for a three-phase triangle in the phase diagram of the

SPM/DOPC/cholesterol lipid system (3, 11, 12, and this paper).

There are many well established methods to determine accurately and precisely phase boundaries of coexistence regions in ternary lipid systems (8-10, and 13-16), which address the challenge that some systems do not exhibit bulk (visible) phase separation. These methods are essentially divided into two types, either direct observation by fluorescence microscopy or through the measurement of some signal. However, both types rely on the presence of a probe. In addition, this probe signal can be either a spectrum, which is a vectorizable function of frequency (or magnetic field) (ESR, NMR, UV/visible/IR absorbance) or a scalar value (FRET, single-dye fluorescence, fluorescence anisotropy). The direct observation method of fluorescence microscopy, while straightforward and informative, involves a sample preparation (i.e. Giant Unilamellar Vesicles, GUVs) prone to trapping metastable states. On the other hand, the signal measurement approach allows for a well-equilibrated sample preparation, but the analysis of the data depends on the application of the linear superposition model for physical properties of phase separated systems. This approach assumes that the probe partitions between the distinct (possibly sub-microscopic) coexisting phases, and only an insignificant fraction of the probe is at the interface of the phases. Therefore, because the probe is reporting on the internal physical properties of the phase, the signal from a sample within the coexistence region is a linear combination of the signals from the coexistence curve compositions at the end points of the tie-line passing thru this total composition. In general, the linear superposition approach should be accurate for probes chemically resembling lipids. Moreover its application ultimately requires knowledge of the tie-line. Two more requirements are that the signals from the phases in coexistence be significantly different from each other and that the probe's partition coefficient not be much different from unity. The linear superposition approach can be used to determine

coexistence curves as well as tie-lines. However, experimentally determining tie-lines for lipid systems containing more than two lipid species has been difficult.

Recently, two methods have been published to determine individual tie-lines one at a time: the Veatch et al method (17) and the trial tie-line method (1, 2). Both methods use the linear superposition approach for magnetic resonance spectra and a specific compositional arrangement of samples in the experimental design, but they differ in applying the knowledge of the coexistence curve and in the partitioning behavior of the probe used, as well as the method to determine the coefficients of the linear superposition model. These methods have been applied to three different lipid systems. In the DPPC/DLPC/cholesterol (two saturated phospholipids/cholesterol) lipid mixture the trial tie-line method determined a coarse-grained tie-lie field one tie-line at a time and the results were consistent with what is known and expected for this system (1). On the other hand, the results for the DPPC/DOPC/cholesterol (saturated/unsaturated phospholipids/cholesterol) system using the Veatch et al method (17, 18) and the SPM/DOPC/cholesterol system (saturated/unsaturated phospholipids/cholesterol) system using the trial tie-line method (2) were expected to be similar but were not. The reasons for this were unknown but there are currently two limiting theories, one a regular solution theory involving a chemical interaction between saturated lipid and cholesterol (19) and the other is a mean-field theory involving differences in lipid packing due to the presence or absence of an unsaturated bond (20), which may offer insights. However, experimentally determined tie-line fields are needed to better understand such lipid phase behavior.

Currently, there have been no experimental methods to globally determine the tie-line field, as opposed to fitting one tie-line at a time. The procedure proposed in this work, which we call the tie-line field (TLF) method, does address this issue by globally determining the whole tie-line field within a two-phase coexistence region in

lipid systems. Like the previous methods, the TLF method is based on the linear superposition of magnetic resonance spectra, but it simultaneously includes all the spectra throughout the entire composition space of the coexistence region. The method, as we have developed it, requires that the boundary of the two-phase coexistence region be known, although, in principle, it could be generalized to allow for simultaneous fitting of the phase boundaries (e.g. ref 8). The heart of the method of analysis is a unique mathematical parameterization called a ruled surface. A ruled surface is any surface composed of non-intersecting line segments and can be embedded in spaces of two (planar) or more dimensions. A simple example of a ruled surface is given by the surface of a finite but open cylinder (i.e. the parallel lines along this surface connecting the two circles forming the rims of the surface). Ruled surfaces have been long known to mathematicians. The concept of a ruled surface was introduced for two-phase coexistence regions of mixtures as a function of a single composition variable vs. temperature (21-24), where for binary mixtures the ruled surface is the set of horizontal (isothermal) line segments connecting the compositions at thermal equilibrium. However, the ruled surface parameterization has not been utilized to determine tie-line fields.

B. Key Aspects of the New Methodology

In this paper we simply identify as the ruled surface the planar surface corresponding to the $L_o + L_d$ phase coexistence region (of the three component phase diagram at constant temperature), which is bounded by the coexistence curve. This surface is "ruled" by the non-intersecting tie-lines that connect the coexisting L_o and L_d phase compositions on the coexistence curve. Thus the ruled surface and the tie-line field are mathematically one and the same. That the tie-lines must not intersect follows directly from Gibbs' Phase Rule, (if there were a crossing, at the point of crossing there would be four distinct compositions in equilibrium, impossible with just

three components at constant temperature and pressure). This fundamental constraint of non-crossing is automatically included in our method, whereas in previous methods, which sought out individual tie-lines, it is more difficult to impose. The section of the coexistence curve representing the L_o phase boundary is taken as the function *u* and that for the L_d phase boundary is given by the function *v*.

Since each point along *v* is connected to a unique point along *u* by the tie-line, we can express $v = v(u)$. The task of finding the tie-line field is then just to obtain $v(u)$ from the experimental data. The non-intersection of the tie-lines merely requires $v(u)$ to be a monotonically increasing function of u, i.e. dv/du is greater than zero. Additional constraints, e.g. starting and end-points of *u* and *v* can then be introduced in the empirical parameterization of $v(u)$ as needed.

Another virtue of our method is that all the experimental data is fit simultaneously to obtain the complete tie-line field, once the problem is formulated as a constrained minimization, which can be solved by standard algorithms. This makes efficient use of all the experimental data. In fact, we show in this work that we can obtain the whole tie-line field with data sets no greater than what was needed to obtain a single tie-line in the previous study on the SPM/DOPC/Chol system (2). Furthermore, in that study, once each approximate tie-line is located, only a small fraction of the data set is useful in the statistics of the fitting.

It is clearly of interest to compare the performance of the new TLF method with the previous one (1, 2), which we refer to as the trial tie-line (TTL) method. It is for this reason that we have chosen the same $L_o + L_d$ two phase region of the SPM/DOPC/Chol system to enable a direct comparison, in this first application of the TLF method. It also enables us to illustrate some other virtues of the TLF method, which were not available in the TTL method. For example, the coexistence curve encompassing such a two phase region can be challenging to obtain in all its features.

While the coexistence curve for this system was determined by standard methods (3, 13) (i.e. confocal fluorescence microscopy and FRET), there is always the challenge of determining the putative critical point(s) on this curve, and, in the present case, the end tie-line which forms the phase boundary with the known three phase region. It is our purpose also to show that it is sufficient to have just approximate knowledge of these key features at the outset.

The TLF method, as we have developed it, is robust enough to also locate fairly accurately both the critical point and the end points of the phase boundary with the three phase region as part of the global fitting. This would be more difficult to accomplish by means of a TTL method, so greater initial effort is required in precisely locating these features prior to finding the tie-lines.

As in the previous studies using the TTL method with a spin-probe, such as 16PC, the analysis must also include the determination of its partition coefficient K_p between the L_o and L_d phases. Although it must be constant along a tie-line, there is no reason to assume that it is the same for all the tie-lines. However, there is every reason to suppose that it is a gently varying function of the ruled surface function u. This feature is naturally built into our new TLF method, whereas by means of a TTL method the K_p for each tie-line must be independently determined, which does not readily enable one to guarantee that it is a smoothly varying function of u. We do compare in our study the respective values of both K_p and the slope of tie-lines obtained by the TLF method vs. that previously obtained by the TTL method, where possible.

The outline of this Chapter is as follows: Section II provides experimental details, Section III the TLF method for fitting the data, Section IV the results of the data analysis, which provides the TLF for the SPM/DOPC/Chol system, and Section V the discussion of these results. A glossary of definitions of symbols used appears in

Appendix A, and the algorithm for obtaining the TLF is outlined in Appendix B.

II. Experimental Details

A. Materials

The phospholipids (SPM and DOPC) and the spin label 1-palmitoyl-2-(16-doxyl stearoyl) phosphatidylcholine (16PC) were purchased from Avanti Polar Lipids, Inc. (Alabaster, AL). Cholesterol was obtained from Sigma-Aldrich (St. Louis, MO). Stock solutions of the lipids were prepared by diluting or dissolving the shipped stock in chloroform in a sealable vial. Purity > 99% of the stock solutions was determined by thin-layer chromatography for phospholipids in chloroform/methanol/water = 65:25:4 (by volume) and hexane/diethyl ether/chloroform = 7:3:3 for cholesterol. All materials were used without further purification. The purity of stock solutions was checked every three months. The concentration of the phospholipid stock solutions was determined by a slightly modified procedure for the "determination of total phosphorous" published on Avanti Polar Lipid, Inc.'s website for technical information (http://www.avantilipids.com/TechnicalInformation.html). The concentration of the cholesterol stock solution was determined from an accurate mass (± 0.1mg) of the powdered cholesterol stock and the preparation of the solution in a 50 mL ± 0.05 volumetric flask.

B. Preparation of Model Membranes

Spin-labeled lipid dispersions consisting of SPM, DOPC, and cholesterol were prepared as follows. Measured volumes of lipid stocks and the spin-label stock were dispensed using a Hamilton repeating dispenser into glass test tubes using a 50 μL Hamilton syringe to give the desired lipid compositions. The concentration of spin-label in the lipid dispersion was 0.2% of the total lipids. These lipid-chloroform solutions were then converted to lipid-buffer suspensions by Rapid Solvent Exchange (25). The buffer used was 50 mM Tris, 10 mM NaCl, and 0.1 mM EDTA at pH 7.0.

The samples were stored under an argon atmosphere in the dark at room temperature for at least 24 hours to reach equilibrium. Previous work on the maximum solubility of cholesterol in phospholipid bilayers (26) demonstrated that sample preparation with temperature annealing was especially important for samples with a mole fraction of cholesterol ≥ 0.5, even if measurements were to be performed at room temperature. However, temperature annealing was not performed in the current work because none of the samples had a mole fraction of cholesterol ≥ 0.5 and the coexisting phases studied at equilibrium were both fluid; therefore, at least a day at room temperature combined with the Rapid Solvent Exchange procedure was enough to ensure complete mixing. After a few days the samples were centrifuged and the pellets were transferred to 1.5−1.8-mm-diameter × 100-mm-length glass capillaries with excess buffer. After the samples were centrifuged in the capillaries, the supernatant (excess buffer) was removed to less than a millimeter above the pellet and the ends of the capillaries were flame sealed. The samples were not deoxygenated in a glove bag because previous work showed there was a negligible difference in 16PC X-band spectra over the relevant range of compositions.

C. ESR Spectral Collections

ESR spectra were obtained on a Bruker Instruments EMX ESR spectrometer at a frequency of 9.3 GHz at room temperature (~23°C). The ESR capillary was placed inside a 2mm NMR tube which was marked to position the sample pellet in the middle of the resonator. This configuration allowed for efficiency and consistency in switching samples, tuning, and sample measurements. The spectrometer settings for all samples were as follows: center field = 3477 G, sweep width = 120 G, microwave power = 2 mW, modulation frequency = 100 KHz, modulation amplitude = 0.5 G, resolution (points) = 1024. The number of scans for each spectrum varied, but the all spectra were aligned with respect to magnetic field and normalized before analysis.

III. Data Fitting Method

A. Coordinate System for the Gibbs' Triangle

As is well-known, the equilateral Gibbs' triangle is used to represent the compositional state of a closed ternary system and is the domain for phase diagrams of ternary mixtures (Figure 3.1A). The compositional state of a lipid bilayer can be represented as a vector of mole fractions:

$$\boldsymbol{\xi} = \begin{bmatrix} \xi_S \\ \xi_D \\ \xi_C \end{bmatrix} = \xi_S \begin{bmatrix} 1 \\ 0 \\ 0 \end{bmatrix} + \xi_D \begin{bmatrix} 0 \\ 1 \\ 0 \end{bmatrix} + \xi_C \begin{bmatrix} 0 \\ 0 \\ 1 \end{bmatrix} \qquad \text{(Eqn. 3.1)}$$

where $\sum_i^n \xi_i = 1$ and $0 \le \xi_i \le 1$. In the summation *n* stands for the set of components, {S, D, C}, where S is for SPM, D is for DOPC, and C is for Cholesterol. The Gibbs' triangle lies in a three-dimensional Cartesian vector space; however, since only two of the mole fractions are independent, we perform a linear transformation to the "$\xi_s\xi_c$"-plane for a more convenient coordinate system ψ. This transformation is a combination of a projection and rotation (Figure 3.1B):

$$\psi = \mathbf{T} \times \boldsymbol{\xi} = \begin{bmatrix} 1 & 0 & \cos(\pi/3) \\ 0 & 0 & \sin(\pi/3) \end{bmatrix} \begin{bmatrix} \xi_S \\ \xi_D \\ \xi_C \end{bmatrix} = \begin{bmatrix} \xi_S + \xi_C \cos(\pi/3) \\ \xi_C \sin(\pi/3) \end{bmatrix} = \xi_S \mathbf{e_S} + \xi_C \mathbf{e_C} \qquad \text{(Eqn. 3.2)}$$

, where

$$\mathbf{e_S} = \begin{bmatrix} 1 \\ 0 \end{bmatrix}$$

and

$$\mathbf{e_C} = \begin{bmatrix} \cos(\pi/3) \\ \sin(\pi/3) \end{bmatrix}.$$

The basis vector $\mathbf{e_S}$ and $\mathbf{e_C}$ are not orthogonal but are of unit length in the Euclidean sense. We arbitrarily chose to eliminate the DOPC mole fraction.

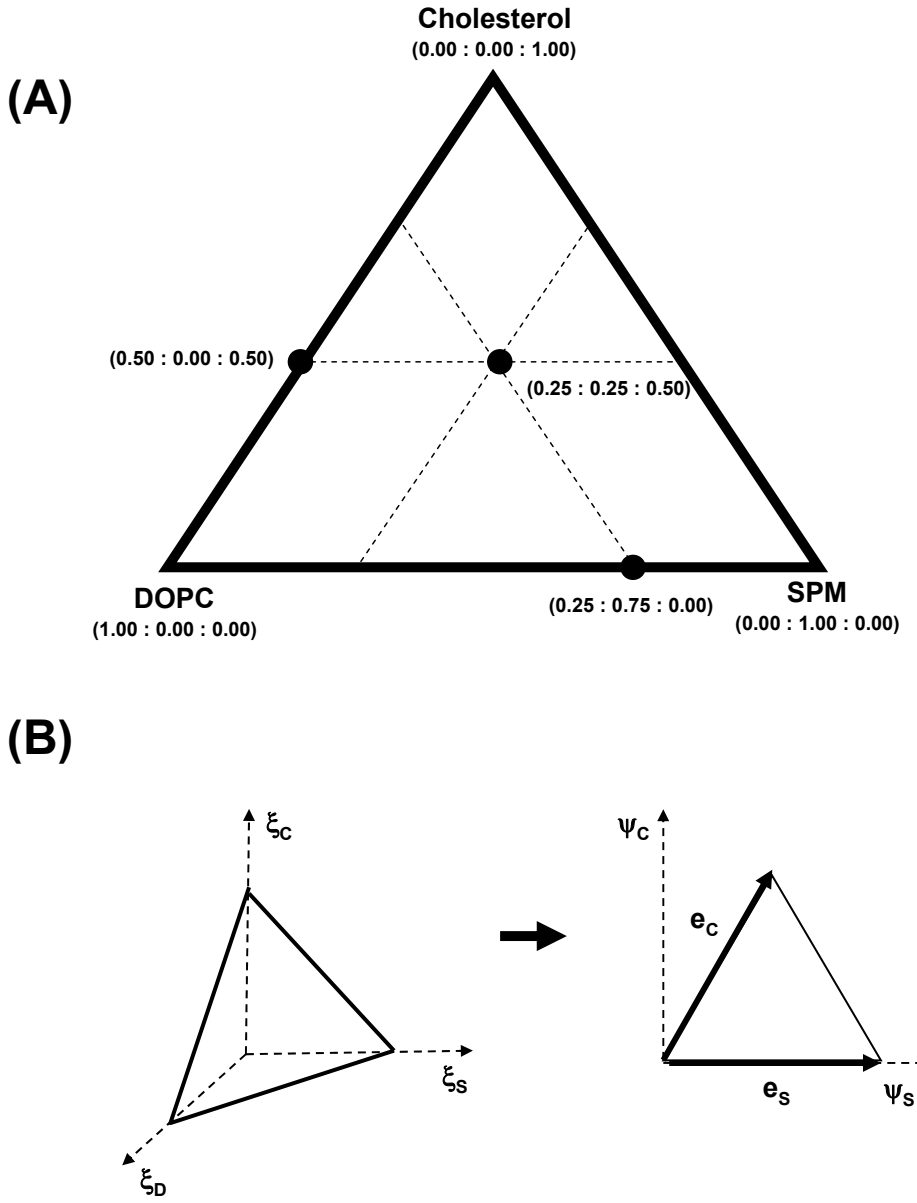

Figure 3.1: Coordinate systems to represent compositional space for ternary phase diagrams. A) The Gibbs' triangle represents mixtures of the three lipid components, brain-sphingomyelin (SPM or S), dioleoylphosphatidylcholine (DOPC or D), and Cholesterol (C), with coordinates in mole fractions. Every point within the triangle represents a ternary mixture of all three lipids. A point on an edge represents a binary mixture of either SPM/DOPC (bottom edge), DOPC/Cholesterol (left edge), or SPM/Cholesterol (right edge). The left vertex of the triangle is pure DOPC, the top vertex is pure Cholesterol, and the right vertex is pure SPM. B) The linear transformation of the Gibbs' triangle from the three-dimensional mole fraction space to the plane of the ψ-coordinate system, $\psi_S = \xi_S + \xi_C \cos(\pi/3)$ and $\psi_C = \xi_C \sin(\pi/3)$. The $\mathbf{e}_S$ and $\mathbf{e}_C$ are the basis vectors that span the Gibbs' triangle.

B. Modeling Tie-Line Fields

A tie-line field is the infinite number of tie-lines that partition a two-phase coexistence region. Our model of tie-line fields begins with a representation of the coexistence curve for a two-phase coexistence region. Figure 3.2A shows the known $L_o + L_d$ phase coexistence boundary for the SPM/DOPC/Cholesterol ternary lipid system (3, 11, and 12). This coexistence curve is shown as a closed loop or ellipse; however, two-phase coexistence regions in ternary mixtures can have different coexistence curve shapes or configurations if they intersect a three-phase coexistence triangle or a binary edge (27, 28). Two-phase coexistence regions can only contact a one-phase region and/or three-phase triangle, and the coexistence curve has a different configuration for each combination (Figure 3.2B). The closed two-phase coexistence region has two critical points (Figure 3.2B-1). An open two-phase region (Figure 3.2B-2) can either contact a one-phase region with a critical point and a three-phase triangle to its edge (called an end tie-line from the two-phase perspective), or contact a three-phase triangle with one end tie-line and another three-phase triangle with another end tie-line (Figure 3.2B-3). Results from experiments of our own (see results in this paper) and others (3, 11, 12) have indicated that the two end tie-line coexistence curve configuration does not exist for the $L_o + L_d$ region of SPM/DOPC/Cholesterol, but that the two critical point and one critical point + one end tie-line configurations are still possible, although the latter is believed to be more likely. Therefore, we only considered these two cases. They will henceforth be referred to as the "closed" (two critical points) and "open" (one critical point/one end tie-line) boundary configurations, but we shall emphasize our results for the latter (open) configuration.

Since we started with just a rough estimate of the exact location of the three-phase region (cf. Figure 3.2A), we initially utilized a closed representation of the coexistence curve; then, in our fitting of the TLF, we generated the open configuration

Figure 3.2: Coexistence curve configurations for two-phase coexistence regions and the chord-length parameterization of curves. A) The coexistence curve of the $L_o + L_d$ phase coexistence region of SPM/DOPC/Chol plotted on the Gibbs' triangle (2, 3). The short dotted-dashed section at the far left of the coexistence curve indicates roughly where there is a critical point; the dashed section to the lower right indicates a region of estimated transition between the $L_o + L_d$ two-phase region and the three-phase region (2, 3). The horizontal dotted lines represent constant cholesterol mole fractions, the 60° dotted lines represent constant SPM mole fractions, and the 120° dotted lines represent constant DOPC mole fractions. The data that is fit in the TLF method consists of compositions on the coexistence curve (20 samples connected by solid black line) and compositions within the coexistence region (51 samples, dots). Based on analysis of the 16PC ESR spectra on the coexistence curve (Figure 3.5A) and the outer hyperfine splittings of these spectra (Figure 3.5B), the coexistence curve compositions are divided into 8 L_o compositions (diamonds), 5 L_d compositions (triangles), and the 2 phase transition regions (squares). Inset: a possible open coexistence curve configuration for this two-phase coexistence region. B) The coexistence curve configurations for a two-phase coexistence region showing (1) a closed configuration with two critical points, (2) an open configuration with one critical point and one end tie-line (dashed line) to a neighboring three-phase triangle, or (3) another open configuration with two end tie-lines (dashed and dotted lines) to two different three-phase triangles. (4) The chord-length parameterization of curves is an approximate arc-length parameterization. The chord-length parameter *t* lies on the interval [0,1]. The solid line is the real curve and the entire dashed line is its polygonal representation with M total points. The chord-length parameters are calculated from the Euclidean lengths of the individual dashed intervals (i.e. chords of the curve).

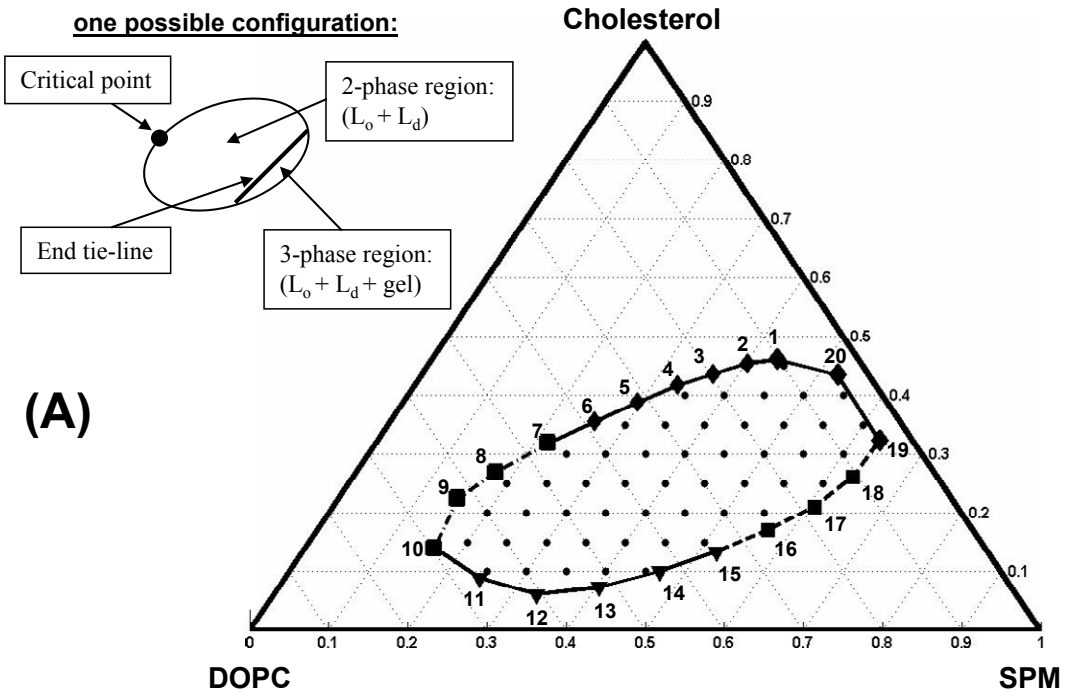
one possible configuration:
Critical point
2-phase region: (Lo + Ld)
End tie-line
3-phase region: (Lo + Ld + gel)
Cholesterol
DOPC
SPM
0
0.1
0.2
0.3
0.4
0.5
0.6
0.7
0.8
0.9
1
1
2
3
4
5
6
7
8
9
10
11
12
13
14
15
16
17
18
19
20

(A)

(B)

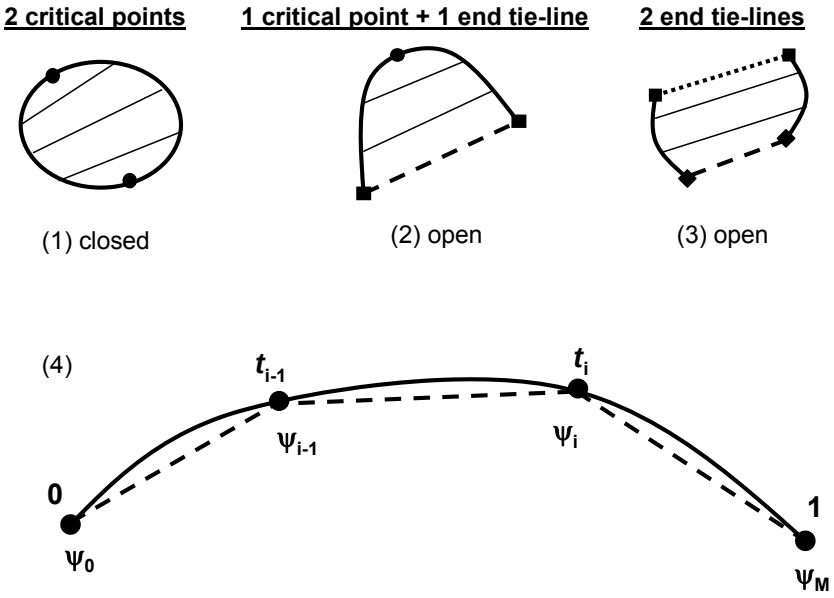
2 critical points
1 critical point + 1 end tie-line
2 end tie-lines
(1) closed
(2) open
(3) open
(4)
t_{i-1}
t_i
ψ_{i-1}
ψ_i
0
1
ψ_0
ψ_M

by assigning the end tie-line as connecting two points on the putative phase boundary (Figure 3.2A). The slopes of the tie-lines in a tie-line field are bounded by such an end tie-line and by the location of (and slope of the tangent to) the critical point(s). Therefore, the coexistence curve was parameterized to enable locating these points. These boundary parameters were then used as search parameters in fitting the data to the best tie-line field.

Generally, the coexistence curve is some smooth curve and the canonical parameterization of a curve is the arc-length. However, experimentally, it is known as a closed set of 20 points forming a 20-sided regular convex polygon. A spline representation can be fit to this polygon, but the process of fitting a general spline to a set of points and calculating the arc-length parameterization of the resulting spline curve is nontrivial. Therefore, for simplicity, we used the polygon representation of the coexistence curve and the chord-length parameterization (Figure 3.2B-4) as an approximate arc-length parameterization. This enabled convenient interpolation of measured properties (i.e. ESR spectra) along the coexistence curve. The modeling of tie-line fields also requires the relationship between the compositions along a tie-line and the compositions of the connodes (end points) of that tie-line. This relationship was calculated from the conservation of matter equations between two phases and the lever rule (Figure 3.3). That is, in terms of the number of moles of SPM, DOPC, and Cholesterol, $N_S = N_S^d + N_S^o$, $N_D = N_D^d + N_D^o$, and $N_C = N_C^d + N_C^o$, respectively. The superscript d stands for the L_d phase and the superscript o stands for the L_o phase. These expressions are readily converted to mole fractions (ξ_i) by dividing through by N, the total number of moles, enabling us to write in vector form:

$$\boldsymbol{\xi} = \begin{bmatrix} \xi_S \\ \xi_D \\ \xi_C \end{bmatrix} = \phi^d \begin{bmatrix} \xi_S^d \\ \xi_D^d \\ \xi_C^d \end{bmatrix} + \phi^o \begin{bmatrix} \xi_S^o \\ \xi_D^o \\ \xi_C^o \end{bmatrix} = \phi^d \boldsymbol{\xi}^d + \phi^o \boldsymbol{\xi}^o \qquad \text{(Eqn. 3.3)}$$

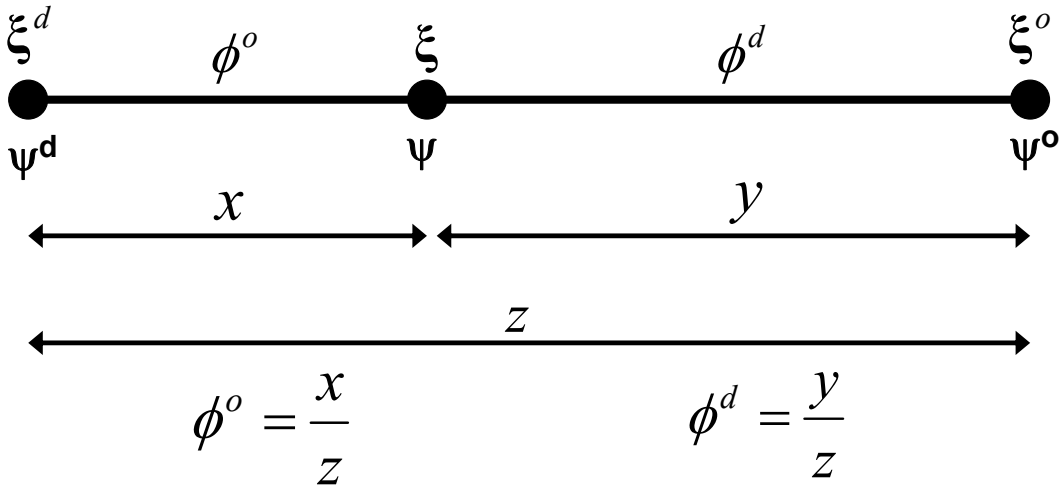

Figure 3.3: The lever rule is the solution of the conservation of matter equations for the fraction of L_o phase (ϕ^o) and L_d phase (ϕ^d) and when the coexistence composition (ξ) and the end-point compositions (ξ^d and ξ^o) are all constrained to lie on a line (i.e. tie-line). The lever rule is essentially the parameterization of a tie-line, with the fractions of phase lying on the interval [0,1]. The lever rule is invariant under our ξ to ψ coordinate transformation and has the form of a ratio of two Euclidean distances (x/z and y/z).

The coefficients ϕ^o and ϕ^d are defined as,

$$\phi^o = \frac{N^o}{N} \text{ and}$$

$$\phi^d = \frac{N^d}{N} = 1 - \phi^o,$$

where $N^o = \sum_i^n N_i^o$, $N^d = \sum_i^n N_i^d$, and $N = N^d + N^o$.

Therefore, ϕ^o is the fraction of the total number of moles of all lipid species that are in the L_o phase (i.e. the fraction of L_o phase), and ϕ^d is the fraction of the total number of moles of all lipid species in the L_d phase (i.e. the fraction of L_d phase). These coefficients can be calculated with the lever rule for composition $\boldsymbol{\psi}$ using the Euclidean norm as:

$$\phi^o = \frac{\left\|\boldsymbol{\xi} - \boldsymbol{\xi}^d\right\|}{\left\|\boldsymbol{\xi}^d - \boldsymbol{\xi}^o\right\|} = \frac{\left\|\boldsymbol{\psi} - \boldsymbol{\psi}^d\right\|}{\left\|\boldsymbol{\psi}^d - \boldsymbol{\psi}^o\right\|} \qquad \text{(Eqn. 3.4a)}$$

$$\phi^d = \frac{\left\|\boldsymbol{\xi} - \boldsymbol{\xi}^o\right\|}{\left\|\boldsymbol{\xi}^d - \boldsymbol{\xi}^o\right\|} = \frac{\left\|\boldsymbol{\psi} - \boldsymbol{\psi}^o\right\|}{\left\|\boldsymbol{\psi}^d - \boldsymbol{\psi}^o\right\|} \qquad \text{(Eqn. 3.4b)}$$

, where,

$$\boldsymbol{\psi}^d = \begin{bmatrix} \xi_S^d + \xi_C^d \cos(\pi/3) \\ \xi_C^d \sin(\pi/3) \end{bmatrix}$$

And

$$\boldsymbol{\psi}^o = \begin{bmatrix} \xi_S^o + \xi_C^o \cos(\pi/3) \\ \xi_C^o \sin(\pi/3) \end{bmatrix}.$$

As can be seen, the lever rule is invariant under our coordinate system transformation (as it must be) and it has the form of a ratio of two Euclidean distances. It should be noted that the lever rule is not the conservation of matter equations. The lever rule is the solution of the conservation of matter equations for the fractions of phase (ϕ^o and ϕ^d) when all compositions lie on a line (i.e. tie-line). The conservation of matter equations can still be solved for a coexistence composition that does not lie on the line connecting the end-point (phase boundary) compositions; however, in either case, the

constraint that the fractions of phase sum to unity still holds. The ruled surface tie-line field is the most general way to model tie-lines. Therefore, we only discuss the implementation and results of this approach. Some comments about simpler approaches are provided in the Results Section.

A ruled surface is a surface generated by a line segment moving along a curve (29) and can have the following parameterization (30):

$$\mathrm{S}(x,y) = y\,\mathrm{A}(x) + (1-y)\,\mathrm{B}(x) \qquad \text{(Eqn. 3.5)}$$

$$x, y \in [0,1]$$

The two non-intersecting space curves A(x) and B(x) are called directrices and the line segments connecting the curves are called rulings. The directrices can either be connected or unconnected. If connected, then the directrices share a common point, if not, they are unconnected. In other words, a ruled surface is the linear combination of two different curves, and can be visualized in three dimensions as the surface formed by moving a line segment through space. Any tie-line field can be expressed as a ruled surface, where the L_o boundary and the L_d boundary are the directrices and the tie-lines are the rulings:

$$\boldsymbol{\xi}(\phi^o, u) = \phi^o \boldsymbol{\xi}^o(u) + (1-\phi^o)\boldsymbol{\xi}^d(v(u)) \text{ or} \qquad \text{(Eqn. 3.6)}$$

$$\boldsymbol{\psi}(\phi^o, u) = \phi^o \boldsymbol{\psi}^o(u) + (1-\phi^o)\boldsymbol{\psi}^d(v(u))$$

$$u, \phi^o, v \in [0,1]$$

$$\frac{dv}{du} > 0$$

The function, $v(u)$, is the tie-line field function (Figure 3.4B and 3.4C-1), which specifies which connode on the L_d boundary with chord-length boundary parameter v that connects to its coexisting connode on the L_o boundary with chord-length boundary parameter u. Requiring the derivative of v with respect to u to be greater than zero insures that the tie-lines do not intersect. The parameters u and v begin and end either at the critical point(s) or the end points of the end tie-line, and, in theory,

Figure 3.4: The tie-line fields of two-phase coexistence regions have a ruled surface parameterization containing a tie-line field function for specifying how the slopes of tie-lines vary across the field. A) The ruled surface parameterizations of the coexistence curve configurations represented in Figure 2B. The u chord-length parameter specifies the L_o phase composition on the L_o phase boundary (directrix) and the v chord-length parameter specifies the L_d phase composition on the L_d phase boundary (directrix). By definition, the boundary conditions $v(0) = 0$ and $v(1) = 1$ ensure that the start point of the L_o directrix connects to the start point of the L_d directrix. B) The ruled surface parameterization of the closed $L_o + L_d$ coexistence region in the SPM/DOPC/Chol lipid system. Also shown is the total coexistence curve parameter t that specifies the location of the critical points (black squares) on the coexistence curve. C) (1) Possible (solid lines) and not possible (dashed line) functional forms for the tie-line field function $v(u)$ of the ruled surface parameterization. (2) The tie-line field function used in our TLF method plotted with different values of the variable parameter c.

(A)

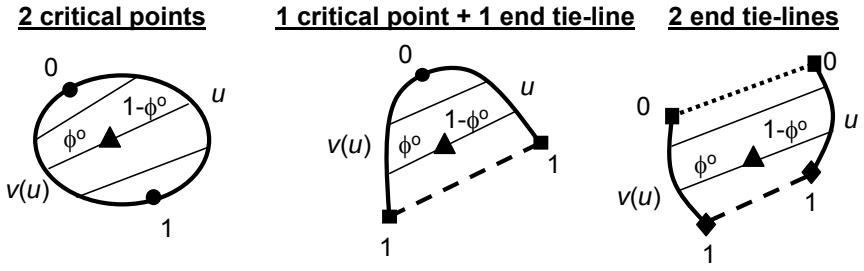
2 critical points
1 critical point + 1 end tie-line
2 end tie-lines
0
u
1-ϕ°
ϕ°
v(u)
1

(B)

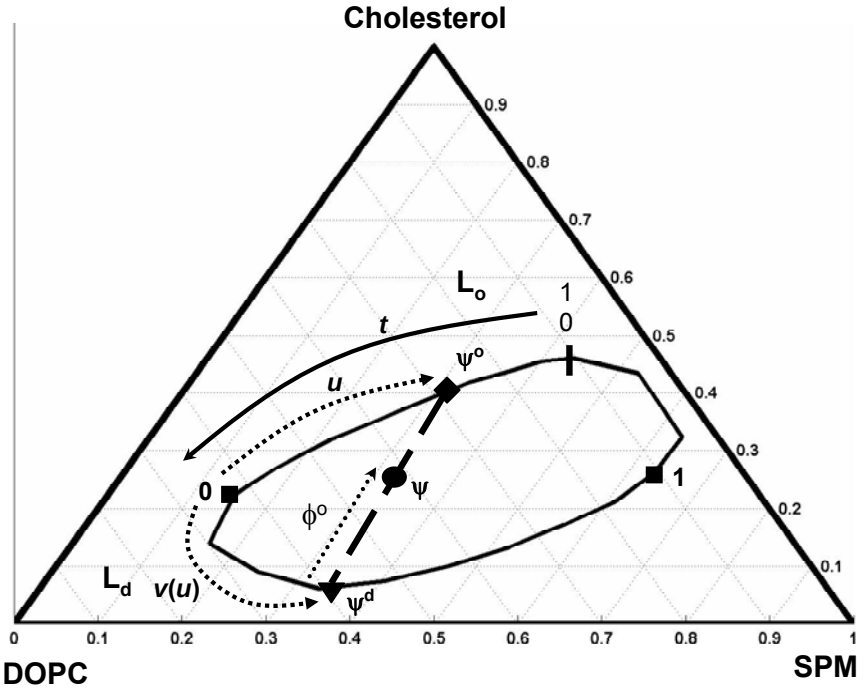
Cholesterol
DOPC
SPM
L_o
L_d
t
u
v(u)
ψ°
ψ
ψ^d
ϕ°
0
1

(C)

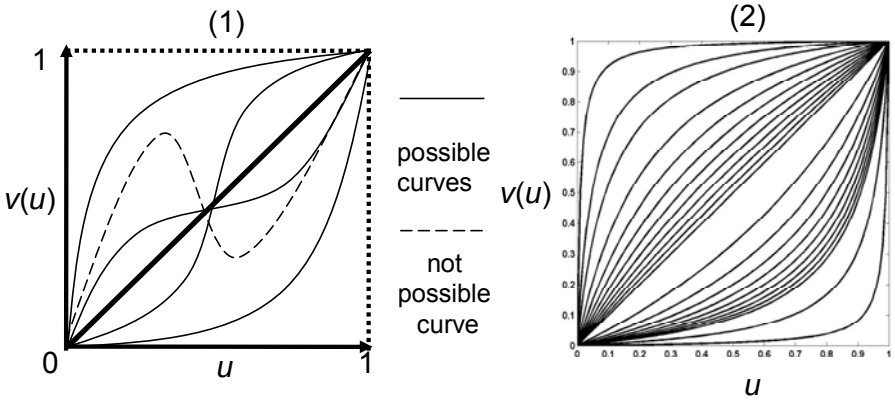
(1)
(2)
v(u)
u
possible curves
not possible curve

can be parameters from any curve parameterization. The coexistence curve configurations for two-phase regions (Figure 3.2B) are shown parameterized as ruled surfaces in Figure 3.4A. The ruled surface parameterization for the closed coexistence curve configuration of the $L_o + L_d$ coexistence region in the SPM/DOPC/Cholesterol system is shown in Figure 3.4B. The tie-line field function determines how the slopes of the tie-lines vary. We adopted a simple form (Figure 3.4C-2) with just a single parameter *c* to be fit for purposes of the present study:

$$v(u) = \frac{u}{u + c(1-u)} \qquad \text{(Eqn. 3.7)}$$

In Eqn. 3.7, $c > 0$, $v(0) = 0$, and $v(1) = 1$. This form for *v* increases monotonically with *u* and satisfies the boundary conditions *v*(0) = 0 and *v*(1) = 1, consistent with the constraints of Eqn. 3.6..

The essential aspect of finding the correct tie-line field for a given coexistence curve is to find the best tie-line field function *v*(*u*) using the ruled surface parameterization. Then a tie-line through a particular point in the coexistence region is the line thru this point that solves the ruled surface parameterization for the L_o boundary parameter (*u*), fraction of the L_o phase (ϕ^o) obtained from the lever rule, and the tie-line configuration function (*v*), which is also the L_d boundary parameter. Different tie-line fields are searched in the least squares fitting by varying the locations of the critical point(s) and/or end points of the end tie-line (within their range expected from experiment), which determine the end-points of the phase boundary directrices from which to calculate the chord-length parameters *u* and *v*(*u*), as well as by varying *c*. The method could, of course, be extended to more sophisticated forms of parameterization than that of Eqn. 3.7.

C. Fitting ESR Spectra

The ESR data consist of spectra obtained from known sample compositions within the two-phase coexistence region and on the coexistence curve. On the whole,

the fitting method involves searching different tie-line fields, each generating trial spectra for the two-phase region by linear combination of the coexistence curve spectra, and then performing a least squares fit of these trial spectra to the experimental spectra within the coexistence region. As needed, coexistence curve spectra located at coexistence curve compositions between the known compositions at which spectra have been experimentally determined are obtained by linear interpolation. For our analysis, ESR spectra are taken as signal vectors, that is a discretization of the derivative signal versus magnetic field. Within a two-phase coexistence region the signal vector, **S**, at a specific bulk (total) composition is a linear combination of the coexistence curve signal vectors, $\mathbf{S}^d$ and $\mathbf{S}^o$, at the endpoints of the tie-line (i.e. connodes):

$$\mathbf{S} = f^o\mathbf{S}^o + f^d\mathbf{S}^d, \qquad \text{(Eqn. 3.8)}$$

where $f^d + f^o = 1$ and $f^d, f^o \in [0,1]$. The coefficients f^o and f^d are defined as,

$$f^o = \frac{N_p^o}{N_p}$$

and

$$f^d = \frac{N_p^d}{N_p}$$

, where f^o is the fraction of total spin-probe that is in the L_o phase and f^d is the fraction of total spin-probe in the L_d phase. Through the ruled surface parameterization of tie-line fields, the linear combination of spectra can also be considered as a ruled surface:

$$\mathbf{S}(f^o, \xi(\phi^o, u)) = f^o\mathbf{S}^o(\xi^o(u)) + (1-f^o)\mathbf{S}^d(\xi^d(v(u))) \qquad \text{(Eqn. 3.9)}$$

$$\Rightarrow \mathbf{S}(f^o, u) = f^o\mathbf{S}^o(u) + (1-f^o)\mathbf{S}^d(v(u))$$

However, the space of tie-line fields and the space of spectra are different, and are related through a nonlinear transformation involving the partition coefficient of the spin-probe, K_p. From the conservation of total spin-probe in the two phases and the definition of mole fractions (similar for the lipids, cf. Eqn 3, in the low concentration

limit),

$$\xi_p = \phi^o \xi_p^o + \phi^d \xi_p^d \qquad \text{(Eqn. 3.10)}$$

, and with the definition of K_p,

$$K_p \equiv \frac{\xi_p^o}{\xi_p^d} \qquad \text{(Eqn. 3.11)}$$

, the transformation between the spaces can be written as,

$$f^o = \frac{K_p \phi^o}{\phi^d + K_p \phi^o} \text{ and } f^d = \frac{\phi^d}{\phi^d + K_p \phi^o} \qquad \text{(Eqn. 3.12)}$$

Therefore, the linear (convex) combination of spectra is from Eqn 8,

$$\mathbf{S} = \frac{K_p \phi^o}{\phi^d + K_p \phi^o} \mathbf{S}^o + \frac{\phi^d}{\phi^d + K_p \phi^o} \mathbf{S}^d \qquad \text{(Eqn. 3.13)}$$

Eqn. 3.13 displays the connection between the ESR data and the tie-line field via K_p.

Since the K_p is constant along a tie-line (i.e. independent of ϕ^o), the K_p across tie-lines is a function only of the L_o boundary parameter *u*, and its form depends on the coexistence curve configurations (i.e. open or closed) and certain boundary conditions, which are that the K_p at a critical point is unity and the K_p at an end tie-line is greater than zero. For the closed boundary case we chose the following simple form for parametrizing K_p:

$$K_p(u) = 1 - \frac{a}{2} \times u(1-u), \qquad \text{(Eqn. 3.14)}$$

for which $K_p(0) = 1$ and $K_p(1) = 1$ as required at the critical points. For the open boundary case, we chose this form:

$$K_p(u) = 1 + au + bu^2 \qquad \text{(Eqn. 3.15)}$$

with $K_p(0) = 1$ and $K_p(1) > 0 \Rightarrow a + b > -1$. The fitting parameters are "*a*" and "*b*". These forms imply that the K_p function is a smooth and slowly varying analytical function that obeys certain boundary conditions; so it was expanded as a Taylor's series around the critical point(s), keeping only lowest order terms. As seen below, it provides a reasonably accurate fit to the experimental data.

In summary, predicting an ESR spectrum at a composition within the coexistence region involves determining the L_o and L_d boundary parameters *u* and *v* of the tie-line through that coexistence composition from the ruled surface parameterization of the TLF, and in addition evaluating the K_p for that tie-line using the K_p function (Eqn. 3.14 or 3.15). Next, the spectra at the tie-line end-point compositions are found by interpolating the experimentally determined boundary spectra, and then the predicted spectrum at the coexistence point is calculated using Eqn. 3.13.

At this point it is useful to compare the tie-line field (TLF) method with the tie-line determination method previously published (1), henceforth called the trial tie-line (TTL) method, because the fitting criterion we use for the TLF method in this work is based on that used in the TTL method. First, the TTL method uses the set of compositions along each of several trial tie-lines and determines which of them provides the best spectral fit, providing just a single best-fit tie-line at a time. The TLF method determines the whole TLF from the global set of coexistence samples. In the TTL method K_p is a parameter that is allowed to vary independently for each coexistence composition on a trial tie-line during the fitting of the coexistence spectrum. Then the standard deviation of this set of K_p's (i.e. σ_{K_p}) along the i^{th} TTL is used to weight the quality of the spectral fit of the TTL given by its average reduced chi-square, $\left\langle \chi^2_{red} \right\rangle_i$. Thus one has for the i^{th} TTL the weighted or "effective" chi-square:

$$(\chi^2)_i = \left\langle \chi^2_{red} \right\rangle_i \times \left(\sigma_{K_p} \right)_i \qquad \text{(Eqn. 3.16)}$$

The χ^2_{red} is for one coexistence composition and the average is over all coexistence compositions on the i^{th} TTL. Eqn 3.16 was utilized because it was found to yield better predictive results than finding the best fit for all spectra along the trial tie-line simultaneously with optimizing the value of K_p. We developed our fit criterion with

this observation in mind, but generalized for the TLF method. The algorithm for the fitting procedure that we adopted is given in Appendix B.

IV. Results

A. ESR Data and Transition Regions on the Coexistence Curve

The data that were fit for determining the best tie-line field were the sample compositions in mole fractions and the ESR spectra obtained at those compositions. The compositions on the coexistence curve and within the $L_o + L_d$ coexistence region of the SPM/DOPC/Chol phase diagram are shown in Figure 3.2A. There were 20 compositions on the coexistence curve and 51 compositions within the coexistence region. It is very desirable to determine the coexistence curve as precisely as possible. We estimate that the uncertainty in the position of the coexistence curve is no greater than 5%, which are the compositional increments of the experimental procedures (i.e. confocal fluorescence microscopy and FRET) used to determine the coexistence curve (3, 13), whereas the minimum uncertainty is no less than 1%, which is the precision of commercially available volumetric syringes for dispensing liquids that were used to prepare the samples. We estimate that the uncertainty in the composition of our samples is no greater than 2%, since our sample preparation method was optimal for minimizing this uncertainty. In publications of other phase diagrams (DPPC/DOPC/Chol and DSPC/DOPC/Chol) an uncertainty in phase boundaries of between 2% and 5% was also estimated (9, 10), and the experiments used to determine the SPM/DOPC/Chol phase diagram were similar. In our experiments, the samples within the coexistence region were selected to provide an even distribution of 5% compositional increments in sphingomyelin and cholesterol for convenience and to provide good coverage of the whole coexistence region.

All ESR spectra are from the 16PC spin-probe, which is an end-chain labeled phosphatidylcholine (1, 2). The spectra from the coexistence curve compositions are

shown in Figure 3.5A. The transition regions were determined by visual inspection of the spectra and the outer hyperfine splittings (Figure 3.5B). A transition region of the coexistence curve is where a L_o phase changes to an L_d phase (or vice versa), or, more precisely, the compositional range where either a critical point or an end tie-line is located. Visually, the spectra (Figure 3.5A) from samples 7 to 10 change gradually and continuously, which we expect for passing through a critical point, wherein L_o and L_d phases become indistinguishable. Also, the outer hyperfine splittings (Figure 3.5B) for this range of samples level off from the rapidly dropping values of samples 1 thru 6, but are not as small as the L_d values from samples 11 thru 15. However, the spectral changes from samples 16 to 19 are not continuous or gradual, which we expect for transiting through a three-phase region and thus implying a nearby end tie-line for the $L_o + L_d$ two-phase region. Also, the spectra within this range, specifically 16, 17, and 18, visually show an additional component within the low-field and high-field ends of the spectra that resembles 16PC spectra from a gel phase composition within the SPM/DOPC/Chol lipid system. In addition, the outer hyperfine splittings increase rapidly over this range suggesting a transition from a more disordered phase to a more ordered phase. The existence of these transition regions was further supported by the order parameter profile of these coexistence curve spectra obtained from non-linear least squares fitting of the spectra to a well-known dynamic model used in ESR (31) (results to be published).

In summary, based on the analysis of the coexistence curve spectra, we estimated that a critical point lies somewhere between the compositions of point 7 ($\xi_S = 0.22$, $\xi_D = 0.46$, $\xi_C = 0.32$) and point 10 ($\xi_S = 0.16$, $\xi_D = 0.70$, $\xi_C = 0.14$), which we call the critical point region (CPR). Also, we estimate a three-phase coexistence

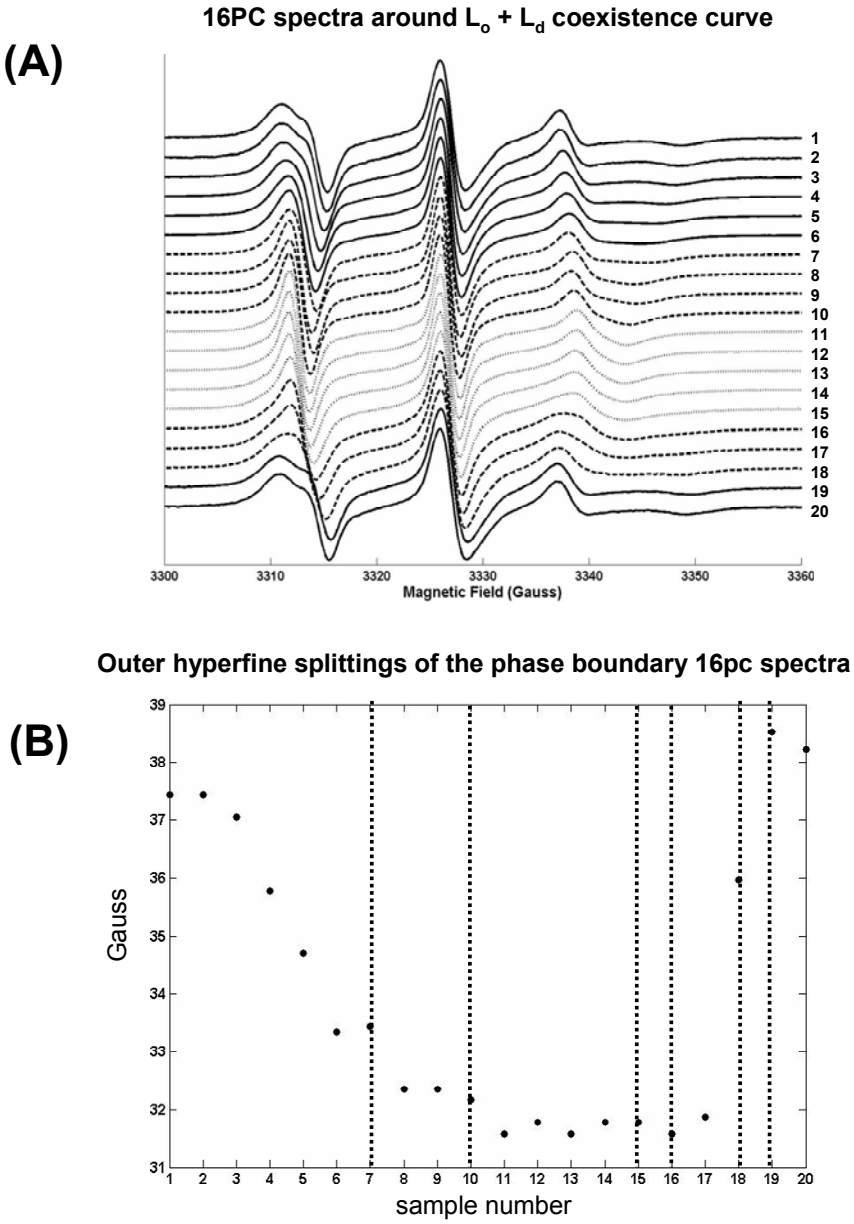

Figure 3.5: ESR spectra obtained from compositions along the coexistence curve reveal the expected compositional range for a critical point (CPR) and end tie-line (ETR) for the open coexistence curve configuration of the L_o + L_d coexistence region of SPM/DOPC/Chol. A) Stack plot of the 16PC ESR spectra on the coexistence curve showing the L_o spectra (solid lines), L_d spectra (dotted lines), and the CPR and ETR spectra (dashed lines). The low-field and high-field regions flanking the central peak in spectra 16, 17, and 18 show visually the appearance of gel-phase spectral components. B) Plot of the outer hyperfine splitting with sample number along the coexistence curve showing the CPR and ETR (between the dotted lines) having different profiles.

boundary with vertex lying between point 15 ($\xi_S = 0.52$, $\xi_D = 0.34$, $\xi_C = 0.13$) and 16 ($\xi_S = 0.57$, $\xi_D = 0.26$, $\xi_C = 0.17$), and another vertex lying between point 18 ($\xi_S = 0.63$, $\xi_D = 0.11$, $\xi_C = 0.26$) and 19 ($\xi_S = 0.63$, $\xi_D = 0.04$, $\xi_C = 0.32$). Also, we concluded that samples 16 thru 18 were within the three-phase region. Therefore, for clarity of exposition, the transition region for the two vertices (points 15 thru 16 and points 18 thru 19) are called the end tie-line regions (ETR). These estimates are consistent with the previous estimates of the three-phase coexistence boundary from the FRET and fluorescence measurements (2, 3, and cf. Figure 3.2A).

B. Performance of the Tie-Line Field Method on Synthetic Data Sets

Before analyzing the actual experiments, we first performed tests of the method on synthetic data sets. A synthetic data set was generated by linearly combining the coexistence curve spectra for each composition in the coexistence region using an arbitrarily chosen critical point, end tie-line, value of *c* in Eqn 7 (to specify the TLF) and arbitrary coefficients in Eqn. 3.14 and 3.15 (to specify the K_p function). The interior reflective Newton method with conjugate gradients (built-in Matlab function "lsqnonlin") and the constrained simplex search method ("fminsearchcon" written by John D'Errico, woodchips@rochester.rr.com, released 12/16/06 and obtained from Matlab Central) were compared with data sets that had essentially no noise (s/n ~ 3000) or were very noisy (s/n ~ 70) to determine their effectiveness for fitting. It should be emphasized, however, that our experimental results are best approximated by the s/n ~ 3000 case. The fitting was started from 10 random starting points, and true convergence to the global minimum was determined if the set of parameters obtained was within 5% of the true minimum.

The simplex search method outperformed the Newton search method in locating the global minimum for the very low-noise data sets; however, the simplex search had about four times as many function calls (data not shown). Both did equally

poorly with the very noisy data. The ruled surface field with an open boundary configuration has six adjustable parameters (3 for the location of the critical point/end tie-line points, 1 for the tie-line field function, and 2 for the K_p function). In the low noise case, good convergence was obtained to the true values, but some trials yielded nearby local minima, differing slightly in the values of the parameters, but virtually the same TLF. We found this feature was closely associated with the initial (or seed) choice of the critical point and end tie-line boundary parameters.

Since we found that convergence of a fit to the true global minimum strongly depended on thoroughly searching the critical point and end tie-line boundary parameters, the procedure we used to stably analyze the real data set was to do a grid search over these parameters. The critical point search range was bounded by samples 7 and 10, and the grid interval was chosen as the boundary parameters of the intervening points. The end tie-line search range was bounded by samples 15/16 and 18/19, but no smaller interval was specified since these points were so close together and within the region of good convergence to a minimum. Therefore, at each point of the grid the boundary parameters of the critical point and end points of the end tie-line were fixed and the remaining search parameters were varied under the simplex search algorithm. After the minimum over all the grid points was found, a further simplex search was done within the restricted ranges for the critical point and the end tie-line to find the global minimum.

C. The Best-Fit Ruled Surface Tie-Line Field

For the expected CPR and ETR (Figure 3.2A), the best-fit ruled surface parameters ($\chi^2 = 34.38$) and their errors are shown in Table 3.1. The uncertainty or errors in the parameters of the ruled surface TLF was determined by a Monte Carlo simulation (33), which proceeded as follows. During each iteration of the simulation, a synthetic data set was generated by adding normally distributed noise, with a

Table 3.1: The parameters and their uncertainties (σ) of the best-fit ruled surface TLF for the open boundary configuration of the L_o + L_d coexistence region of the SPM/DOPC/Cholesterol lipid system.†

Parameter	Critical point*	End tie-line vertex 1*	End tie-line vertex 2*	Tie-line field parameter *c*	K_p parameter *a*	K_p parameter *b*
value	0.35 *(a)*	0.70 *(b)*	0.90 *(c)*	2.3	4.3	–3.9
σ	±0.01 (3%)	±0.02 (2%)	±0.01 (1%)	±0.4 (19%)	±0.3 (6%)	±0.4 (9%)

† The uncertainties were estimated by a Monte Carlo simulation. The number of Monte Carlo iterations was 100. To generate the synthetic data sets for the simulation, noise was added to the coexistence spectra and compositions but not to spectra and compositions on the coexistence curve.

* These give the value of *t*, defined in Figure 3.4B, which gives the location on the coexistence curve.

(a) This corresponds to the composition: $\xi_S = 0.15$, $\xi_D = 0.64$, $\xi_C = 0.20$, with ±0.01 component uncertainty (cf. Figure 3.6A)

(b) This corresponds to the composition: $\xi_S = 0.55$, $\xi_D = 0.30$, $\xi_C = 0.16$, with ±0.02 component uncertainty (cf. Figure 3.6A)

(c) This corresponds to the composition: $\xi_S = 0.63$, $\xi_D = 0.05$, $\xi_C = 0.31$, with ±0.01 component uncertainty (cf. Figure 3.6A)

variance taken from the spectral baseline, to the best-fit predicted spectra ($\mathbf{S}^{P}$) for each coexistence composition and uniformly distributed noise of 2% was added to the coexistence compositions themselves, then this synthetic data set is fit the same way as the real data set. The standard deviation of the distribution of the difference between the best-fit parameter from the synthetic data sets and the best-fit parameter from the real data set was the error estimate for that parameter. Since the ruled surface TLF parameters are highly coupled and interdependent, the sources of their uncertainty are difficult to diagnose. However, the lower the uncertainty the more confident we are in the value of the parameter and the more important the parameter is to getting the best-fit to the data. Therefore, the boundary parameters for the location of the critical point and end tie-line are the most important (i.e. the lowest uncertainty) in determining the best-fit to the ESR data (Table 3.1). The errors for these boundary parameters are close to the estimated variability of the coexistence curve (2%–5%). We find the critical point at a composition of ($\xi_S = 0.15$, $\xi_D = 0.64$, $\xi_C = 0.20$, with an average uncertainty in each component of ±0.01) and the end tie-line vertices at the compositions ($\xi_S = 0.55$, $\xi_D = 0.30$, $\xi_C = 0.16$, with ±0.02 component uncertainty) and ($\xi_S = 0.63$, $\xi_D = 0.05$, $\xi_C = 0.31$, with ±0.01 component uncertainty), cf. Table 1 and Figure 6A. The best-fit ruled surface tie-line field is shown in Figure 3.6A. The slopes of the tie-lines through the experimental coexistence compositions (Figure 3.6B) were calculated numerically. The slope of the end tie-line ($u = 1$) is 40°. The profile exhibited a maximum at $u = 0.65$ with a slope of 52.8°. This L_o boundary parameter corresponds to the tie-line that connects a L_o phase with composition, $\xi_S = 0.40$, $\xi_D = 0.15$, $\xi_C = 0.45$, having one of the highest concentrations of cholesterol, to an L_d phase with composition, $\xi_S = 0.35$, $\xi_D = 0.60$, $\xi_C = 0.06$, having one of the lowest concentrations of cholesterol. In addition, the slope for the lowest L_o boundary parameter for an experimental coexistence composition ($u = 0.24$) is 47.0°. As u

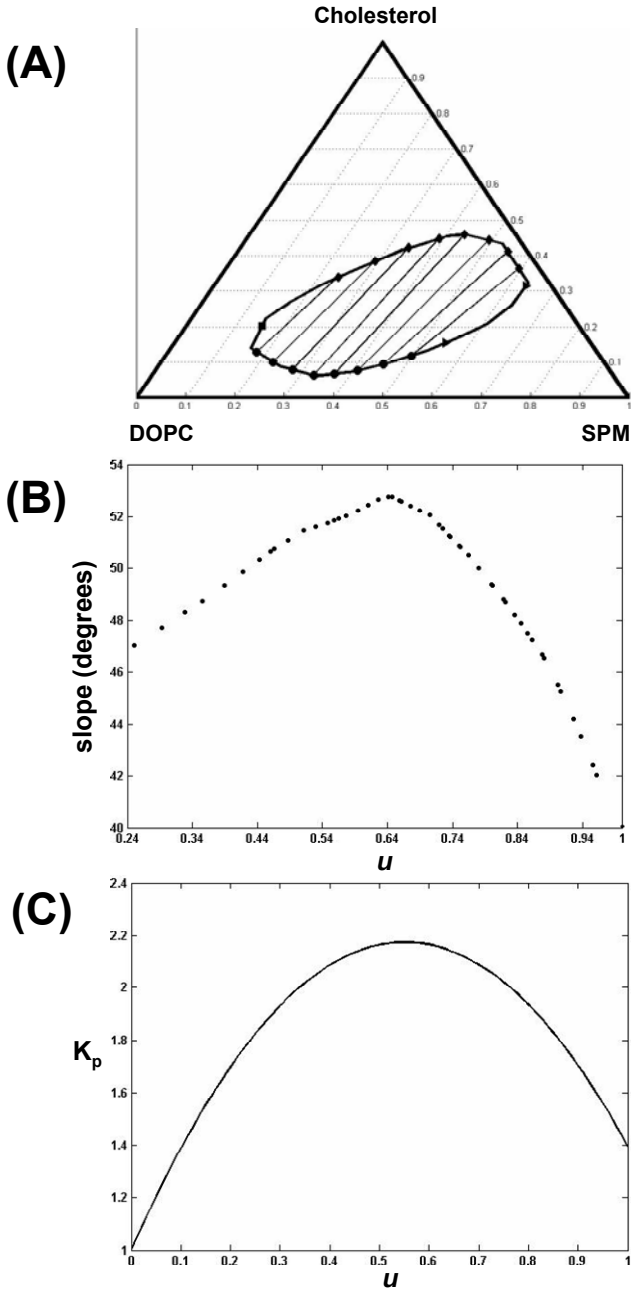

Figure 3.6: The ruled surface TLF best fit to the ESR data for the open boundary configuration of the $L_o + L_d$ coexistence region of the SPM/DOPC/Chol lipid system with the expected CPR and ETR. A) A plot showing some tie-lines from the TLF, the critical point (square), end-points of the end tie-line (triangles), L_o phase compositions (diamonds), and L_d phase compositions (dots). B) The slope profile of the TLF showing a maximum slope of 52.8° and an end tie-line with a slope of 40°. C) The K_p function of the TLF showing a maximum K_p of 2.17 and a K_p of 1.40 at the end tie-line ($u = 1$); a $K_p > 1$ favors the L_o phase.

approaches zero the tie-line slopes approach the slope of the tangent line to the critical point, as they should geometrically. However, the numerical calculation of the tie-line slopes near the critical point is unreliable because of the lack of sufficient data near the critical point, as well as the restrictions the tie-line field function imposes on the tie-line slopes as the critical point is approached. A more sophisticated tie-line field function that takes into account the slope of the tangent lines to the boundary approaching a critical point would be an improvement. A previously determined tie-line in this system from the TTL method was found to have a slope of 65° ± 5° (2). From the uncertainty in the tie-line field function parameter ("*c*" in Table 3.1), the error in the slope of a similar tie-line of the ruled surface tie-line field is 50° ± 5°. These results do not agree exactly, but, since the TTL and TLF methods are fundamentally different (e.g. the TTL method does not have the non-crossing constraint with respect to other tie-lines), we expect minor deviations. For all values of *u*, and thus all tie-lines, the K_p was greater than unity (Figure 3.6C), showing that 16PC preferentially partitions into the L_o phase. A K_p slightly greater than unity value ($K_p = 1.1 \pm 0.5$) was found previously for the tie-line determined by the TTL method within this lipid system (2). This compares favorably to a similar tie-line in the ruled surface TLF with $K_p = 1.6 \pm 0.5$ (where the uncertainty in K_p has been estimated from those of "*a*" and "*b*" in Table 1).

We have also considered two simpler models for a TLF that have been discussed previously (33). The simplest is, of course, one of parallel tie-lines. This case is easily implemented using our methodology. It is however too restrictive for a realistic multi-component system, (e.g. it requires the tangent to the critical point and the end tie-line, for an open system, to be parallel). Nevertheless, our result, using this approach, yields a parallel TLF with a slope of 33° from our data. The second approach is that of a "common vertex". This refers to an intersection point formed by

the intersection of the tangent to the critical point and the end tie-line. It is assumed that all tie-lines intersect this common vertex. We note that there are numerous experimental phase diagrams for many different systems which show TLF's that seem to conform to this configuration (33). Our analysis of this approach yielded tie-line slopes varying monotonically from 52° (for $u = 0$) to 41° (for $u = 1$). This is comparable to the range observed for the ruled surface (cf. Figure 3.6). Also we find the K_p varying from unity to a maximum of 2.1 (occurring at $u \sim 0.6$), corresponding closely to the ruled surface result. However, we regard the ruled surface TLF approach as the more general one, which does not require the simplifying constraints of the parallel and common vertex models. Also, in a comparison of the three models, the ruled surface TLF gave the best fit statistically to the ESR data despite having more fitting parameters (results not shown).

V. Discussion

A. Conclusions from This Study

The work presented in this paper provides several important conclusions. The TLF method provides a general way to experimentally determine tie-lines in any lipid system efficiently and with little or no constraint on the type of data. Furthermore, the ruled surface parameterization of tie-line fields allows a data fitting procedure to be formulated and solved using standard algorithms. This formulation also highlights the importance of the probe partition coefficient as the mediator between the TLF and the data. In the application of the TLF method to the $L_o + L_d$ coexistence region of the SPM/DOPC/Chol lipid system, the determined TLF conformed to previous information on this lipid system, and it offers a path for further research in studying phase behavior.

Analysis of cw-ESR spectra from an appropriate spin-labeled probe can be used to determine phase transition regions containing critical points and end tie-lines

bordering three-phase triangles in ternary lipid mixtures. The 16PC spectra from compositions along the $L_o + L_d$ coexistence curve of the SPM/DOPC/Chol lipid system (Figure 3.5A) show clear transition regions from L_o phases to L_d phases, and this enables us to distinguish these regions as transiting through a critical point or a three-phase triangle. The spectra around the critical point exhibit smooth spectral changes, while spectra through the three-phase triangle exhibit gel-phase spectral components and abrupt spectral changes. Although the cw-ESR spectra from 16PC can only give a range of compositions, constraining the possible critical point and end tie-line locations greatly improves convergence to the global minimum because of their importance in the fitting procedure. Additional cw-ESR spectra from other probes (such as the cholesterol analogue, cholestane) or data from techniques with better resolution of components, such as 2D-ELDOR (8) may be sufficient to narrow the phase transition regions (i.e. CPR and ETR).

However, since we found that the critical point location is determined in the fitting to high precision, the TLF method provides a way, in principle, to determine very precisely the location of the critical point. We do not conclude that we precisely located the critical point for the $L_o + L_d$ region of SPM/DOPC/Chol because of correlation in its fitting with the parameters for the tie-line field function and partition coefficient function, which have substantially greater uncertainty. Therefore, reduction of confidence intervals for these parameters, through higher quality data (e.g. 2D-ELDOR) and/or better tie-line field and partition coefficient functions, will improve the confidence of the exact location of the critical point.

B. Comparison of the TLF Method to Other Experimental Methods

There have been two other experimental methods to determine tie-lines in ternary lipid systems, the TTL method (1) and the method of Veatch et al (17). The main difference between them and the TLF method, as we previously noted, is that the

latter determines all tie-lines through a coexistence region whereas the other methods determine one tie-line at a time, thereby generating a "coarse-grained" TLF. A disadvantage of determining a TLF one tie-line at a time is the non-trivial way of constraining the tie-lines to not intersect; whereas, in the TLF method, this constraint is implicit in the ruled surface parameterization. In addition, as we have already shown, the TLF method is more efficient in its data requirements. The main similarity of all three methods is the application of the linear superposition model to magnetic resonance spectra. Both the TLF and TTL method were used to analyze ESR spectra and the Veatch et al method to analyze NMR spectra; however, each of these methods should be equally applicable to studies using ESR or NMR data. That is, the data analysis employing the linear superposition model and the lever rule involve common aspects independent of the source of the spectra. Therefore, a comparison of the TLF method with the other tie-line determination methods, independent of data type, is appropriate.

As already mentioned, the TLF method and the TTL method share a similar fit criterion; however, they differ in the manner of searching for the tie-lines: either one at a time as in the TTL method, or the field as in the TLF method. Although both methods use compositions and spectra from the coexistence curve, the TTL method directly searches for a tie-line by varying the slope of trial tie-lines from a common point on the coexistence curve, with each trial tie-line containing a linear arrangement of sample compositions through the coexistence region. The TLF method searches the tie-line fields by varying the parameters for the ruled surface parameterization. As a result, in the TTL method, the slopes of the trial tie-lines are naturally constrained with respect to each other, but within the "coarse-grained" TLF, the slopes of the best-fit trial tie-lines are essentially unconstrained with respect to each other. An advantage of the direct search for a tie-line in the TTL method is that many samples of data along

a trial tie-line offer a statistically better estimation of the K_p and its standard deviation for that trial tie-line. This estimation of K_p variability is needed when comparing other trial tie-lines because of the requirement of constant K_p along tie-lines. The disadvantage of the TTL method is the amount of work needed to determine a "coarse-grained" TLF. For example, we used a total of 71 samples for the TLF method in this work and 77 samples to determine one tie-line in the same lipid system using the TTL method (2).

The Veatch et al method is a much different one from the TLF method. Their method is an attempt to generalize a well-known NMR method for determining phase boundaries in binary systems (34, 35) to use for determining tie-lines (and phase boundaries) in ternary systems. The NMR method for determining phase boundaries in binary systems (where the tie-lines are immediately known) consists of two basic steps: 1) Spectral subtraction of two spectra from two coexistence compositions (A and B) to get the basis (i.e. tie-line end-point) spectra and the fractions of total deuterated (D) lipid probe $f_{D,i}^{o}$ and $f_{D,i}^{d} = 1 - f_{D,i}^{o}$ for each coexistence spectra (i = A,B). This method relies on the ability to clearly distinguish the spectra for each phase. The basis spectra are determined by visual inspection using the concept of a "reference" spectrum for each phase. 2) Then these values of $f_{D,i}^{o}$ and the overall mole fractions of DPPC and Cholesterol in these samples can be used with the conservation of matter equations (Eqn. 3.3 including associated definitions, but for binary systems) to obtain the phase boundary compositions given by ξ_C^o and ξ_C^d.

The Veatch et al method requires "reference" spectra representing just the L_o phase and just the L_d phase. Then they obtain spectra within the two-phase region. But here they obtain a spectrum for a single composition A and a range of B compositions along a line within the coexistence region. By means of spectral subtraction of the A spectrum from each of the B spectra they obtain a series of "trial"

L_o and L_d spectra, which are then compared with the reference spectra. The best estimate of the tie-line is taken as the line connecting the point A with that composition of B yielding the best agreement between the spectral subtraction results and the reference spectra in a least squares sense. Only one (or a few) reference spectra are taken in each phase. The assumption is made that there is little change with composition in the NMR spectrum taken within a single phase, and whatever spectral change occurs may be approximately corrected by small changes in ordering requiring only a small rescaling of the spectral frequency (x) axis. This is done as part of the least square fitting. Once the best tie-line slope is determined, the end-points of the tie-line are found by substituting

$$\phi^o = \frac{\xi_{DPPCd62}}{\xi^o_{DPPCd62}} f^o_{DPPCd62} \text{ and } \phi^d = \frac{\xi_{DPPCd62}}{\xi^d_{DPPCd62}} f^d_{DPPCd62}$$

for the fraction of L_o and L_d phase into the conservation of matter equations (Eqn. 3.3), rewritten as a homogeneous system of equations, and solving the system for the phase boundary (end-point) compositions. The fractions of total deuterated lipid probe in each phase, $f^o_{DPPCd62}$ and $f^d_{DPPCd62}$, are determined from the spectral subtraction in step one. However, the above equations for the fractions of phase only apply to binary systems because they are derived from the binary lever rule; their substitution into the conservation of matter equations for the ternary system decouples the problem into the projections on the binary axes. But these equations are not the same as for the ternary system, because the ternary lever rule is not conserved under this projection. The lever rule for ternary systems is given in Eqn 4 and is a function of the mole fractions of two components (unlike binary systems); therefore, the fraction of one other component, either DOPC or Cholesterol, in each phase needs to be determined by a similar spectral subtraction procedure to solve for the phase boundaries.

Taking into account the inherent differences between ESR and NMR spectra, the TLF method has no disadvantages over the other methods, since it can be applied to either data with little or no modification. Therefore, the issue with the type of data has more to do with quality than methodology. In an ESR experiment, the spin-probe is added to the lipid system in low concentrations, whereas, in an NMR experiment, the deuterated lipid probe is a component of the system. In applying the TLF method to NMR spectra, this probe property would allow replacing the $K_p(u)$ function with $K_p(u) = \frac{\xi^o_{DPPCd62}(u)}{\xi^d_{DPPCd62}(v(u))}$, which can be calculated from the ruled surface parameterization of the TLF, is dependent on the coexistence curve, and satisfies the boundary conditions for both the open and closed coexistence curve configurations. However, a disadvantage of an NMR experiment would be the great expense in making the many deuterated samples required for the TLF method. In addition, two ideal properties of any spectral data to be fit with the TLF method are to have significantly different lineshapes for different phases and to change appreciably with variable composition within one phase. Because both ESR and NMR lipid probes are sensitive to the ordering of the lipid acyl chains, both types of spectra typically have much different lineshapes in different phases; however, since an ESR probe is more sensitive to lipid dynamics, the ESR spectra tend to change more noticeably along the coexistence curve with changing composition (1, 8, this study). In the DPPC/Chol binary system, studies employing ^{2}H-NMR (35, 36) observed only small differences in the L_d and L_o spectra vs. temperature and composition, thus rendering a spectral subtraction analysis for phase boundaries very difficult. One proposed reason for the spectral similarity is exchange averaging over small liquid phase domains within the NMR timescale (35); however, in the ternary systems with DOPC, the $L_o + L_d$ coexistence region exhibits large phase

domains (10). Another reason is the reduced resolution arising from the superposition of ^{2}H NMR spectra from all positions along the acyl chains (36).

C. Tie-Lines and Theoretical Interpretations

The general consensus is that the phase behavior of ternary lipid systems containing a gel-forming saturated phospholipid, an L_d-forming unsaturated phospholipid, and cholesterol would be similar. In fact, the phase diagrams of the DPPC/DOPC/Chol, DSPC/DOPC/Chol, and SPM/DOPC/Chol lipid systems do contain similar two-phase coexistence regions along with a three-phase triangle. However, the steeper slopes of the tie-lines for the $L_o + L_d$ coexistence region of the SPM/DOPC/Chol mixture obtained from the TTL method (2) and the TLF method (this work) contrast with the shallower slopes of the tie-lines for the $L_o + L_d$ coexistence region of the DPPC/DOPC/Chol mixture obtained using the Veatch et al method (18). The TLF of the DPPC system (18) was assumed to be parallel because the slope of the determined tie-line was roughly parallel to the end tie-line of the neighboring three-phase triangle. The TLF of the SPM system is not parallel (Figure 3.6A, B), but has the smallest slope at the end tie-line with increasing slopes connecting the L_o phases with the highest amounts of cholesterol to the L_d phases with the lowest amounts of cholesterol and then decreasing slopes approaching the critical point.

The slopes of tie-lines are significant because they show the difference in lipid mole fractions between each phase, which reflects the favorable or unfavorable interactions between the lipids. For example, a 60° slope implies that the SPM (or DPPC) mole fraction is constant in the two phases with the larger differences in the mole fractions of DOPC and cholesterol, suggesting that the energetic repulsion between DOPC and cholesterol drives the L_o and L_d phase separation. This is reasonable because of the predicted poor packing between the rigid ring structure of

cholesterol and an unsaturated acyl chain, especially with the double bond of DOPC in the middle of the chain. Shallower tie-line slopes show less of a difference in the cholesterol mole fraction and a greater difference in the SPM (or DPPC) and DOPC mole fraction between the L_d and L_o phases, suggesting the energetic interaction driving phase separation is the attraction of well-aligned saturated chains for each other.

Elliot et al (20) proposed a statistical model using mean-field theory that takes into account lipid packing with a tendency to align the chains with the bilayer normal. This tendency is a result of the long-range attraction between lipids due to the hydrophobic effect. In this model, cholesterol interacts equally well with the bonds of unsaturated or saturated acyl chains, but cholesterol is more repulsed by unsaturated chains overall because of poor packing. Their model predicted tie-lines with approximately 60° slopes for the $L_o + L_d$ coexistence region of a saturated/unsaturated/cholesterol lipid system (37).

The Elliot et al model contrasts with McConnell's condensed complex model (19). In McConnell's regular solution theory, saturated lipids and cholesterol chemically react forming complexes which can interact as a unit with the unsaturated lipid and unbound saturated lipid and cholesterol. This model emphasizes a stronger attraction of cholesterol to saturated chains instead of unsaturated chains over a background tendency to mix uniformly as required by the thermodynamic entropy of mixing. A calculated DPPC/DOPC/Chol phase diagram with the condensed complex model shows tie-lines with slopes of approximately 30° for the $L_o + L_d$ region (19). Indeed, the phase diagrams of both the DSPC/DOPC/Chol and DPPC/DOPC/Chol systems show the end tie-line of the $L_o + L_d$ region with a shallow slope between 10° and 30°, with the determined tie-line in the DPPC system also having this slope (18).

The TLF of the SPM/DOPC/Chol system also has a shallow slope for the end

tie-line but steeper slopes with increasing concentrations of DOPC. This result suggests that at higher saturated lipid amounts near the three-phase triangle the L_o and L_d phase separation is driven by the attraction of chain alignment, whereas with increasing amounts of unsaturated lipid the tie-lines bend to steeper slopes, reflecting the greater contribution of the packing repulsion between unsaturated chains and cholesterol to the free energy. More experimentally determined tie-line fields of ternary lipids systems will be needed to resolve whether there is any discrepancy of the steeper slopes in the SPM system than the saturated glycerophospholipid system.

REFERENCES

1. Chiang, Y. W.; Zhao, J.; Wu, J.; Shimoyama, Y.; Freed, J. H.; Feigenson, G. W. *Biochim. Biophys. Acta* **2005,** 1668, 99.
2 . Swamy, M. J.; Ciani, L.; Ge, M.; Smith, A. K.; Holowka, D.; Baird, B.; Freed, J. H. *Biophys. J.* **2006**, 90, 4452.
3 . Smith, A. K.; Buboltz, J. T.; Spink, C. H.; Feigenson, G. W. *Biophys J.* **2003**, 84, 372a.
4. Feigenson, G. W. *Annu. Rev. Biophys. Biomol. Struct.* **2007**, 36, 63.
5. London, E. *Biochim. Biophys. Acta* **2005**, 1746, 203.
6. Edidin, M. *Annu. Rev. Biophys. Biomol. Struct.* **2003**, 32, 257.
7. Simons, K.; Winchil, L. C. V. *Annu. Rev. Biophys. Biomol. Struct.* **2004**, 33, 269.
8. Chiang, Y. W.; Costa-Filho, A. J.; Freed, J. H. *J. Phys. Chem B* **2007**, 111, 11260.
9. Zhao, J.; Wu, J.; Heberle, F. A.; Mills, T. T.; Klawitter, P.; Huang, G.; Costanza, G.; Feigenson, G.W. *Biochim. Biophys. Acta* **2007**, 1768, 2764.
10. Veatch, S. L.; Polozov, I. V.; Gawrisch, K.; Keller, S. L. *Biophys. J.* **2004**, 86, 2910.
11. Kahya, N.; Scherfeld, D.; Bacia, K.; Schwille, P. *J Struct. Biol.* **2004**, 147, 77.
12. Veatch, S. L.; Keller, S. L. *Phys. Rev. Lett.* **2005**, 94, 148101.
13. Feigenson, G. W.; Buboltz, J. T. *Biophys. J.* **2001**, 80, 2775.
14. de Almeida, R. F. M.; Fedorov, A.; Prieto, M. *Biophys. J.* **2003**, 85, 2406.
15. Heberle, F. A.; Buboltz, J. T.; Stringer, D.; Feigenson, G. W. *Biochim. Biophys. Acta* **2005**, 1746, 186.
16. Buboltz, J. T. *Physical Review E.* **2007**, 76, 021903.
17. Veatch, S. L.; Gawrisch, K.; Keller, S. L. *Biophys. J.* **2006**, 90, 4428.

18. Veatch, S. L.; Soubias, O.; Keller, S. L.; Gawrisch, K. *P. N. A. S.* **2007**, 104, 17650.

19. McConnell, H. M. *Biophys J.* **2005**, 88, L23.

20. Elliot, R.; Katsov, K.; Schick, M. *J. Chem. Phys.* **2005**, 122, 044904.

21. Tedrow, P. M.; Lee, D. M. *Physical Review* **1969**, 181, 399.

22. Bahari, Z.; Rivet, J.; Legendre, B.; Dugue, J. *Journal of Alloys and Compounds* **1999**, 289, 99.

23. Kundrat, D. M.; Elliott, J. F. *Metallurgical Transactions A* **1986**, 17A, 1461.

24. Orr, Jr., F. M.; Dindoruk, B.; Johns, R. T. *Ind. Eng. Chem. Eng.* **1995**, 34, 2661.

25. Buboltz, J. T.; Feigenson, G. W. *Biochim. Biophys. Acta* **1999**, 1417, 232.

26. Huang, J.; Buboltz, J. T.; Feigenson, G. W. *Biochim. Biophys. Acta* **1999**, 1417, 89.

27. Palatnik, L. S.; Landau, A. I. *Phase Equilibria in Multicomponent Systems*; Holt, Rinehart and Winston, Inc.: New York, 1964.

28. Gordon, P. *Principles of Phase Diagrams in Materials Systems*; McGraw-Hill Book Company: New York, 1968.

29. Gray, A.; Abbena, E.; Salamon, S. "Ruled Surfaces." Ch. 14 in *Modern Differential Geometry of Curves and Surfaces with Mathematica, 3rd ed.*; CRC Press: Boca Raton, FL, p. 432, 2006.

30. Wang, C. C. L.; Tang, K. *Journal of Computing and Information Science and Engineering* **2005**, 5, 291.

31. Schneider, D. J.; Freed, J. H. *Biological Magnetic Resonance* **1989**, 8, 1.

32. Press, W. H.; Flannery, B. P.; Teukolsky, S. A.; Vetterling, W. T. *Numerical Recipes in C: The Art of Scientific Computing, 2nd ed.*; Cambridge University Press: London, 1992.

33. Bachman, I. *J. Phys. Chem.* **1940**, 44, 446.

34. Hsueh, Y. W.; Gilbert, K.; Trandum, C.; Zuckermann, M.; Thewalt, J. *Biophys. J.* **2005**, 88, 1799.

35. Vist, M. R.; Davis, J. H. *Biochemistry* **1990**, 29, 451.

36. Huang, T. H.; Lee, C. W. B.; Das Gupta, S. K.; Blume, A.; Griffin, R. G. *Biochemistry* **1993**, 32, 13277.

37. Elliot, R.; Szleifer, I.; Schick, M. *Physical Review Letters.* **2006**, 96, 098101.

Chapter Four: Overview of This Work to the Field of Membrane Biophysics

I. Phase Behavior and Model Systems

Chapter One was an introduction to phase behavior in general, phase behavior of model lipid systems in particular, and the two-phase model for the physical structure of biological membranes. Although the introduction was primarily background for the work in the subsequent chapters, the important points of the discussion were related to the role of chemical and mechanical phase behavior in the interpretation of experimental results from work on both biological and model membranes in the context of the two-phase model and the applicability of work on model membranes in clarifying and explaining the two-phase model. Although discrepancies exist from experiments on biological and model membranes, and the interpretation of these results on a multidisciplinary problem (i.e. lipid rafts) are through the lenses of different researchers from many fields, the chemical and mechanical phase behavior of lipid bilayers provides the theoretical foundation for understanding lipid rafts. Furthermore, a complete and thorough understanding of this complex phase behavior must (can only) be done initially on simple model systems, so that in the future more complex model systems that more closely approximate biological membranes can be studied accurately and the lipid raft model can be expanded constructively.

The importance of chemical and mechanical phase behavior of model lipid systems, both equilibrium and non-equilibrium, is to provide a solid theoretical foundation for the two-phase model so that it can be applied with confidence to complex biological membranes. Under the important assumption that biological membranes contain two, coexisting thermodynamic phases, the outstanding questions of the two-phase model can be formulated within the chemical and mechanical phase behavior of lipid bilayers. For example, chemical equilibrium relates to the phases'

compositions, and chemical non-equilibrium (i.e. phase separation) relates to the phases' stability, either locally as fluctuating non-ideal (non-random) aggregations or globally as coexisting phases. In addition, mechanical equilibrium, particularly locally, of lipid domains relates to the size/shape of the phases, and mechanical non-equilibrium relates to the phases changing size/shape or coalescing from nanoscopic to microscopic in size.

The chemical and mechanical phase behavior of even simple model systems is non-trivial; therefore, better analysis is needed to expand to more complicated model systems. The development of methodology to determine detailed chemical equilibrium, such as tie-line fields for two-phase coexistence regions, is just the first step. Model systems involving proteins and lipids will require both experimental and theoretical advances to dissect complex multi-dimensional phase diagrams. Furthermore, much work remains for the development of methodologies and theories for the exploring and explaining the mechanical phase behavior of model systems. In conclusion, model systems are just that, models, but without a comprehensive and thorough understanding of the complex phase behavior of simple lipid mixtures, both chemically and mechanically, which underpin the tenets of the two-phase model, then attempts to understand the structure and function of biological membranes directly will be fraught with complications and misdirection.

II. The Importance of Both Chemical and Mechanical Phase Behavior

Chapter Two described the construction of the compositional phase diagram for the SPM/DOPC/Chol lipid mixture at 23°C and the observations of the mechanical phase behavior of GUVs composed of this mixture. This particular lipid mixture, dubbed the "canonical raft mixture" by the field because of previous work showing two immiscible macroscopic liquid phases (i.e. L_o and L_d phase), was used to model the plasma membrane because it contained SPM, unsatured lipid, and cholesterol. The

compositional phase diagram, particularly the $L_o + L_d$ two-phase coexistence region, was determined to address the proposed phase compositions in the two-phase model for biological membranes. In addition, observations of the mechanical phase behavior showed the complex dynamics of phase-separated GUVs, the mechanical membrane model that most closely approximates real cells, and how these dynamics varied with membrane composition.

A basic proposition of the two-phase model is that the composition of one phase (called the raft phase) contains a high mole fraction of cholesterol and sphingolipids, while the other phase contains a high mole fraction of unsaturated lipids. As determined in this work, the $L_o + L_d$ coexistence region of SPM/DOPC/Chol, which has a L_o phase boundary with phase compositions rich in cholesterol and SPM and a L_d phase boundary with phase compositions rich in DOPC and low in cholesterol, validates the basic phase compositions of the two-phase model. In addition, according to the phase rule, a biological membrane with many lipids could possibly contain many coexisting phases; therefore, an argument in the field against model membranes is that lipid mixtures of only three components are poor models for biological membranes. However, results against this argument are 1) most of the various glycerophospholipid species in the plasma membrane are unsatured phosphatidylcholines (like DOPC), which are completely miscible with each other over all compositions, essentially forming a single phase, and 2) GUVs composed of lipids and proteins extracted from biological membranes show two phases both at room temperature and physiological temperature (1, 2). The importance of the phase diagram is to show that model lipid mixtures can exhibit two fluid phases with compositions similar to those found in biological membranes.

Along with the chemical phase behavior, another contribution of this work is the mechanical phase behavior relating to the material/areal fraction of two coexisting

phases and its relation to the two-phase model of biological membranes. The original vision of the two-phase model was that the raft phase (i.e. L_o phase) was disconnected from the other phase. However, although the exact threshold was indeterminate in this work, percolation in general for coexisting L_o and L_d phase was dependent on composition, where at higher cholesterol concentrations the membrane is almost entirely the L_o phase. Therefore, the raft phase of biological membranes is probably the majority or connected phase; an observation that has been reported (3).

Finally, another important contribution within Chapter Two is the importance of the mechanical phase behavior of phase-separated bilayers, especially concerning curvature, surface tension, and line tension, and the possible relationship to cellular processes. The observation of light-induced phase domain size/shape transitions can possibly explain another proposition of the two-phase model, which is that in the resting state of the plasma membrane, the raft phase is nanoscopic in size (10-200 nm), but, when "activated", the phase domains can coalescence into larger, more stable domains that can perform some cellular function (4, 5). The line tension is know to control the size and shape of phase domains, with low line tension favoring many nanoscopic domains or highly amorphous domains and high line tension favoring large circular domains. The observations of light-induced mechanical phase transitions demonstrate that specific lipids (in this work oxidized lipids) or particular proteins in biological membranes could possible increase the line tension of nanoscopic raft phase domains to promote their coalescence into larger functional domains. This process is a physical transformation that does not require specific lipid-lipid or protein-lipid interactions. Future work into the mechanical phase behavior of phase-separated bilayers within model systems will undoubtedly prove fundamental to unraveling these complicated phenomena and their relation to the function of the raft phase in biological membranes.

III. The Need for Better Analysis of Phase Behavior in Model Systems

Chapter Three describes the development of a data-fitting method to determine the tie-line fields of two-phase coexistence regions and its application to the $L_o + L_d$ coexistence region in SPM/DOPC/Chol. The benefit of tie-line fields is to locate the exact compositions of the two coexisting phases. As mentioned above, the $L_o + L_d$ coexistence region of the SPM/DOPC/Chol phase diagram validated the proposition of the two-phase model that the raft phase contains high amounts of cholesterol and SPM, but, without the tie-lines, the exact mole fractions of the coexisting phases, and therefore the possible compositions of the phases in biological membranes, were unavailable. However, the determined tie-line field of this region suggests that the major difference between L_o and L_d phases is the mole fraction of cholesterol and DOPC, while the mole fraction of SPM is only slightly greater in the L_o phase than the L_d phase. Therefore, the nature of the L_o phase and, by extension, the phases of the two-phase model has more to do with the segregation of cholesterol from unsaturated lipids, than the association of cholesterol to SPM or saturated acyl chains. Moreover, the chemical interactions underlying the formation of coexisting phases can be determined from the tie-line fields of coexistence regions within model systems.

Regardless of the exact tie-line field for the $L_o + L_d$ coexistence region of SPM/DOPC/Chol, the most important contribution of Chapter Three is the development of a methodology to address a specific problem concerning chemical phase behavior. Although the tie-line field is a detail of coexistence regions within phase diagrams, they are integral to understanding chemical equilibrium and determining the exact compositions of coexisting phases. Furthermore, the ruled surface parameterization of the tie-line field method will possibly allow the extension of determining the chemical equilibrium of coexistence regions of higher dimension. This extension will be required to understand the chemical phase behavior of better

models, such as quaternary mixture of lipids and proteins or asymmetric bilayers with leaflets of different composition. Moreover, perhaps the contribution of this work in its entirety is that the improvement of the two-phase model for the structure of biological membranes depends on the improvement of observing and analyzing complex chemical and mechanical phase behavior in model membranes.

REFERENCES

1. Baumgart, T.; Hammond, A. T.; Sengupta, P.; Hess, S. T.; Holowka, D. A.; Baird, B. A. *Proc. Natl. Acad. Sci.* **2007**, 104, 3165.
2. Lingwood, D.; Ries, J.; Schwille, P.; Simons, K. *Proc. Natl. Acad. Sci.* **2008**, 105, 10005.
3. Swamy, M.; Ciani, L.; Ge, M.; Smith, A.; Holowka, D.; Baird, B.; Freed, J. *Biophys. J.* **2006**, 90, 4452.
4. Lingwood, D.; Simons, K. *Science*. **2010**, 327, 46.
5. Pike, L. *J. Lipid Res.* **2009**, S323.

APPENDIX A

Definitions of Symbols and Abbreviations

Subscripts: S = Sphingomyelin, D = DOPC, C = Cholesterol

Superscripts: o = L_o phase, d = L_d phase

i = S, D, or C and j = o or d

$\xi_i = \frac{N_i}{N}$ = total mole fraction of component i (cf. Eqn 1)

$\boldsymbol{\xi}$ = vector of mole fractions ξ_i for the whole sample (cf. Eqn 1)

ψ = coordinate transform of $\boldsymbol{\xi}$ (cf. Eqn 2)

$\xi_i^j = \frac{N_i^j}{N^j}$ = mole fraction of component i in the jth phase (cf. Eqn 3)

$\boldsymbol{\xi}^j$ = vector of mole fractions ξ_i^j for the jth phase (cf. Eqn 3)

ψ^j = coordinate transform of $\boldsymbol{\xi}^j$ (cf. Eqn 4)

N_i^j = number of moles of component i in the jth phase

$N_i = \sum_j N_i^j$ = total number of moles of component i

$N^j = \sum_i N_i^j$ = total number of moles of the jth phase

$N = \sum_j \sum_i N_i^j$ = total number of moles

$\phi^j = \frac{N^j}{N}$ = mole fraction of the jth phase (cf. Eqns 3, 4)

t = chord-length parameter for the entire coexistence curve (cf. Figure 4B)

u = chord-length parameter for L_o phase boundary; specifies tie-line (cf. Eqn 6)

$v(u)$ = chord-length parameter for L_d phase boundary (cf. Eqn 6)

$\mathbf{S}$ = spectrum of the whole sample (cf. Eqn 8)

$\mathbf{S}^j$ = spectrum of the jth phase (cf. Eqn 8)

$f^j = \frac{N_{probe}^j}{N_j}$ = fraction of total $probe$ in the jth phase (cf. Eqn 8)

$K_p(u)$ = predicted partition coefficient for parameter u (cf. Eqns 14, 15)

$\left\langle \chi_{red}^2 \right\rangle_k$ = reduced (unweighted) Chi-square for the kth trial tie-line (cf. Eqn 16)

$\left(\sigma_{K_p}\right)_k$ = standard deviation of K_p for the kth trial tie-line (cf. Eqn 16)

$(\chi^2)_k$ = weighted Chi-square for the kth trial tie-line (cf. Eqn 16)

TTL = trial tie-line, TLF = tie-line field, HTLF = hypothetical tie-line field,
CPR = critical point region, ETR = end tie-line region

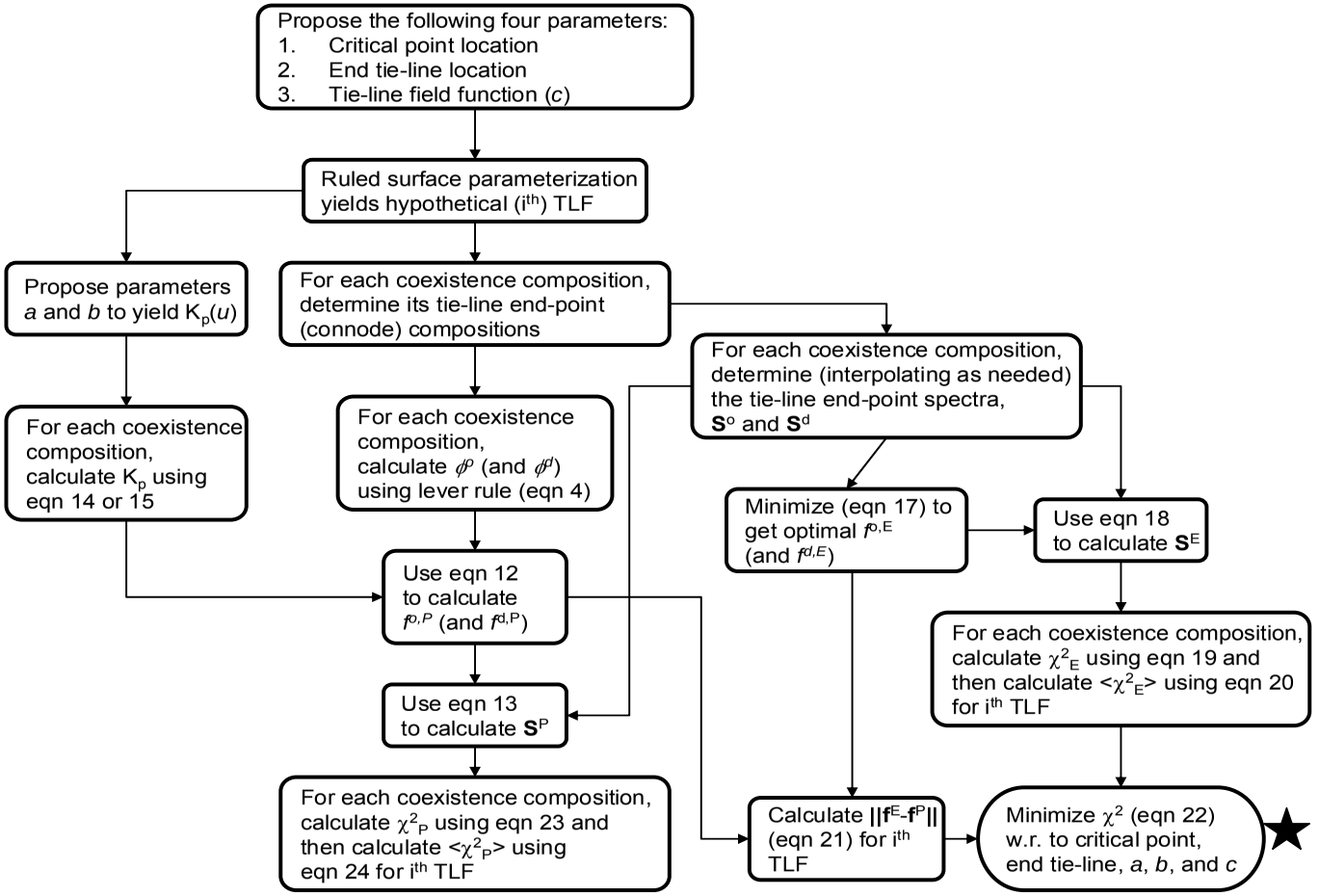

Figure 3.7: The flow chart of the TLF data fitting method showing the order and dependences of important calculations and procedures.

APPENDIX B
Algorithm for Obtaining the Tie-Line Field

The algorithm is outlined below and also illustrated in a flow chart, (cf. Figure 3.7).

1) An arbitrary choice of critical point(s) and/or end tie-line locations is made within their expected range. In addition the TLF function $v(u)$ is selected with an arbitrary choice of parameter c.

2) The ruled surface parameterization yields the ith hypothetical TLF (HTLF).

3) From the HTLF, determine the tie-line for the kth coexistence composition (51 total in the present study); this yields the two tie-line end-point (connode) compositions, from which ϕ^o and $\phi^d = 1 - \phi^o$ are determined from the lever rule (Eqn. 3.4).

4) From the experimental ESR spectra along the coexistence curve determine (interpolating as needed) the ESR spectrum for each of the two tie-line end-point compositions found in step 3 for the kth coexistence composition.

5) Then for the experimental ESR spectrum at the kth coexistence composition ($\mathbf{S}_k$) and the spectra at the two hypothetical tie-line end-points ($\mathbf{S}^d$ and $\mathbf{S}^o$) solve the constrained least squares problem based on the linear superposition that is given by

$$\min_{\mathbf{f}^E} \left\| \left[\mathbf{S}^d_{i,k}(\xi^d_{i,k}) \quad \mathbf{S}^o_{i,k}(\xi^o_{i,k}) \right] \mathbf{f}^E - \mathbf{S}_k(\xi_k) \right\|^2, \qquad \text{(Eqn. 3.17a)}$$

where

$$\mathbf{f}^E = \begin{bmatrix} f^{d,E}_{i,k} \\ f^{o,E}_{i,k} \end{bmatrix}$$

, to determine $f^{o,E}_{i,k}$ (and $f^{d,E}_{i,k} = 1 - f^{o,E}_{i,k}$). The vector $\mathbf{f}^E$ contains the "estimated" fraction of total spin-probe coefficients $f^{d,E}$ and $f^{o,E}$. These estimates are implicitly based on allowing K_p to vary independently for each coexistence composition. This "estimated" K_p can be calculated with

$$(K_p)^E_{i,k} = \frac{f^{o,E}_{i,k}}{f^{d,E}_{i,k}} \frac{\phi^d}{\phi^o}, \qquad \text{(Eqn. 3.17b)}$$

which is a rearrangement of Eqn. 3.12.

6) Then one determines an "estimated" spectrum $\mathbf{S}^E$ from

$$\mathbf{S}_{i,k}^{E} = f_{i,k}^{o,E}\mathbf{S}_{i,k}^{o} + f_{i,k}^{d,E}\mathbf{S}_{i,k}^{d} \qquad \text{(Eqn. 3.18)}$$

for the k^{th} coexistence composition.

7) Now for the k^{th} coexistence composition one determines

$$(\chi_E^2)_{i,k} = \frac{\left\|\mathbf{S}_{i,k}^{E} - \mathbf{S}_k\right\|^2}{\sigma_k^2} \qquad \text{(Eqn. 3.19)}$$

where χ^2_E is the chi-square between the "estimated" spectrum and the experimental spectrum for a coexistence composition. The variance of the noise (σ^2) was taken from the first and last 200 points of the experimental spectrum. Then the average of χ^2_E or $\left\langle \chi_E^2 \right\rangle_i$ is taken over all coexistence compositions for the i^{th} HTLF:

$$\left\langle \chi_E^2 \right\rangle_i = \frac{1}{N}\sum_{k=1}^{N}(\chi_E^2)_{i,k} \qquad \text{(Eqn. 3.20)}$$

8) Now an arbitrary choice is made of the parameters *a* (and *b*) in the functional form for the $K_p(u)$ (Eqn. 3.14 or 3.15) giving the j^{th} K_p parameters. The "predicted" K_p for the k^{th} coexistence composition is the evaluation of the K_p function using the L_o boundary parameter *u* for that coexistence composition. Then Eqn. 3.13 was used to generate another set of spectra, $\mathbf{S}^P$, called the "predicted" spectrum for each coexistence composition using the linear combination of tie-line end-point spectra obtained from the HTLF. This $\mathbf{S}^P$ is thus based on a "constrained" $K_p(u)$, which is required to be constant along each tie-line. Also, the $f^{o,P}$ and $f^{d,P}$, the "predicted" fraction of total spin-probe coefficients, are readily obtained from Eqn. 3.12.

9) Now for the i^{th} HTLF and j^{th} K_p parameters obtain the norm of the squares of the differences between the $f^{o,E}$ and $f^{o,P}$ and the $f^{d,E}$ and $f^{d,P}$ given by

$$\left\|\mathbf{f}^E - \mathbf{f}^P\right\|_{i,j} = \sqrt{\sum_{k=1}^{N}(f_{i,k}^{o,E} - f_{i,j,k}^{o,P})^2 + (f_{i,k}^{d,E} - f_{i,j,k}^{d,P})^2} \qquad \text{(Eqn. 3.21)}$$

10) From steps 7 and 9 one then forms the weighted chi-square $(\chi^2)_{i,j}$ given by

$$(\chi^2)_{i,j} = \left\langle \chi_E^2 \right\rangle_i \times \left\| \mathbf{f}^E - \mathbf{f}^P \right\|_{i,j} \qquad \text{(Eqn. 3.22)}$$

for the ith HTLF and jth choice of K_p parameters.

11) Now minimize $(\chi^2)_{i,j}$ with respect to critical point(s) and/or end tie-line locations and the parameters *a*, *b*, and *c* to find the best fit TLF and K_p function consistent with the global set of ESR spectra.

12) In addition, calculate the chi-square

$$(\chi_P^2)_{i,j,k} = \frac{\left\| \mathbf{S}_{i,j,k}^P - \mathbf{S}_k \right\|^2}{\sigma_k^2} \qquad \text{(Eqn. 3.23)}$$

for the kth coexistence composition, and then perform the average over the N (51 in this study) coexistence compositions to obtain $\left\langle \chi_P^2 \right\rangle_{i,j}$ given by

$$\left\langle \chi_P^2 \right\rangle_{i,j} = \frac{1}{N} \sum_{k=1}^{N} (\chi_P^2)_{i,j,k} \qquad \text{(Eqn. 3.24)}$$

for the ith choice of TLF and the jth choice of K_p parameters.

From a comparison of Eqn. 3.16 from the TTL method and Eqn. 3.22 for the TLF method, one sees that χ^2_E plays the role of χ^2_{red}, and $||\mathbf{f}^E - \mathbf{f}^P||$ is related to σ_{K_p}. In fact, a major reason we used Eqn. 3.22 for fitting our data was because Eqn. 3.22, applied to find a single tie-line, yields the same answer as Eqn. 3.16 for the best trial tie-line when analyzing the same data from the SPM/DOPC/Chol system (2). In addition, stability of the fitting was another reason we used $||\mathbf{f}^E - \mathbf{f}^P||$ of Eqn. 3.21 instead of the norm of the difference between "estimated" and "predicted" K_p's. Very small values of $f^{d,E}$ in Eqn. 3.17b, which could occur in the TLF method, but not in the TTL method, would make the expected K_p very large. The more traditional chi-square, given by Eqn. 3.24, was also calculated for the TLF, but did not provide sufficient stability in the fitting, in accord with the experience in Chiang et al. (1). We attribute this to the fact that the ESR spectra, for small composition displacements along either the L_o or L_d coexistence curve, typically change to a small degree, but there is considerable sensitivity to the degree to which K_p remains constant along a

hypothetical tie-line. Since the fitting chi-square (Eqn. 3.22) and the traditional chi-square (Eqn. 3.24) are closely related, we justifiably used the traditional chi-square to statistically analyze the quality of a fit between different tie-line field models. The fitting of the ESR data with the TLF models was implemented with a program written in Matlab 7.0 R14 (The MathWorks Inc., Natick MA). The choice of search algorithm was either the constrained simplex method ("fminsearchcon" written by John D'Errico, woodchips@rochester.rr.com, released 12/16/06 and obtained from Matlab Central) or the interior-reflective Newton with a subspace trust region using preconditioned conjugate gradients (builtin Matlab 7.0 function "lsqnonlin").

APPENDIX C

Modeling "Parallel" and "Common Vertex" Tie-Line Fields

1. Parallel

The parallel TLF parameter was the slope angle, which varies from zero to pi. For the closed boundary configuration, the slope angle was directly used as the fitting parameter. For the open configuration, the boundary parameters for the end tie-line were the fitting parameters, from which the slope angle can be calculated through the two-point form for a line. However, for both coexistence curve configurations, the critical point(s) location(s) for a given slope angle must be determined for the ruled surface parameterization. We solved this problem the following way:

$$\text{find } b^* : \left\| \psi^d(b_1) - \psi^o(b_2) \right\| = 0 \Rightarrow b^* = b_1 = b_2 \qquad \text{(Eqn. A1)}$$

, where $\psi^d(b_1)$ was an L_d boundary composition and $\psi^o(b_2)$ was an L_o boundary composition of a trial tie-line passing through the coexistence region. This intuitive solution essentially says find the points on the coexistence curve where the length of tie-line goes to zero. For a closed convex curve in two-dimensions the solution always has two unique points. Figure 3.8A shows the process for finding the two critical points for the closed $L_o + L_d$ coexistence region in the SPM/DOPC/Cholesterol system.

In summary, within the parallel TLF model, a hypothetical tie-line through an arbitrary coexistence composition was determined from the point-slope equation for a line, where the slope was calculated from the slope angle ([0, pi]], and the point was the coexistence composition. This tie-line intersects the coexistence curve at the L_o and L_d end-points (connodes), and determining these intersection points is a solved problem for a polygonal representation of the coexistence curve (see the "polyxpoly" built-in function for Matlab 7 R14). For the ruled surface parameterization of the parallel TLF, the L_o boundary parameter u and the L_d boundary parameters v were

Figure 3.8: Graphical representation of finding the critical point in the parallel TLF model and the common vertex TLF model for the closed boundary configuration of the $L_o + L_d$ coexistence region. A) The critical points (squares) are where the L_o boundary composition (diamonds) and L_d boundary composition (triangles) are equal, and therefore where the length of the tie-line equals zero. In this case, the parameter b is the boundary parameter for the section of the boundary between $\psi^d(b_1)$ and $\psi^o(b_2)$, and the root of Eqn. A1 was found by the bisection method. B) In the common vertex TLF model the coexistence curve parameter b locates the critical points (squares). The tangent lines to the critical points (dashed lines) are calculated from an interpolating spline fitted to coexistence curve sections surrounding the critical points. The common vertex of the tangent lines (lower left off the figure) and the coexistence composition (dot) form a line (extend solid line) which forms a tie-line thru that coexistence composition. The L_o compositions (diamonds) and the L_d compositions (triangles) are determined by the intersections of the line thru the coexistence compositions and the common vertex with the coexistence curve.

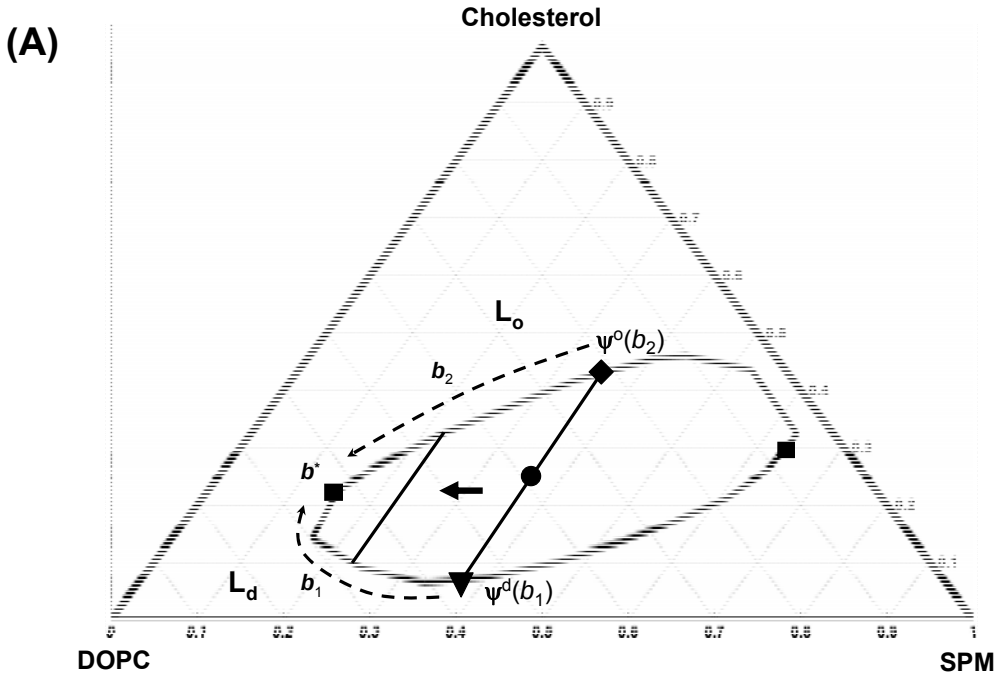
(A)
Cholesterol
L_o
$\psi^o(b_2)$
b_2
b^*
L_d
b_1
$\psi^d(b_1)$
DOPC
SPM

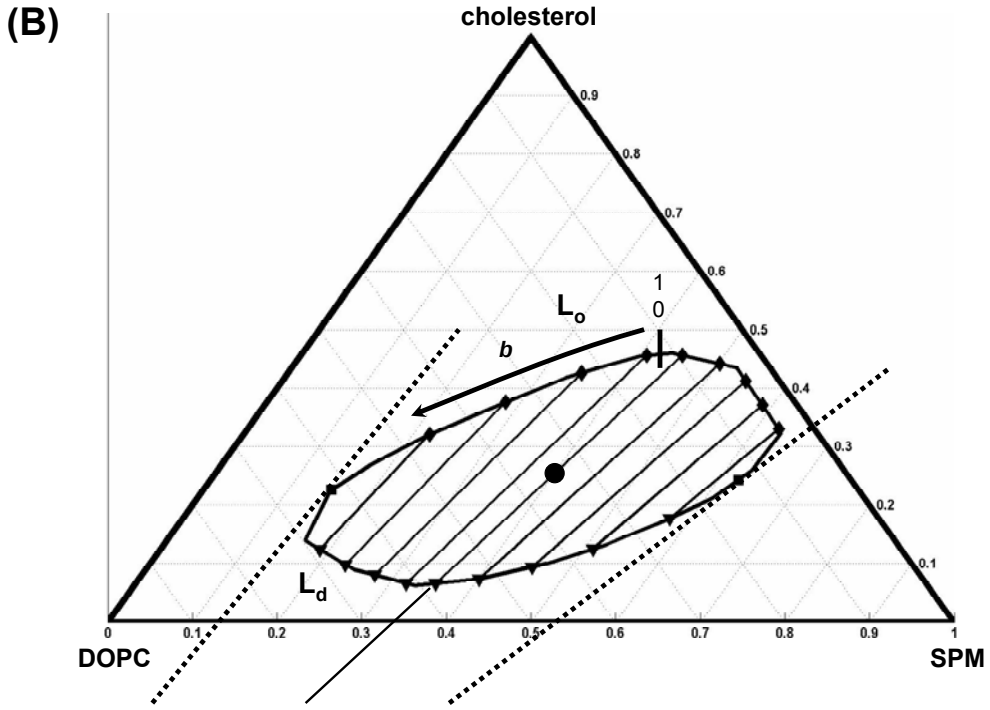
(B)
cholesterol
L_o
1
0
b
L_d
DOPC
SPM

calculated by reverse linear interpolation of the tie-line end-point compositions. Therefore, the tie-line field function was numerically determined by performing the reverse interpolation for each coexistence composition.

2. Common Vertex

The "common vertex" refers to the intersection point of two lines that, once determined, specifies the TLF. For the closed boundary configuration, the common vertex was the intersection of the tangent lines to the two critical points, and, for the open configuration, the common vertex was the intersection of the tangent line to the critical point and the end tie-line. In this model, the easiest way of representing a tie-line was in the two-point form for a line. One point was the coexistence composition, and the other point was the common vertex. The fitting parameters for both the open and closed boundary configurations were the boundary parameters for the location of the critical point(s) and/or end points of the end tie-line. The tangent line to a critical point was determined by first locally fitting, in a least-squares sense, a quadratic interpolating spline to an appropriate section of the coexistence curve. If the critical point was one of the experimental boundary compositions, then the splined section was the critical point and the two flanking experimental boundary compositions (three points total). If the critical point was between two neighboring experimental boundary compositions, then the splined section consisted of four points, the two experimental boundary compositions flanking either side of the critical point. The splined sections we used were to ensure a more accurate representation of the coexistence curve. With the resulting spline representation, the slope of the tangent line was calculated by taking the derivative of the spline and evaluating it at the critical point location. Essentially, the tangent line was determined in point-slope form, where the slope was calculated from the interpolating spline and the point was the critical point. The geometrical justification for using tangent lines to critical points is that as the end

points of a chord of any convex curve (e.g. circle, ellipse, hyperbola, etc) approach each other along the curve, the slope of the line between them approaches the slope of the tangent line at the point where the end points converge. In the common vertex TLF method, the chord is the tie-line, the coexistence curve is the curve, the end points of the chord are the connodes, and the converged point is the critical point. Of course, the assumption here is that the tie-line slopes varying continuously and monotonically from one critical point/end tie-line to another critical point/end tie-line. This was not an erroneous assumption because there was, to our knowledge, no thermodynamic restriction disallowing such a situation and there are numerous experimental phase diagrams over many different systems which showed tie-line fields that seem to conform to this configuration (33). Figure 3.8B shows the common vertex TLF model for the $L_o + L_d$ coexistence region in the SPM/DOPC/Cholesterol system.

In summary, within the common vertex TLF model, a hypothetical tie-line through an arbitrary coexistence composition was the line through the coexistence composition and the common vertex of the critical point(s) and/or end tie-line. In the same way for the parallel TLF method, this tie-line intersects the coexistence curve at the L_o and L_d end-points (connodes). Also, in the same way for the parallel TLF, the tie-line field function for the ruled surface parameterization of the common vertex TLF was determined numerically.

APPENDIX D

Results of Comparison between the Parallel, Common Vertex, and Ruled Surface Tie-Line Field Models

1. All Three TLF Models Gave Consistent and Expected Results for the Hypothetical Boundary Configurations Studied

As explained in the Chapter, the closed boundary configuration was not predicted to exist for the $L_o + L_d$ coexistence region in the SPM/DOPC/Cholesterol lipid system. However, for completeness, we compared results of fitting all three TLF models to the ESR data for hypothetical closed and open boundary configurations designed to test the consistency and expectation of the results. The closed configuration consisted of the expected CPR (Figure 3.5) for one critical point location and the compositions between coexistence curve points 15 and 19 (Figure 3.5) as the other critical point region. The open boundary configuration consisted of the expected CPR for the critical point location and all compositions between points 15 and 19 as the end tie-line region, thus any two points within this region were possible end points of the end tie-line. We called this end tie-line region the expanded ETR to avoid confusion will the expected ETR (Figure 3.5) mention in the main body of the manuscript. The consistency we expected was that the TLF models would give nearly the same tie-line field for both boundary configurations, and that the critical point within points 15 and 19 for the closed configuration would be located between the end points of the end tie-line for the open configuration.

The parallel tie-line fields (data not shown) for the both the open and closed configurations were almost identical with the tie-line slopes (≈ 50 degrees) different by < 0.3 degrees. Also, the common vertex tie-line fields (data not shown) for the both the open and closed configurations were almost identical. For the closed configuration, the tie-line slopes increased from 48.6 degrees at one critical point (u =

0) to 56.9 degrees at the other critical point (u = 1); for the open configuration, the tie-line slopes increased from 48.5 degrees at the critical point (u = 0) to 58.2 degrees at the end tie-line (u = 1). In addition, the ruled surface tie-line fields (data not shown) were visually similar, with the same critical location for the expected CPR (closed = 0.351, open = 0.356), which was within error (Table 3.2), and nearly the same tie-line field function parameter c (closed = 3.314, open = 3.728), which again was within error. Furthermore, the tie-line field functions ($v(u)$) calculated numerically for the parallel and common vertex TLF models were similar between the open and closed configurations (data not shown). All three TLF models gave consistent results between the closed and open boundary configurations, and between each other for a particular boundary configuration.

The fitting chi-squares (χ^2, Eqn. 3.22) and the traditional chi-squares (χ^2_P, Eqn. 3.24) of the three TLF models for both the closed and open boundary configurations, along with the statistical analysis of these results, are shown in Table 3.2. The statistical analysis is the calculation the Q-value, which measures how well the TLF model fit the ESR data taking into account the model's number of degrees of freedom (32). The Q-value is the probability of a chi-square larger than a given chi-square using the chi-square probability distribution with a certain number of degrees of freedom. Therefore, the higher the Q-value the better the TLF model describes the ESR data. The number of degrees of freedom (δ) is the number of data points (N = 51) minus the number of model parameters. To get a more statistically meaningful Q-value inline with a proper analysis of the chi-square statistic, we used the traditional chi-square instead of the fitting chi-square in the calculation.

For both boundary configurations, the ruled surface TLF model has the lowest fitting chi-square, the common vertex model had the highest Q-value, and the parallel

Table 3.2: Chi-squares and statistical analysis of the best-fit results for the parallel, common vertex, and ruled surface TLF models applied to the hypothetical closed and open boundary configuration with the expanded ETR of the $L_o + L_d$ coexistence region within the SPM/DOPC/Cholesterol lipid system. The degrees of freedom (δ) is the number of coexistence compositions, 51, minus the number of fit parameters for the TLF model (2 for parallel/closed, 4 for parallel/open, 3 for common vertex/closed, 5 for common vertex/open, 4 for ruled surface/closed, and 6 for ruled surface/open). The Q-value for χ^2_P and δ is calculated using the incomplete gamma function (32); in Matlab 7.0 (The MathWorks Inc., Natick MA), Q = 1 – gammainc(χ^2_P/2, δ/2), where "gammainc" is Matlab's built-in incomplete gamma function.

	closed boundary configuration				open boundary configuration (expanded ETR)			
parallel	χ^2	χ^2_P	δ	Q	χ^2	χ^2_P	δ	Q
	35.60	53.21	49	0.315	35.48	53.19	47	0.248
common vertex	χ^2	χ^2_P	δ	Q	χ^2	χ^2_P	δ	Q
	35.68	51.75	48	0.330	35.21	51.51	46	0.267
ruled surface	χ^2	χ^2_P	δ	Q	χ^2	χ^2_P	δ	Q
	34.39	51.77	47	0.293	34.14	51.37	45	0.238

model had the highest traditional chi-square and the lowest Q-value. Within either boundary configuration the difference in Q-values between the three TLF models was small suggesting that any of the three models could fit the ESR data almost equally well. In addition, according to the Q-values, all three TLF models fit the data better for the closed configuration than for the open configuration. This is expected because since the tie-line slopes are so similar between the two boundary configurations the TLF models could not significantly decrease the chi-square enough to justify the increase in the number of fit parameters (decrease in degrees of freedom) for the open configuration than the closed configuration. Also, the expanded ETR does not provide enough of a constraint on the tie-line slopes to discern a difference between the TLF models.

2. The Ruled Surface TLF Model Was A Statistically Better Fit for the Expected CPR and ETR than the Parallel or Common Vertex TLF Models

We now compare the results of fitting all three TLF models to the ESR data for the open boundary configuration with the expected CPR and ETR (Figure 3.5). The best-fit parallel TLF (Figure 3.9A) has a slope angle of 33 degrees. The best-fit K_p function is plotted in Figure 3.9B and the numerically calculated tie-line field function is plotted in Figure 3.9C. Since parallel tie-line fields for the open configuration are determined by the slope of the end tie-line, the number of possible tie-line fields is limited because of the smaller ETR. The common vertex TLF model provided an interesting example of the importance of employing a grid search on the critical point and end tie-line boundary parameters, and the difference between the fitting and traditional chi-squares. Figure 3.10A shows two common vertex tie-line fields, one where the common vertex is located in the upper right ("high common vertex"), and one where the common vertex is located in the lower left ("low common vertex"). The slope profiles for these two fields are plotted in Figure 3.10B, their K_p functions

Figure 3.9: The parallel TLF that best-fit the ESR data for the open boundary configuration with the expected CPR and ETR of the $L_o + L_d$ coexistence region within the SPM/DOPC/Cholesterol lipid system. A) A plot showing a few tie-lines from the parallel TLF (slope angle = 33°) , the critical point (square), end-points of the end tie-line (triangles), L_o phase compositions (diamonds), and L_d phase compositions (dots). B) The K_p function (Eqn. 3.15) for the TLF with the maximum $K_p = 1.64$ and the K_p at the end tie-line ($u = 1$) = 1.11. C) The tie-line field function ($v(u)$) for the parallel TLF calculated numerically; each point represents the (u,v) pair for a coexistence composition. The dashed lines are suggested extrapolations to the critical point ($u = 0$) and the end tie-line ($u = 1$) satisfying the boundary conditions (i.e. $v(0) = 0$ and $v(1) = 1$). Notice that this shape was not formulated in the ruled surface tie-line field function (Eqn. 3.7), and that at least another parameter would be needed to specify the general shape.

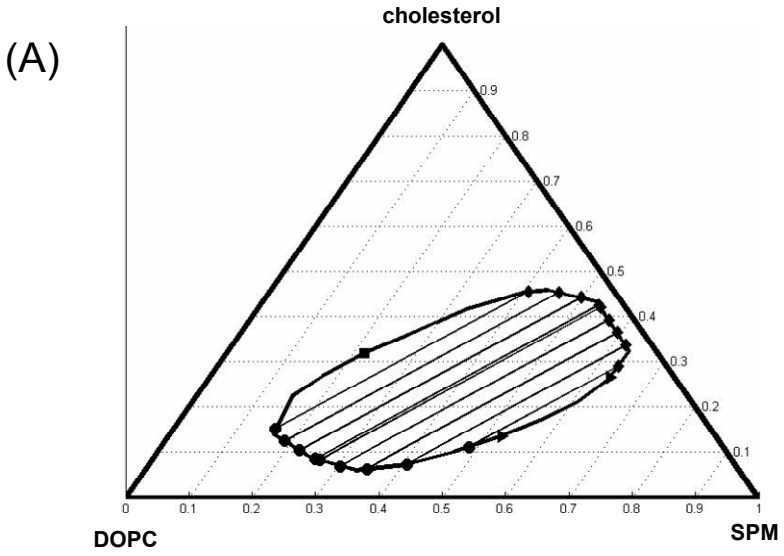
(A)
cholesterol
DOPC
SPM

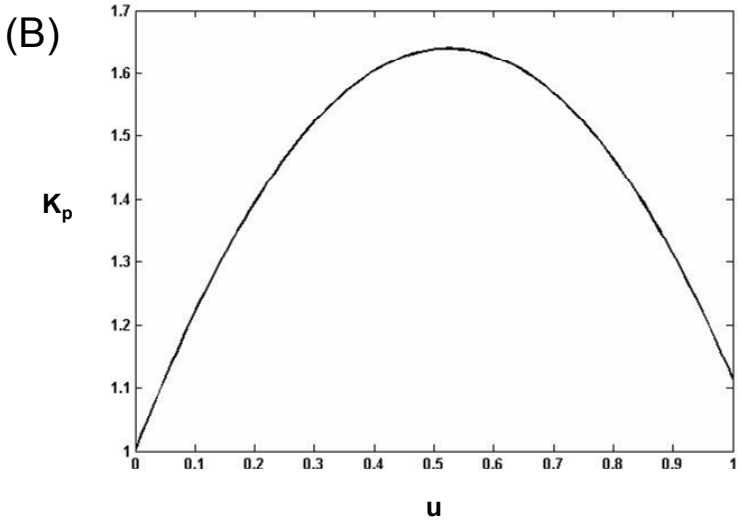
(B)
K_p
u

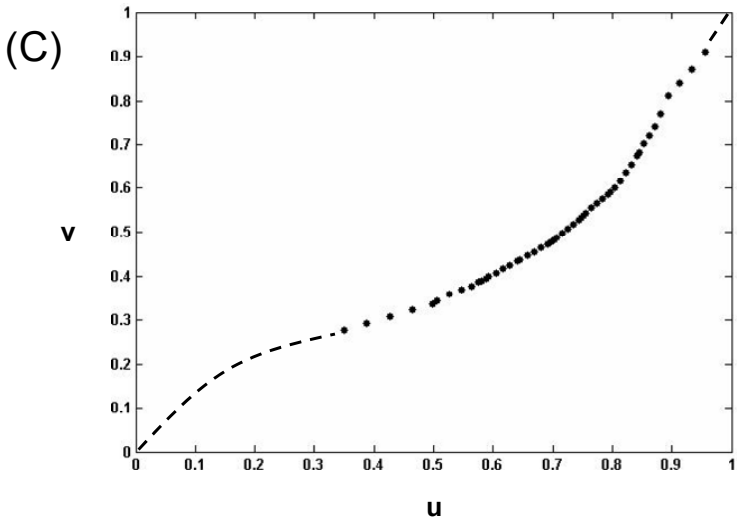
(C)
v
u

Figure 3.10: Interesting example of two different common vertex TLFs which fit the ESR data nearly equally well for the open boundary configuration with the expected CPR and ETR of the $L_o + L_d$ coexistence region within the SPM/DOPC/cholesterol lipid system. The high common vertex TLF and the low common vertex TLF have approximately the same fitting chi-square ($\chi^2 \sim 36$) with different terms (χ^2_E and $||\mathbf{f}^E - \mathbf{f}^P||$ in Eqn. 3.22), but have different traditional chi-squares. A) A plot showing a few tie-lines from the two TLFs. The dashed lines are either the tangent line to the critical points (squares) or extensions of the end tie-lines (triangles) to show the location of the common vertex, all other symbols the same as in Figure 3.9. B) The tie-line slope profiles of the high (solid circles) and low (open squares) common vertex TLFs are different because of the location of the critical point. C) Different K_p functions (Eqn. 3.15) for the high (solid line) and low (dashed line) common vertex TLFs. D) The numerically calculated tie-line field functions of the high (solid circles) and low (open squares) common vertex TLFs are similar although the slope profiles are not. The dashed lines are suggested extrapolations (see Figure 3.9).

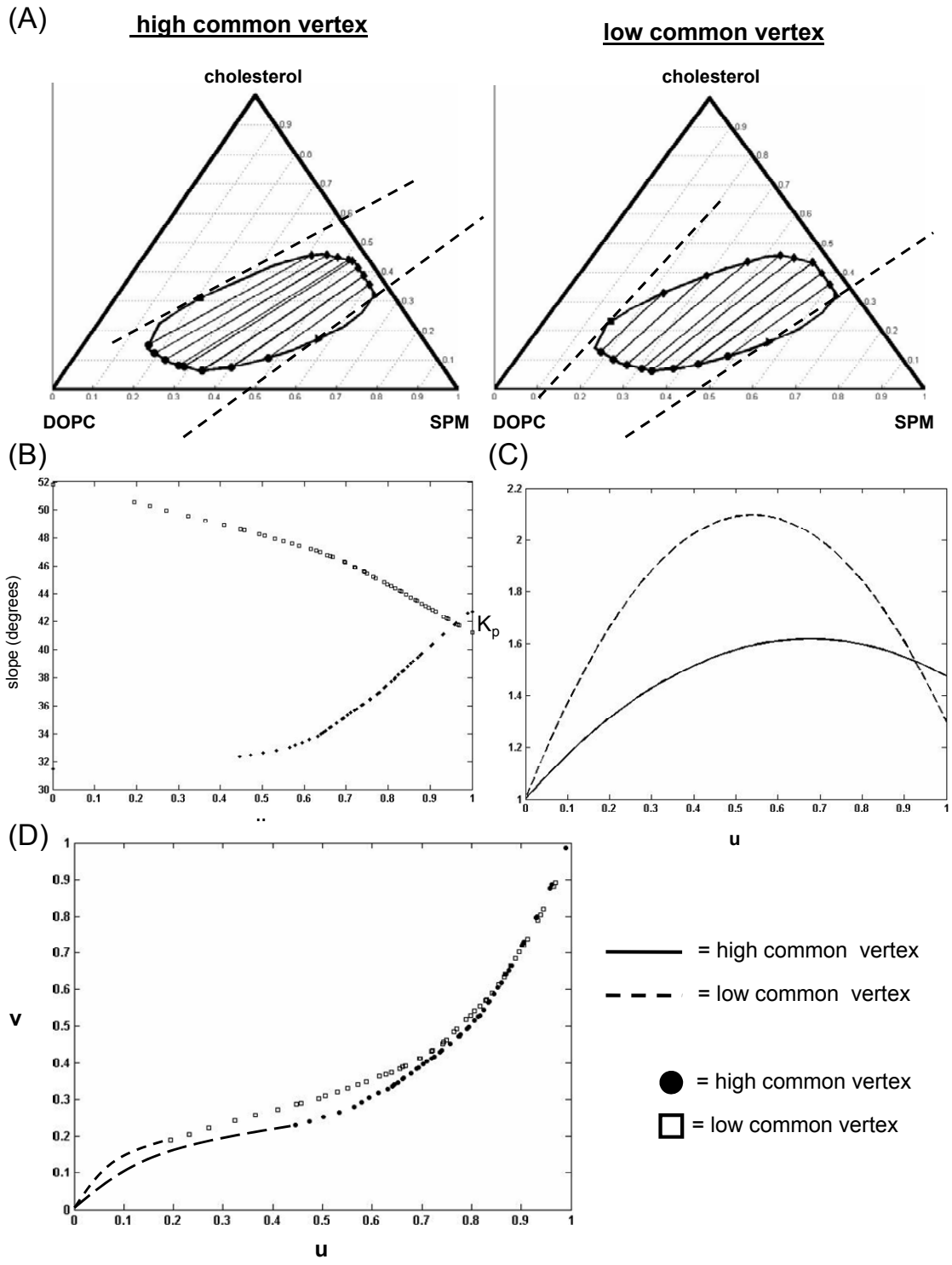
(A)
high common vertex
low common vertex
cholesterol
cholesterol
DOPC
SPM
DOPC
SPM
(B)
(C)
slope (degrees)
K_p
u
(D)
v
u
= high common vertex
= low common vertex
= high common vertex
= low common vertex

are plotted in Figure 3.10C, and their numerically calculated tie-line field functions are plotted in Figure 3.10D. Both TLFs have nearly the same end tie-line parameters (high = [0.72, 0.86], low = [0.71, 0.86]), but differed in the critical point parameter (high = 0.24, low = 0.32). Also, both TLFs have approximately the same fitting chi-square χ^2 (Table 3.3), but differ in the two terms, χ^2_E and $\|\mathbf{f}^E - \mathbf{f}^P\|$ (Eqn. 3.20 and 3.21). The high common vertex TLF has a lower $\|\mathbf{f}^E - \mathbf{f}^P\|$ (0.7334) but a higher χ^2_E (49.09); whereas the low common vertex TLF has a lower χ^2_E (40.10) but a higher $\|\mathbf{f}^E - \mathbf{f}^P\|$ (0.9056). However, these two TLFs exhibit different traditional chi-squares (χ^2_P, Table 3.3). Therefore, the high and low common vertex TLFs represent two different minima with approximately equal fitting chi-squares (Eqn. 3.22) but different traditional chi-squares (Eqn. 3.24). These minima were only found by thoroughly grid searching the critical point and end tie-line boundary parameter space. Moreover, the best-fit TLF model to the ESR data was the ruled surface (Figure 3.6A), which has the lowest fitting and traditional chi-square, and the highest Q-value (Table 3.3). The large difference in Q-values between the TLF models for the same open boundary configuration provides confidence that the ruled surface TLF is the best fit to the data.

Table 3.3: Chi-squares and statistical analysis of the best-fit results for the parallel, common vertex, and ruled surface TLF models applied to the open boundary configuration with the expected CPR and ETR of the $L_o + L_d$ coexistence region within the SPM/DOPC/cholesterol lipid system. See Table 3.2 for the calculation of χ^2, χ^2_P, δ, and Q. The ruled surface TLF model statistically best-fit the ESR data.

	open boundary configuration (constrained transition region)			
parallel	χ^2	χ^2_P	δ	Q
	38.40	62.22	47	0.068
high common vertex	χ^2	χ^2_P	δ	Q
	36.01	60.62	46	0.073
low common vertex	χ^2	χ^2_P	δ	Q
	36.32	55.94	46	0.150
ruled surface	χ^2	χ^2_P	δ	Q
	34.38	52.38	45	0.209